Spin Crossover Behavior of N-Confused C-Scorpionate Complexes of Iron(II) Trifluoromethanesulfonate

Kristin Joy Meise
Marquette University

SPIN CROSSOVER BEHAVIOR OF N-CONFUSED C-SCORPIONATE COMPLEXES OF IRON(II) TRIFLUOROMETHANESULFONATE

By

Kristin J. Meise, B.Sc.

A Thesis submitted to the Faculty of the Graduate School,
Marquette University,
in Partial Fulfillment of the Requirements for
the Degree of Master of Science

Milwaukee, Wisconsin

December 2017

ABSTRACT
SPIN CROSSOVER BEHAVIOR OF N-CONFUSED C-SCORPIONATE COMPLEXES OF IRON(II) TRIFLUOROMETHANESULFONATE

Kristin J. Meise

Marquette University, 2017

An understanding of the molecular properties that influence highly-cooperative SCO behavior is critical in the development of new electronic materials. The purpose of this thesis work is to more fully examine whether hydrogen bonding interactions can be used to assemble iron(II) scorpionate complexes and whether this leads to abruptness in the SCO behavior. In this contribution, new N-confused C-scorpionate ligands are prepared with two 'normal' pz* groups (= 3,5-dimethylpyrazol-1yl) and a 'confused' pyrazolyl with either an N-H, ^{H}L*, or an N-Tosyl (Tosyl = p-toluenesulfonyl), ^{Ts}L*, bound to a central methine. These bulky ligands complement those previously described, ^{H}L and ^{Ts}L, that had less-bulky, unsubstituted, 'normal' pyrazol-1-yls. For these four related N-confused C-scorpionate ligands, the 2:1 and 1:1 ligand:silver complexes are prepared and characterized both structurally and spectroscopically. The complexes' stoichiometric reactivity and catalytic activity for aziridination of styrene are also reported. The solution- and solid-state properties of the iron(II) N-confused C-scorpionate complex, $[Fe(^{H}L^*)_2](OTf)_2$, which unexpectedly displayed multiple solid-state structures and solvates, are also discussed. The synthesis, solid-state characterization, and SCO of both compounds will be described in detail.

ACKNOWLEDGEMENTS

Kristin J. Meise

I would first like to thank my advisor, Dr. James Gardinier, for trusting me with his work. I have gained a tremendous amount of confidence as an independent scientist due to the patience, kindness, and guidance I received throughout the research process. I would also like to thank my committee members, Dr. Adam Fiedler and Dr. Rajendra Rathore, for their valuable insight and feedback. I would like to thank faculty members Dr. Sheng Cai for assisting with the variable-temperature and DOSY NMR experiments, and Dr. Sergey Lindeman for providing the single crystal diffraction analysis data. I would like to thank my current and past group members, Fathiya Jahan and Alex Treleven, for their support and friendship during my time at Marquette.

I would like to acknowledge the chemistry faculty and staff at University of Wisconsin-Eau Claire and Marquette University for providing me with excellent research opportunities and mentors throughout my academic career. I would like to especially thank Dr. Roslyn Theisen and Dr. Abbey Fischer, who both encouraged me to pursue graduate studies.

Lastly, I would like to thank John, who has served as a constant source of encouragement and joy in every challenging and rewarding moment this program has brought me. I am forever grateful for the love you have shown me.

TABLE OF CONTENTS

LIST OF TABLES

LIST OF FIGURES

Chapter 1

INTRODUCTION

Coordination complexes that have transition metal centers in an octahedral ligand environment and that contain between four and seven d- electrons will normally exist at room temperature either with a maximally spin-paired d-electron arrangement (low spin, or LS) or a minimally spin paired electron arrangement (high spin, HS), depending on both the metal and supporting ligands. As an example relevant to this work, iron(II) has six electrons in d-orbitals. When placed in an octahedral ligand environment, the d-orbitals split into two sets- one set aligned with the cartesian coordinates (acting as an E_g representation under the O_h point group) and one set containing the d-orbitals whose lobes are off-axes (and act as the T_{2g} representation of the O_h point group). The t_{2g} set is sigma nonbonding. On the other hand, the e_g set of d-orbitals can combine with ligand orbitals to form a sigma bonding/antibonding pair of molecular orbitals that energetically flank the t_{2g} d-orbitals. The lower energy e_g orbitals are mainly ligand-based, whereas the higher energy, e_g*, orbitals are metal-based. The metal's six d-electrons are found in both the e_g* and t_{2g} orbitals, Figure 1.1. If a ligand has π-orbitals, then these have the

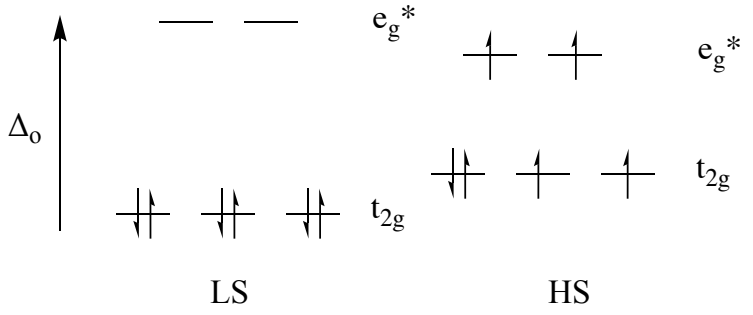

Figure 1.1. For octahedral, Fe(II) systems, the low spin (LS) state contains no unpaired electrons (S=0), while the high spin state (HS) state contains four unpaired electrons (S=2). Δ_o = ligand field strength.

proper symmetry to combine with the metal's t_{2g} set to form a bonding/antibonding pair, where the net effect is to move the t_{2g} set energetically either closer to, or further from the e_g* set. If the energy separation between the e_g* and t_{2g} orbitals, Δ_o, is greater than the coulombic energy penalty to pair electrons (Coulombic pairing energy, Π_c), then the LS arrangement is found. Conversely, a HS state (where electrons are filled per Hund's rule[2]) is observed when the energy separation between e_g* and t_{2g} orbitals is small ($\Delta_o < \Pi_c$). The magnitude of Δ_o is increased by stronger metal-ligand bonding. The effects of ligands on Δ_o follows the general order: pi donors (Cl^-, NR_2^-, H_2O, etc.) < sigma-only donors (NR_3, H-), < pi-acceptors (PR_3, CO, CNR, bipy, or other conjugated organics). The dependence of the metal on Δ_o is also known. Thus, as the principal quantum number increases, the Δ_o is subsequently higher due to the more diffuse nature of the 4d- and 5d orbitals relative to 3d-orbitals gives greater overlap with ligand orbitals.[2] So, 3d metal complexes can be either LS or HS, while octahedral 4d and 5d metal complexes are always low-spin.[2] Also, as the oxidation state of the metal ion increases, the more highly-charged metal ion exhibits shorter bonds to its ligands, thus increasing Δ_o.[2]

In certain combinations of ligands and d^4-d^7 transition metals ions, Δ_o approximately matches the pairing energy, Π_c. In these cases, it is possible to coerce the complex to change spin states (to undergo spin crossover, SCO) by application of some external perturbation such as changing temperature, or pressure, by irradiation with visible light, or by application of either magnetic or electric fields. The change in spin

state also changes the magnetic, optical (color, reflectivity), electric, and mechanical properties of the material. So, there is immense interest in these materials for potential use in various technological applications.

Of the external perturbations, the influence of temperature on the spin state changes in SCO complexes has been most studied. Increasing temperatures lead to increased metal-ligand bond stretching and favor high spin states, since the population of e_g* orbitals leads to longer bond distances due the σ-antibonding nature of these orbitals. Also, the greater entropy associated with the increase in quantum exchange energy, Π_e, of the unpaired electron arrangement versus the LS state help to stabilize the high-spin state at high temperature.[4] In fact, the heat evolved, or consumed, during spin-crossover can be monitored by Differential Scanning Calorimetry (DSC), and can be used to determine the changes in enthalpy and entropy associated with spin transitions.[5] The temperature dependence of the spin crossover generally gives the profiles shown in Figure 1.2. Here, γ_{HS} refers to the fraction of HS complex in the sample as determined

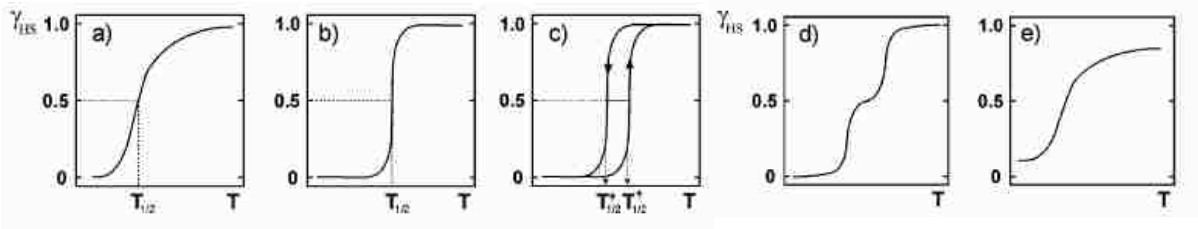

Figure 1.2. Temperature vs. HS fraction (Y_{HS}) plots of 5 main types of SCO events: a) gradual but complete b) abrupt c) abrupt with thermal hysteresis d) two-step e) gradual but incomplete. $T_{1/2}$ is the temperature at which the ratio of HS to LS states is 1:1. Illustrations taken from reference 1.

from magnetic, optical, or other data characteristic of one of the spin states. The plots are also characterized by a reference temperature, $T_{1/2}$, that corresponds to the temperature where the sample achieves a 50% high spin composition. The SCO can occur gradually, and either completely (Figure 1.2a) or incompletely (Figure 1.2e). The gradual SCO behavior is observed for SCO complexes in solution and often in solid state. Both cases are potentially useful in sensing applications. The other three profiles are found exclusively in solid state materials. The SCO is characterized as 'abrupt' if it occurs over a narrow temperature range (Figure 1.2b), a behavior useful for switching applications.[1] The SCO can sometimes occur in multiple steps (Figure 1.2d). Finally, in a few instances the temperature at which SCO occurs on cooling, $T_{1/2}\downarrow$, is different than that on warming, $T_{1/2}\uparrow$, so the sample has a thermal hysteresis. This hysteresis introduces a critical memory component to some SCO materials. For practical, normal, memory applications, a 30-50 K hysteresis loop that spans room temperature is desirable. The ability to deliberately design a SCO material to exhibit any one of the behaviors in Figure 1.2 or to control $T_{1/2}$ are still unresolved challenges that need to be addressed in order to create new devices or technologies with predictable properties.

While it is not yet possible to predict thermal spin crossover behavior apriori, examinations of known systems have led to improved understanding. It is generally accepted that the abruptness of the spin transition is a result of cooperativity between neighboring SCO complexes transmitting structural changes throughout the bulk material.[7] The largest structural changes in SCO complexes have been observed for iron(II) with nitrogen donor ligands, whose metal-ligand bonds change by 10-13% during spin-crossover;[7] Fe-N bond lengths are 1.8-2.0 Å for LS Fe(II) but are 2.0-2.2 Å for HS

iron(II).[1] Thus, the large changes in the shape of the spin center during SCO can lead to large rearrangements of the crystal lattice if the sites are close enough. It might be predicted that SCO sites that are connected by the strong covalent bonding, as in coordination polymers, would result in the highest degree of cooperativity. However, it has been found that spin transitions mediated by secondary interactions, such as hydrogen bonding or pi-pi interactions, have resulted in the most cooperative SCO systems.[7] Thus, the origin of cooperativity is more complicated than considering direct bonding interactions alone; a more detailed analysis of the structural changes, and all intermolecular interactions within a crystal lattice is required for more penetrating insight into the spin crossover behavior.[7] Finally, it has been observed that those complexes with thermal SCO hysteresis often, but not always, exhibit crystallographic phase changes.

The first relation made between crystal packing and cooperativity was demonstrated in a series of $[Fe(NCS)_2(PM\text{-}R)_2]$ (R = phenyl group) by Guinonneau and coworkers. They found that the short C-H···S contacts (2.8 Å) from the aromatic R groups of one molecule interacted closely with its neighboring isothiocyanate ligand (Figure 1.3).[7] In two isostructural polymorphs, they found that cooperativity was not strongly influenced by the pi-pi interactions of the ligand, instead, was correlated with the length of the intermolecular hydrogen bond to one of the ligand O-donor atoms.[7] The polymorph with short intermolecular contacts resulted in an abrupt hysteresis loop from 5-70 K, one of the widest hysteresis loops known to date.[7] Where this intermolecular interaction was not present, a gradual SCO behavior was observed instead.

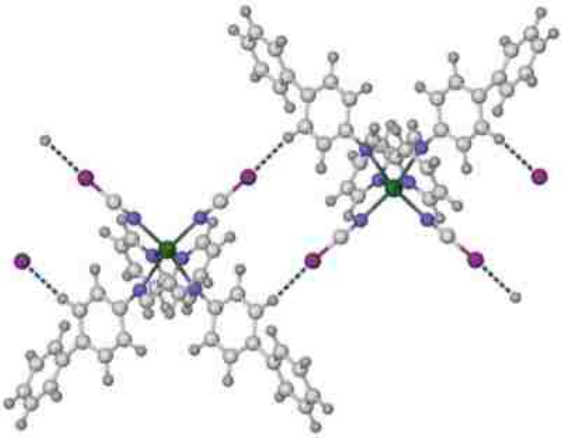

Figure 1.3. Partial packing diagram of $Fe(NCS)_2(PM\text{-}R)_2]$ (R=biphenyl) in its high spin state, showing the short intermolecular C-H…S contacts promoting strong cooperativity (Fe = green, N = blue, S = magenta). Figure from reference 7.

Strong intermolecular interactions have been identified as a main contributor towards cooperativity. Iron(II) complexes with 1,2,4-triazoles (Figure 1.3, left) yields linear coordination polymers, $[Fe(Rtz)_3]X_2 \cdot nH_2O$, where R = H, NH_2, C_2H_4OH, X^- = anion (Figure 1.4, right).[7]

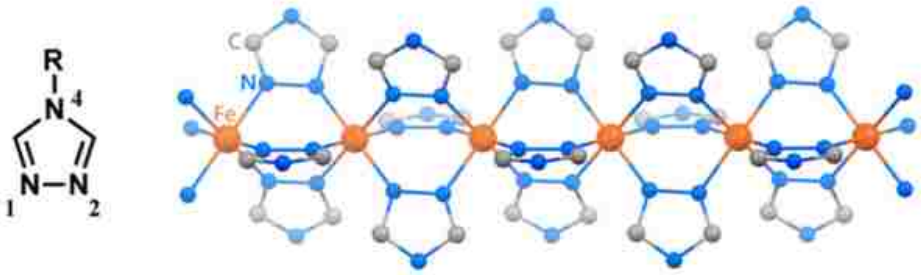

Figure 1.4. Structure of 4-R-1,2,4 triazole (left) and one-dimensional coordination polymer chains of $[Fe(Rtz)_3]^{2+}$ (right). Figure from reference 8.

These compounds undergo SCO with wide hysteresis loops of 20-40 K.[7] Controlling the temperature of SCO is highly dependent on the triazole substituent, anion, and water content, all which impact the subsequent hydrogen bonding interactions. While these structures lack any covalent linkages between the coordination polymer chains, single crystal and powder diffraction data of the iron and analogous copper complexes have confirmed extensive hydrogen bonding interactions between the polymer chains, involving the acidic triazole C-H groups and/or substituent R, with the counter-ion and water.[7] The intermolecular interactions within (and between) the polymer chains have been noted as the main contributor towards hysteric SCO transitions in these systems.[7] This class of compounds have been significant in the development of device applications, and were the first SCO materials to show hysteresis centered at room temperature. While these complexes are significant, their poor crystalline nature has made their structural determinations challenging and their low solubility render their processing difficult.[7] The development of new SCO compounds with straightforward synthesis and characterization techniques is crucial in understanding the complicated role of structure on magnetic behavior.

Tris(pyrazol-1-yl)borates (Tp^x) and Tris(pyrazol-1-yl)methanes (Tpm^x), recognized as "scorpionate" ligands (with x substituents replacing hydrogen on the pyrazolyls), have been a widely-explored ligand scaffold for iron(II) SCO chemistry because they provide structurally diverse compounds with convenient syntheses.[9] The first example, $Fe[(HB(pz)_3 = Tp]_2$ (pz = pyrazol-1-yl), prepared by Trofimenko in 1967 had unusual magnetic behavior.[10,11] Samples purified by sublimation showed SCO and apparent hysteresis, Figure 1.5. On first heating, the sample remained low spin

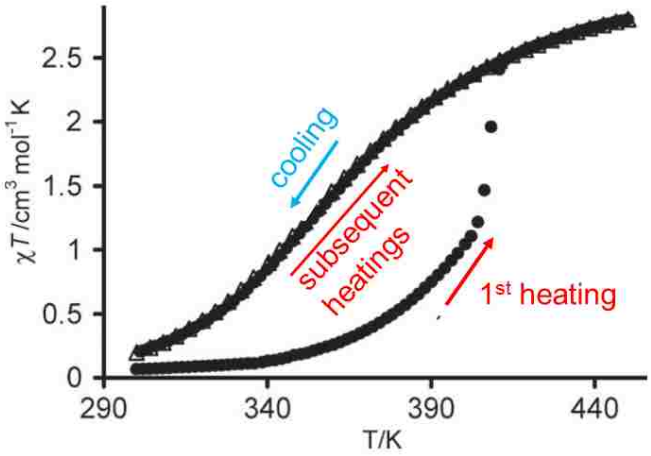

Figure 1.5. Temperature dependence of the magnetic properties of $FeTp_2$, adapted and modified from reference 12.

above room temperature, then showed an abrupt SCO near 400K. Upon cooling, a gradual SCO with $T_{1/2}\downarrow$ near 365 K was found. Subsequent cycles followed the cooling curve. It was later shown that this unusual behavior was due to an irreversible phase change from a metastable tetragonal crystal system (with unknown structure) formed during sublimation to the thermodynamically stable monoclinic system (for which low and high temperature structures are known).[12] These unusual magnetic properties were taken advantage of in the construction of read-only memory devices.[11] Afterward, the magnetic properties of other variants with different substituents around the scorpionate were examined. In contrast with $FeTp_2$ which is low spin at room temperature, those with sterically-demanding methyl substituents in pyrazolyl 3-positions (near the metal), $Fe[(HB(pz^*)_3 = Tp^*]_2$ (pz^* = 3,5-dimethylpyrazolyl) and $FeTp^{**}_2$ (containing 3,4,5-trimethylpyrazol-1-yls) were HS at room temperature because steric congestion favored elongated Fe-N bonds.[13,17] Interestingly, the temperature-dependent magnetic behaviors of $FeTp^*_2$ and $FeTp^{**}_2$ are dramatically different, Figure 1.6. The compound $FeTp^*_2$

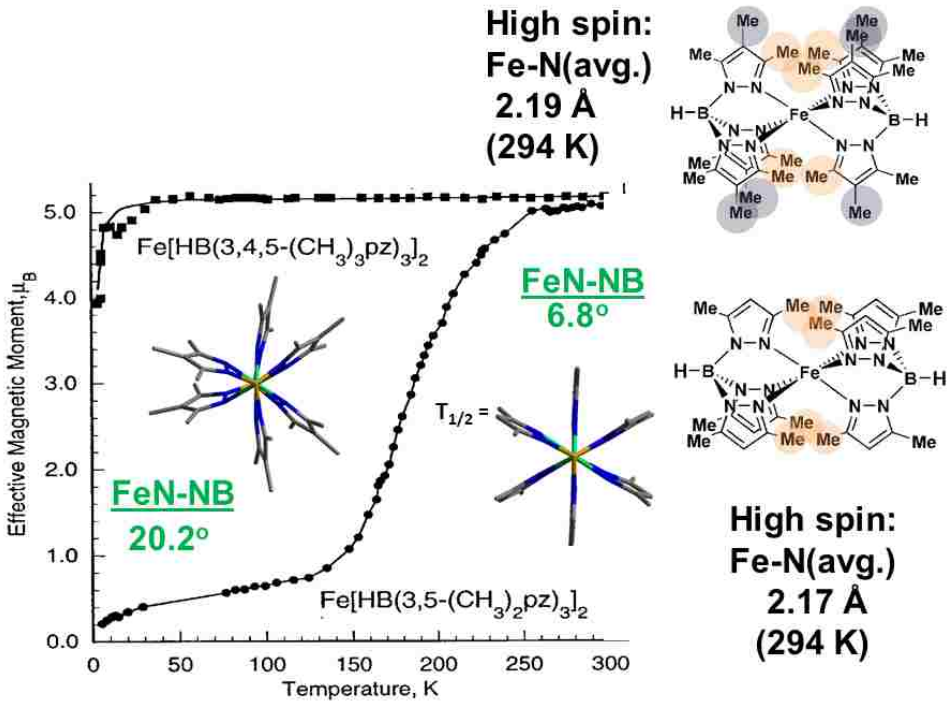

Figure 1.6. Comparison of structures and temperature dependence of $FeTp^*_2$ and $FeTp^{**}_2$.

undergoes a somewhat abrupt SCO near 200 K, while $FeTp^{**}_2$ remains high spin at all temperatures. The difference in the two compounds is related to the amount of pyrazolyl ring twisting, measured by the FeN-NB torsion angle (left of Figure 1.7). On average the rings in $FeTp^*_2$ are twisted by 7° whereas in $FeTp^{**}_2$ the ring twisting approaches 21°. It is noted that other groups have used a different torsion angle FeN-NC (right of Figure 1.7) which corresponds to pyrazolyl ring-tilting to evaluate the distortions in a Tp^x type ligand. A subsequent evaluation of the SCO behavior of all known $FeTp^x_2$ compounds as of 2005, revealed an empirical "11 degree rule"; if the average pz-twisting was greater than 11°, then the ligand will be too distorted to undergo SCO and revert to LS.

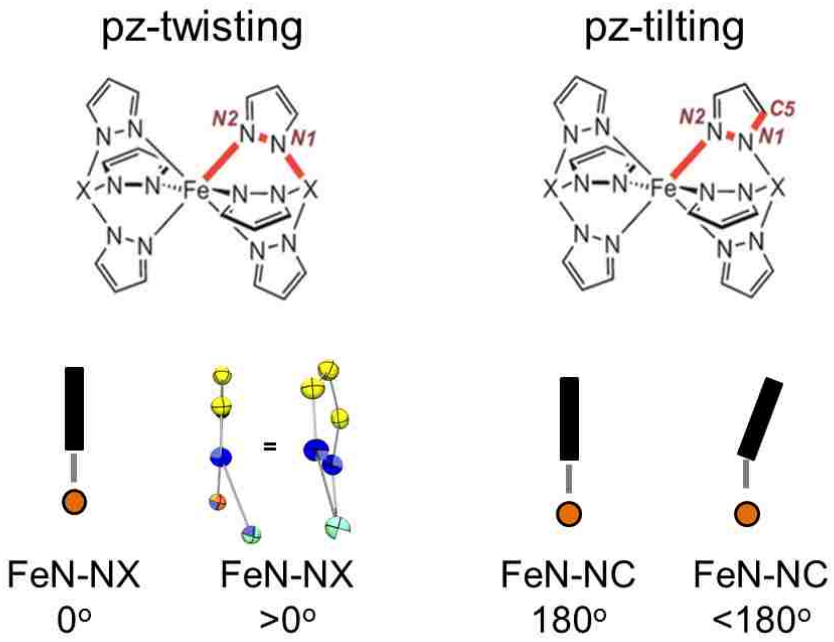

Figure 1.7. Depiction of the two different torsions used to evaluate the degree of pyrazolyl ring twisting in $[Fe(Tp^x)_2]$ and in $[Fe(Tpm^x)_2]^{2+}$ (X = BH or CH). The chem-draw part of this figure is used from reference 6. The orange ball is in the bottom represents either the B-H bond in Tp^x or the C-H methine bond in Tpm^x.

The SCO behavior of $[Fe(Tpm^x)_2]^{2+}$ complexes mirrors the borate counterparts in many ways, but the ionic nature and inclusion of different anions in the crystal lattice and greater propensity of inclusion of solvate molecules can greatly impact the properties. The parent complex $\{Fe[(HC(pz)_3 = Tpm]_2\}(BF_4)_2$ (pz = pyrazol-1-yl) is LS at room temperature and undergoes a somewhat abrupt SCO to HS near 400 K, very much like the first heating cycle of $FeTp_2$.[12] In this case however, no crystallographic phase change is observed and the SCO is simple.

Analysis of $Fe[Tpm^*]_2(BF_4)_2$ showed an abrupt SCO at 203 K but the transition was only 50% complete due to a crystallographic phase change (figure 1.8, left).[14] The

high-spin state contained one, symmetric Fe(II) center.[15a,b] However, two distinct iron sites were present when cooled, one site had a very twisted rings (pz twist 24°) and was high

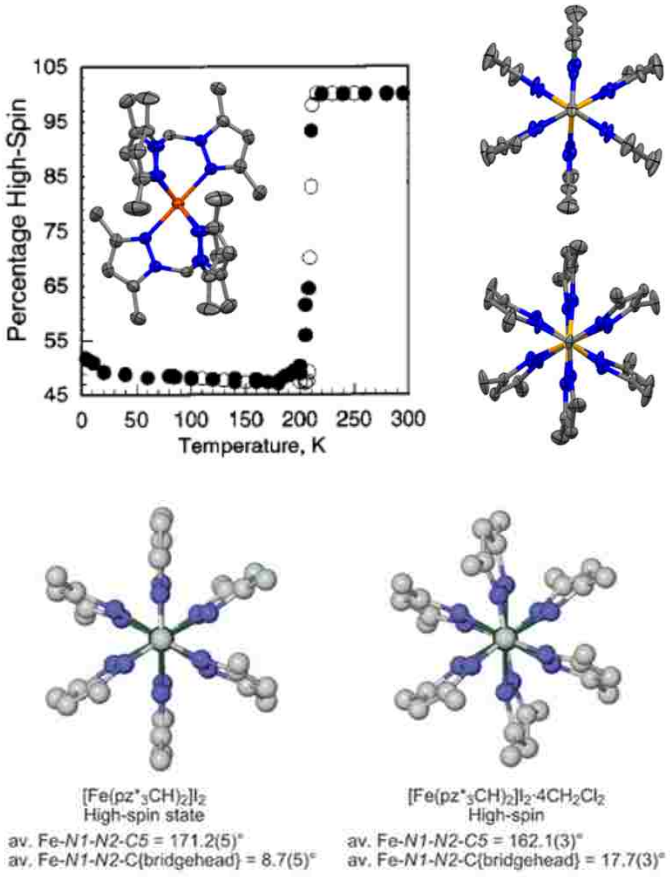

Figure 1.8. Top: Magnetic data and structures of $[Fe(Tpm^*)_2](BF_4)_2$. Bottom: Comparison of structures of $[Fe(Tpm^*)_2](I)_2$-xCH_2Cl_2 (x = 0, left; x = 4, right) Top figure adapted from reference 15, while bottom is from reference 6.

spin while the other site had lesser twisting (3°) and was converted to low-spin. Analysis of corresponding nickel and cobalt complexes that do not undergo spin crossover, showed the same phase change. Thus it was concluded that the crystallographic phase change caused the spin crossover. When the anion was switched to iodide, inconsistent spin behavior was observed between two crystal structures of $Fe[(HC(pz^*)_3 = Tpm^*]_2\,I_2$

(pz = 3,5-dimethylpyrazolyl), solvated (4 CH_2Cl_2) and un-solvated. Interestingly, the solvent-free form underwent an abrupt SCO at 203 K with a hysteresis width of 15 K, while the solvated crystals were high-spin at all temperatures.[13] An analysis of the solid-state structures revealed deviations from the idealized symmetry due to pyrazolyl tilting and twisting. While the torsion angles (Fe-N2-N1-C5) would normally be 180° for C_{3v} symmetry, the high-spin form of the solvent-free $Fe[Tpm^*]_2 I_2$ displayed an average torsion angle of 171.2°, less tilted than that of the high-spin solvate at 162.1° (left and middle, Figure 1.5). Twisting of the solvent free complex of 9° was much less than the 18° for the CH_2Cl_2 tetrasolvate, showing that the "11° rule" seems to work well for Tpm^x complexes as well .[13] The Murray group was able to make the mixed scorpionate complex, $[Fe(Tpm)(Tpm^*)](BF_4)_2$. Interestingly this compounds crystallized as two polymorphs where each polymorph exhibited unique SCO behavior (Figure 1.9).

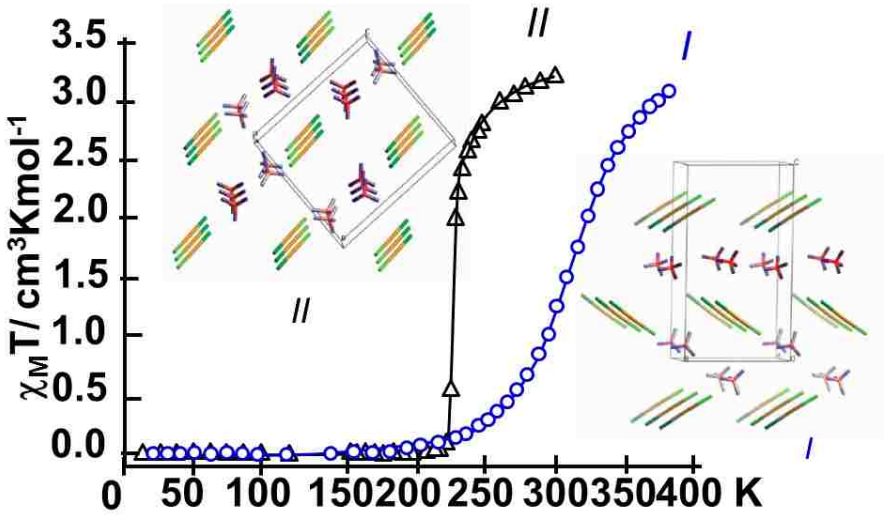

Figure 1.9. Magnetic behavior and structures of two polymorphs of $[Fe(Tpm)(Tpm^*)](BF_4)_2$, adapted from reference 17.

Thus, common features in SCO behavior of iron(II) scorpionates is that both crystal packing and pyrazolyl ring twisting govern magnetic behavior. Moreover, the Goodman group also summarized a limitation in the design of any new iron(II) scorpionates for SCO applications in that "…any substituents in the 3-position that are much larger than a methyl destroy any hope of observing spin state crossover behaviour and essentially lock the complex into the HS form."[18]

With these observations in mind, new N-confused tris(pyrazolyl)methane ligands were developed, in which one of the three pyrazolyls is attached to the sp^3 methine carbon via a carbon, rather than nitrogen. With this substitution pattern, it may be possible to use nitrogen protection and deprotection reactions on the 'confused' pyrazolyl to modify the steric environment about the metal. This strategy may allow for rapid screening to test whether groups larger than a methyl could indeed provoke SCO, if only two of the six pyrazolyls are being modified. Also, these reactions may allow for means to change spin states in solution to give indicators or sensors. Finally, it may be possible to use properly chosen X groups such as H, or 4-pyridyls to direct the solid-state assemblies of the SCO complexes though hydrogen bonding or coordination bonds. In the initial study of these ligands, $[Fe(^{X}L)_2](BF_4)_2$ (X = H, Bn ($CH_2C_6H_5$) or Ts (p-$SO_2C_6H_4CH_3$), L=pzCH$(pz)_2$) were prepared and the magnetic properties of subsequently studied.[19] The complex $[Fe(^{Ts}L)_2](BF_4)_2$ stayed HS at all temperatures.[17] Interestingly, $[Fe(^{Bn}L)_2](BF_4)_2 \cdot 2CH_3CN$ displayed SCO in the solid ($T_{1/2}$ at 90 K) but the solvate free complex (of unknown structure) remained HS at all temperatures.[17] The complex $[Fe(^{H}L)_2](BF_4)_2$ exhibited a gradual SCO above room temperature with $T_{1/2}$ near 360 K. This latter result was a somewhat disappointing since it was hoped that hydrogen bonding

to the BF_4^- anions would give rise to abrupt spin transitions. Examination of the structure showed that the anion was disordered over two closely spaced orientations, both within van der Waals contact with the N-H group. The observation of the disorder may be an indication of the weakness for the hydrogen bonding interaction.

As discussed above, understanding the molecular properties that influence highly-cooperative SCO behavior is critical in the development of new electronic materials. The purpose of this thesis work is to more fully examine whether hydrogen bonding interactions can be used to assemble iron(II) scorpionate complexes and whether this leads to abruptness in the SCO behavior. In addition, since the SCO of $[Fe(^{H}L)_2](BF_4)_2$ is well above room temperature, means to reduce the $T_{1/2}$ by increasing steric bulk of the 'normal' pyrazolyls will be evaluated. Chapter one describes the preparation of two new N-confused C-scorpionates, $^{Ts}L^*$ and $^{H}L^*$, each with two 'normal' 3,5-dimethylpyrazolyl groups, and either an N-tosyl or N-H group on the 'confused' pz. Also described in this first chapter are the silver complexes of the (^{X}L) ligands which are subsequently used as stoichiometric ligand transfer reagents to different transition metals. The silver complexes are also examined for their potential as catalysts for nitrene transfer reactions.

The second chapter will discuss the solution- and solid-state properties of the iron(II) N-confused C-scorpionate complex, $[Fe(^{H}L^*)_2](OTf)_2$, which unexpectedly displayed multiple solid-state structures and solvates. The synthesis, solid-state characterization, and SCO behavior of both compounds will be described in detail. Lastly, the final chapter provides conclusions and details future work that will further delineate how the SCO behavior of iron(II) N-confused C-scorpionates is influenced by

the hydrogen bonding interactions, different solvents, counter-ions, or other hydrogen-bond donors.

Chapter 2

SILVER(I) TRIFLUOROMETHANESULFONATE COMPLEXES OF N-CONFUSED C-SCORPIONATES

2.1 INTRODUCTION

Scorpionate ligands, which originally referred to Trofimenko's tris(pyrazolyl)borates, Tp^x,[20] are ubiquitous in modern coordination chemistry. The "scorpionate" moniker is also used to classify other facial tri-chelating ligands[20b] such as Reglinski's tris(thioimidazolyl)borate, Tm^R (aka "soft" scorpionates),[21] and C-scorpionate counterparts such as tris(pyrazolyl)methane, Tpm^x,[22] and tris(pyrazolyl)methanesulfonate, Tpms.[23] The chemistry of silver(I) scorpionates has seen tremendous growth in the last 15 years, ever since the subject was first reviewed.[24],[25] At the time of the 2004 review, the chemistry of these derivatives was still in its infancy because first-generation scorpionates with B-H bonds had a proclivity for reducing silver(I) to the metal. It was learned on the late 1990's that silver reduction could be slowed by increasing steric bulk on the pyrazolyls, by removing B-H bonds, and/or by introducing electron withdrawing groups on the pyrazolyl rings.[25] Intensified interest in silver(I) scorpionates began with early reports from the Dias group that showed that the fluorinated scorpionate complex, $AgTp^{(CF3)2}$, was a competent catalyst for carbene insertions into C-halogen bonds,[26] aromatic C=C bonds (Büchner reaction),[27] and aliphatic C-H bonds.[28] Further inciting interest were reports from the Pérez group that showed $AgTp^x$ complexes catalyzed a variety of transformations[25] such as carbene insertions into alkane C-H bonds,[29] Si-H bonds,[30] and C-X (X = Cl, Br) bonds,[31] or for

cross coupling of diazo- compounds.[32] Moreover, diverse $AgTp^X$ catalyzed nitrene transfer reactions have been discovered such as aziridination of alkenes,[33] dienes,[34] amination of alkanes,[35] and unexpected N-N bond formations.[36] More recently, other silver scorpionates such as Huang's $Ag(PPh_3)(^{Ph}Tm)$[37] and Perez's $Ag[PhB(CH_2PPh_2)_3](PPh_3)$[38] were also found to catalyze the aziridination of styrene, albeit in much lower yields than the analogous copper complexes.

In contrast to the $AgTp^x$ and other anionic B-scorpionates, the reaction and catalytic chemistry of AgTpms[39] or $[Ag_n(Tpm^x)_m]^+$ [40,41] remains largely unreported. The chemistry of $[Ag_n(Tpm^x)_m]^+$ compounds lagged behind the Tp^x derivatives in part because of difficulties in the original ligand synthesis,[42] that were only resolved in 1984 by Elguero and co-workers.[43] Large-scale syntheses and subsequent functionalization chemistry of tris(pyrazolyl)methanes were then introduced in 2000.[44] These breakthroughs opened the door for countless new variations including Tpms.[42] Given remarkable achievements reported by various groups in the use silver complexes of charge neutral N-donors to effect both aziridination and amination reactions,[43,48] similar chemistry might be expected for tris(pyrazolyl)methanes but, surprisingly, has not yet been reported for this ligand.[48]

Our group has recently introduced a new class of tris(pyrazolyl)methane, the N-confused C-scorpionate[43] where one of the three pyrazolyl rings is bound to the central methine carbon via a pyrazolyl ring carbon atom rather than the more usual

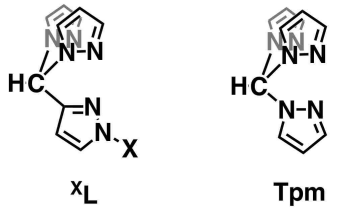

^{X}L Tpm

Figure 2.1. Depiction of 'N-confused' C-scorpionates (left, X = H, Bz = $CH_2C_6H_5$, Ts = SO_2(p-tolyl)) versus the 'normal' C-scorpionate, tris(pyrazolyl)methane, Tpm, (right).

nitrogen atom, Figure 2.1. With this mode of linkage, easy access to variable steric and electronic properties of the ligands can be gained by any variety of simple N-protection and deprotection reactions. Importantly, by suitable choice of the confused pyrazolyl's X-group it should be possible to promote favorable supramolecular interactions in the second coordination sphere of a complex to either guide crystallization or facilitate reactions. In this contribution, the preparation of new N-confused C-scorpionate ligands with two 'normal' pz* groups (= 3,5-dimethylpyrazol-1yl) and a 'confused' pyrazolyl with either an N-H, ^{H}L*, or an N-Tosyl (Tosyl = p-toluenesulfonyl), ^{Ts}L*, bound to a central methine carbon is described. These bulky ligands complement those previously described, ^{H}L and ^{Ts}L, that had less-bulky, unsubstituted, 'normal' pyrazol-1-yls. For these four related N-confused scorpionate ligands, the 2:1 and 1:1 ligand:silver complexes are prepared and characterized both structurally and spectroscopically. The complexes' stoichiometric reactivity and catalytic activity for aziridination of styrene is also reported.

2.2 EXPERIMENTAL

General Considerations. The compounds (*p*-$CH_3C_6H_4SO_2$ = Ts)pzC(O)H, ^{Ts}pzCHpz$_2$ (^{Ts}L), and ^{H}pzCHpz$_2$ (^{H}L) were prepared as described previously.[50] The compound O=C(pz*)$_2$ was prepared by the literature method.[51] Anhydrous $CoCl_2$, Ag(trifluoromethanesulfonate = OTf), $Mn(CO)_5Br$, Fe, $Fe(OTf)_2$, $FeCl_2$, $PhI(OAc)_2$, H_2NTs, and styrene were purchased from commercial sources and used as received. Anhydrous $Fe(OTf)_2$, $CoCl_2$, and AgOTf were stored under argon in a drybox. Commercial solvents were dried by conventional means and distilled under a nitrogen atmosphere prior to use. The silver(I), manganese(I), and iron(II) complexes were prepared under argon using Schlenk line techniques, however, after isolation, were stored and manipulated under normal laboratory atmospheric conditions, unless otherwise specified (see catalysis section).

Instrumentation. Midwest MicroLab, LLC, Indianapolis, Indiana 45250, performed all elemental analyses. Melting point determinations were made on samples contained in glass capillaries using an Electrothermal 9100 apparatus and are uncorrected. IR spectra were recorded for samples as KBr pellets or as either solutions or Nujol mulls between KBr plates in the 4000-500 cm^{-1} region on a Nicolet Magna-IR 560 spectrometer or on solid samples using a Thermo Scientific Nicolet iS5 IR spectrometer equipped with an iD3 Attenuated Total Reflection (ATR) accessory. ^{1}H, ^{13}C, ^{19}F NMR spectra were recorded on a Varian 400 MHz spectrometer. Chemical shifts were referenced to solvent resonances at δ_H 7.26 and δ_C 77.23 ppm for $CDCl_3$ or δ_H 1.94 and δ_C 118.26 for CD_3CN. Abbreviations for NMR and UV-Vis: br (broad), sh (shoulder), m (multiplet), ps

(pseudo-), s (singlet), d (doublet), t (triplet), q (quartet), p (pentet), sept (septet). Solution magnetic moment were measured by the Evan's method.[52] Magnetic susceptibility data were collected on a Quantum Design MPMS3 SQUID magnetometer. Raw moment data were corrected for sample shape and radial offset corrections using the MPMS 3 Sample Geometry Simulator.[53] Diamagnetic corrections of -218×10^{-6} emu/mol for **9**, calculated from tabulated Pascal's constants[54] Were applied to the measured susceptibility data, as appropriate. Electronic absorption (UV-Vis/NIR) measurements were made on a Cary 5000 instrument. Powder X-ray diffraction patterns were collected with a Rigaku MiniFlex II instrument using Cu Ka (1.54178 Å) radiation. ESI(+) mass spectrometric measurements were obtained on a Micromass Q-TOF spectrometer where formic acid (ca. 0.1 % v:v) was added to the mobile phase (CH_3CN).

A. Ligands

^{Ts}pzCHpz*$_2$, **^{Ts}L***. A mixture of 2.132 g (8.511 mmol) ^{Ts}pzC(O)H, 2.092 g (9.585 mmol) O=C(pz*)$_2$, and 0.055 g (0.43 mmol) $CoCl_2$ in 50 mL toluene was heated at reflux 16 h. The resulting blue mixture was cooled to room temperature and solvent was removed by vacuum distillation. The residue was partitioned between 100 mL H_2O and 100 mL ethyl acetate. The layers were separated and the aqueous layer was extracted with two 50 mL portions CH_2Cl_2. The organic fractions were combined, dried over $MgSO_4$, and filtered. Solvents were removed by vacuum distillation to leave 3.29 g (91%) of ^{Ts}L* as a pale yellow solid. Recrystallization by cooling a boiling supersaturated solution in MeOH to room temperature gave crystalline ivory-tinted blocks (ca. 25 mg/mL) after filtration and drying under vacuum. Mp: 181-182 ^{o}C. IR (CH_2Cl_2, KBr) ν_{CH} = 3141, 2971, 2856; IR

(ATR) ν_{CH} = 3195, 3163, 3146, 3051, 2973, 2923; ν_{SO} = 1374 (asym) ,1179 (sym) cm^{-1}. ^{1}H NMR (CD_3CN) δ_H 8.19 (d, *J* = 2.8 Hz, 1 H, H_{5cpz}), 7.81 (d, *J* = 8.4 Hz, 2 H, Ts), 7.48 (s, 1 H, $H_{methine}$), 7.41 (d, *J* = 8.4 Hz, 2 H, Ts), 6.35 (d, *J* = 2.8 Hz, 1 H, H_{4cpz}), 5.83 (s, 2 H, H_{4pz*}), 2.42 (s, 3 H, $TsCH_3$), 2.07 (s, 6 H, pz*CH_3), 2.05 (s, 6 H, pz*CH_3) ppm. ^{13}C NMR (CD_3CN) δ_C 155.42, 149.14, 147.85, 141.71, 134.64, 133.72, 131.23, 128.84, 110.98 (C_{4cpz}), 107.56 (C_{4pz*}), 69.44 ($C_{methine}$), 21.71 (TsMe), 13.61 (pz*Me), 11.44 (pz*Me) ppm.

^{H}pzCHpz*$_2$, ^{H}**L***. A solution of 15.0 mL 5.00 M NaOH (aq) (75.0 mmol), 3.29 g (7.75 mmol) TsL*, and 20 mL THF was heated at reflux 1.25 h. The solution was allowed to cool to room temperature and then was extracted with two 50 mL portions EtOAc. The organic fractions were dried over $MgSO_4$ and filtered. The organic solvent was removed by vacuum distillation and the residue was triturated with Et_2O to leave 1.61 g (77%) ^{H}**L*** as a colorless solid. Mp: 146-147 ^{o}C. IR (CH_2Cl_2, KBr) ν_{NH} = 3450, ν_{CH} = 3054 2986, 2857; IR (ATR) ν_{CH} = 3141, 3051, 2971, 2956, 2914 cm^{-1}. ^{1}H NMR (CD_3CN) δ_H 11.25 (br s, 1 H, N-H), 7.56 (d, *J* = 2.3 Hz, 1 H, H_{5cpz}), 7.55 (s, 1 H, $H_{methine}$), 6.15 (d, *J* = 2.3 Hz, 1 H, H_{4cpz}), 5.86 (s, 2 H, H_{4pz*}), 2.21 (s, 6 H, pz*CH_3), 2.07 (s, 6 H, pz*CH_3) ppm. ^{13}C NMR ($CDCl_3$) δ_C 148.95, 141.59, 107.19 (C_{4pz*}), 106.11 (C_{4cpz}), 69.20 ($C_{methine}$), 13.65 (pz*Me), 11.52 (pz*Me) ppm; two resonances presumably for quartenary pyrazolyl carbons not observed.

B. Silver Complexes

General Procedure. A solution of a given ligand (ca. 0.5-2.0 mmol) in 10 mL THF was added to a solution of AgOTf (1 or 0.5 eq) in 10 mL THF by cannula transfer. The flask originally containing the ligand was washed twice with 2 mL THF and the washings were transferred to the reaction medium to ensure quantitative transfer of reagent. After the mixture had been stirred overnight 14 h, the colorless precipitate was collected after cannula filtration, washing the solid with two 2 mL portions Et_2O, and drying under vacuum 30 min. The quantities of reagents used, of products obtained, and characterization data for each of the eight new compounds is given below. An alternative work up in the case where no precipitate was observed (complex **4b**) is also described.

[Ag(^{Ts}L*)](OTf), **1a**. A mixture of 0.306 g (0.721 mmol) ^{Ts}L* and 0.185 g (0.720 mmol) AgOTf gave 0.333 g (68%) of **1a** as a colorless solid after drying under vacuum at 100^{o}C for 4h. Mp: 183-185 ^{o}C, dec. Anal. Calcd. (Found) for $C_{22}H_{24}N_6AgF_3O_5S_2$: C, 38.78 (39.05); H, 3.55 (3.73); N, 12.33 (12.15). IR (ATR) tosyl: 1393 (ν_{as}, SO_2), 911 ($\nu_{S\text{-}N}$); triflate (s to vs): 1260 (ν_{as}, SO_3), 1223 (ν_s, CF_3), 1162 (ν_{as}, CF_3), 1029 (ν_s, SO_3), 638 (ν_s, SO_3) cm^{-1}. ^{1}H NMR (CD_3CN) δ_H 8.20 (d, J = 2.8 Hz, 1 H, H_{5cpz}), 7.78 (d, J = 8.5 Hz, 2 H, Ts), 7.46 (s, 1H, $H_{methine}$), 7.41 (d, J = 8.5 Hz, 2 H, Ts), 6.11 (d, J = 2.8 Hz, 1 H, H_{4cpz}), 6.04 (s, 2 H, H_{4pz*}), 2.42 (s, 3 H, $TsCH_3$), 2.41 (s, 6 H, pz*CH_3), 1.94 (s, 6 H, pz*CH_3) ppm. ^{13}C NMR (CD_3CN) δ_C 154.56, 151.93, 147.93, 143.85, 134.55, 134.10, 131.27, 128.87, 110.48 (C_{4cpz}), 107.32 (C_{4pz*}), 65.11 ($C_{methine}$), 21.75 (TsMe), 14.06 (pz*Me), 11.36 (pz*Me) ppm. ^{19}F NMR (CD_3CN) δ_F -79.32 (s) ppm. ESI(+) MS *m*/*z*

(rel. intensity) [assignment]: 957 (73) $[Ag(^{Ts}L^*)_2]^+$, 531 (36) $[Ag(^{Ts}L^*)]^+$, 447 (7) $[Na(^{Ts}L^*)]^+$, 425 (5) $[H(^{Ts}L^*)]^+$, 329 (100) $[^{Ts}L^* - Hpz^*]^+$. A sample that was dried under vacuum 30 min without heating analyzed as **3b**·THF: Anal. Calcd. (Found) for $C_{26}H_{32}N_6AgF_3O_4S$: C, 41.49 (41.39); H, 4.28 (4.19); N, 11.15 (11.23). X-ray quality single crystals of mostly **1a** and some larger plates of **1b**·MeOH were grown by vapor diffusion of Et_2O into a MeOH solution (1.3 mL, 0.005 M).

$[Ag(^{Ts}L^*)_2](OTf)$, **1b**. A mixture of 0.250 g (0.589 mmol) $^{Ts}L^*$ and 0.0757 g (0.295 mmol) Ag(OTf) gave 0.289 g (89%) of **1b** as a colorless solid. Mp: 201-203 ^oC, dec. Anal. Calcd. (Found) for $C_{43}H_{48}N_{12}AgF_3O_7S_3$: C, 46.70 (46.81); H, 4.37 (4.72); N, 15.20 (15.31). IR (ATR) ν_{NH} = 3154; triflate (s to vs): 1268 (ν_{as}, SO_3), 1224 (ν_s, CF_3), 1172 (ν_{as}, CF_3), 1032 (ν_s, SO_3), 637 (ν_s, SO_3) cm^{-1}. ^1H NMR (CD_3CN) δ_H 8.19 (d, J = 2.8 Hz, 1 H, H_{5cpz}), 7.80 (d, J = 8.4 Hz, 2 H, Ts), 7.46 (s, 1 H, $H_{methine}$), 7.40 (d, J = 8.4 Hz, 2 H, Ts), 6.12 (d, J = 2.8 Hz, 1H, H4cpz), 5.98 (s, 2 H, H_{4pz*}), 2.38 (s, 3H, TsMe), 2.35 (s, 6 H, pz*Me), 1.65 (s, 6H, pz*Me) ppm. ^{13}C NMR (CD_3CN) δ_C 154.81, 151.82, 147.89, 143.63, 134.59, 134.08, 131.35, 128.83, 110.53 (C_{4cpz}), 107.31 (C_{4pz*}), 65.66 ($C_{methine}$), 21.73 (TsMe), 13.63 (pz*Me), 11.36 (pz*Me) ppm. ^{19}F NMR (CD_3CN) δ_F -79.29 (s) ppm. ESI(+) MS *m*/*z* (rel. intensity) [assignment]: 957 (6) $[Ag(^{Ts}L^*)_2]^+$, 531 (7) $[Ag(^{Ts}L^*)]^+$, 425 (9) $[Ag(^{Ts}L^*)\text{-}pz^*]^+$, 329 (100) $[^{Ts}L^* - pz]$. X-ray quality single crystals of **1b**·1.5CH_3CN were grown by vapor diffusion of Et_2O into a CH_3CN solution (1.3 mL, 0.02 *M*). Single crystals of **1b**·MeOH were grown by vapor diffusion of Et_2O into a MeOH solution (1.3 mL, 0.04 M).

[Ag(^{Ts}L)](OTf), **2a**. A mixture of 0.605 g (1.64 mmol) ^{Ts}L and 0.422 g (1.64 mmol) AgOTf gave 0.847 g (82%) of **2a** as a colorless solid. Mp: 141-146 ^{o}C, dec. Anal. Calcd. (Found) for $C_{18}H_{16}N_6AgF_3O_5S_2$: C, 34.57 (34.47); H, 2.54 (2.56); N, 13.44 (13.49). IR (ATR) tosyl: 1389 (ν_{as}, SO_2), 904 ($\nu_{S\text{-}N}$); triflate (s to vs): 1283 (ν_{as}, SO_3), 1237 (ν_s, CF_3), 1223 (ν_s, CF_3), 1163 (ν_{as}, CF_3), 1148 (ν_{as}, CF_3), 1025 (ν_s, SO_3), 634 (ν_s, SO_3) cm^{-1}. ^{1}H NMR (CD_3CN) δ_H 8.23 (d, J = 2.8 Hz, 1H, H_{5cpz}), 7.89 (d, J = 2.4 Hz, 2 H, H_{5pz}), 7.82 (s, 1 H, $H_{methine}$), 7.81 (d, J = 8.4 Hz, 2 H, Ts), 7.59 (d, J = 1.6 Hz, 2 H, H_{3pz}), 7.41 (d, J = 8.4 Hz, 2 H, Ts), 6.39 (dd, J = 2.4, 1.6 Hz, 2 H, H_{4pz}), 6.31 (d, J = 2.8 Hz, 1 H, H_{4cpz}), 2.41 (s, 3 H, $TsCH_3$) ppm. ^{13}C NMR (CD_3CN) δ_C 153.79, 148.10, 142.99, 134.29, 134.27, 132.68, 131.32, 128.91, 110.24 (C_{4cpz}), 107.71 (C_{4pz}), 72.03 ($C_{methine}$), 21.72 (TsMe) ppm. ^{19}F NMR (CD_3CN) δ_F -79.33 (s) ppm. ESI(+) MS *m*/*z* (rel. intensity) [assignment]: 1101 (11) [$Ag_2(^{Ts}L)_2(OTf)]^+$, 845 (100) [$Ag(^{Ts}L)_2]^+$, 475 (87) [$Ag(^{Ts}L)]^+$, 301 (18) [^{Ts}L – Hpz]$^+$. X-ray quality single crystalline needles of **2a** were grown by vapor diffusion of Et_2O into a CH_3CN solution (1.25 mL, 0.03 *M*) over the course of 2 days. In certain cases, when vapor diffusion of more concentrated solutions (1.25 mL, 0.06 *M*) was prolonged over the period of a week, large block crystals of **2b** also formed amidst the majority of needles of **2a**.

[Ag(^{Ts}L)$_2$](OTf), **2b**. A mixture of 0.250 g (0.679 mmol) ^{Ts}L and 0.0872 g (0.339 mmol) AgOTf gave 0.251 g (77%) of **2b** as a colorless solid. Mp: 150-151 ^{o}C, dec. Anal. Calcd. (Found) for $C_{35}H_{32}N_{12}AgF_3O_7S_3$: C, 42.30 (41.99); H, 3.25 (3.31); N, 16.91 (16.54). IR (ATR) tosyl: 1365 (ν_{as}, SO_2), 902 ($\nu_{S\text{-}N}$); triflate (s to vs): 1290 (ν_{as}, SO_3), 1260 (s_s, CF_3), 1220 (ν_s, CF_3), 1174 (ν_{as}, CF_3), 1131 (ν_{as}, CF_3), 1022 (ν_s, SO_3), 638 (ν_s,

SO_3) cm^{-1}. ^1H NMR (CD_3CN) δ_H 8.23 (d, *J* = 2.8 Hz, 1H, H_{5cpz}), 7.82 (br s, *3* H, overlapping H_{5pz} + $H_{methine}$), 7.79 (d, *J* = 8.4 Hz, 2 H, Ts), 7.56 (br s, 2 H, H_{3pz}), 7.40 (d, *J* = 8.4 Hz, 2 H, Ts), 6.36 (dd, *J* = 2.4, 1.6 Hz, 2 H, H_{4pz}), 6.35 (d, *J* = 2.8 Hz, 1 H, H_{4cpz}), 2.40 (s, 3 H, $TsCH_3$) ppm. ^{13}C NMR (CD_3CN) δ_C 154.04, 148.08, 142.50, 134.29, 134.25, 132.05, 131.32, 128.92, 110.18 (C_{4cpz}), 107.67 (C_{4pz}), 72.40 ($C_{methine}$), 21.73 (TsMe) ppm. ^{19}F NMR (CD_3CN) δ_F -79.32 (s) ppm. ESI(+) MS *m*/*z* (rel. intensity) [assignment]: 845 (7) $[Ag(^{Ts}L)_2]^+$, 475 (16) $[Ag(^{Ts}L)]^+$, 391 (13) $[Na(^{Ts}L)]^+$, 369 (4) $[H(^{Ts}L)]^+$, 301 (100) $[^{Ts}L - Hpz]^+$. X-ray quality single crystals were grown by vapor diffusion of Et_2O into a CH_3OH solution (1.25 mL, 0.022 M).

$[Ag(^{H}L^*)](OTf)$, **3a**. A mixture of 0.200 g (0.740 mmol) $^{H}L^*$ and 0.190 g (0.740 mmol) AgOTf gave 0.337 g (86%) of **3a** as a colorless solid. Mp: 186-188 °C, dec. Anal. Calcd. (Found) for $C_{15}H_{18}N_6AgF_3O_3S$: C, 34.17 (34.20); H, 3.44 (3.37); N, 15.94 (15.81). IR (ATR) ν_{NH} = 3157; triflate (s to vs): 1286 (ν_{as}, SO_3), 1222 (ν_s, CF_3), 1168 (ν_{as}, CF_3), 1028 (ν_s, SO_3), 638 (ν_s, SO_3) cm^{-1}. ^1H NMR (CD_3CN) δ_H 11.47 (br s, 1 H, NH), 7.63 (d, *J* = 2.3 Hz, 1 H, H_{5cpz}), 7.49 (s, 1 H, $H_{methine}$), 6.17 (d, *J* = 2.3 Hz, 1 H, H_{4cpz}), 6.01 (s, 2 H, H_{4pz*}), 2.45 (s, 6 H, CH_3pz*), 2.06 (s, 6 H, CH_3pz*) ppm. ^{13}C NMR (CD_3CN) δ_C 151.23 (br), 151.11, 143.03, 107.05 (C_{4pz*}), 106.12 (C_{4cpz}), 64.78 ($C_{methine}$), 14.03 (pz*Me), 11.38 (pz*Me), ppm. ^{19}F NMR (CD_3CN) δ_F -79.34 (s) ppm. ESI(+) MS *m*/*z* (rel. intensity) [assignment]: 905 (29) $[Ag_2(^{H}L^*)_2(OTf)]^+$, 809 (12) $[Ag_2(^{H}L^*)_2OTf - Hpz^*]$, 755 (9) $[Ag_2(^{H}L^*)(^{H}L^*\text{-}H)]^+$, 649 (100) $[Ag(^{H}L^*)_2]^+$, 551 (10) $[Ag(^{H}L^*)_2 - Hpz^*]^+$, 418 (27) $[Ag(^{H}L^*)(CH_3CN)]+$, 377 (73) $[Ag(^{H}L^*)]^+$. X-ray quality single crystals were grown by vapor diffusion of Et_2O into a CH_3CN solution (1.4 mL, 0.04 M).

$[Ag(^{H}L^*)_2](OTf)$, **3b**. A mixture of 0.150 g (0.550 mmol) $^{H}L^*$ and 0.0713 g (0.277 mmol) AgOTf gave 0.170 g (77 %) of **3b** as a colorless solid after drying at 100°C 4h under vacuum. Mp: 181-183 °C, dec. Anal. Calcd. (Found) for $C_{29}H_{36}N_{12}AgF_3O_3S$: C, 43.67 (44.01); H, 4.55 (4.64); N, 21.07 (21.28). IR (ATR) ν_{NH} = 3375; triflate (s to vs): 1283 (ν_{as}, SO_3), 1223 (ν_s, CF_3), 1151 (ν_{as}, CF_3), 1028 (ν_s, SO_3), 636 (ν_s, SO_3) cm^{-1}. ^1H NMR (CD_3CN) δ_H 11.38 (br s, 1 H, NH), 7.61 (d, J = 2.3 Hz, 1 H, H_{5cpz}), 7.50 (s, 1 H, $H_{methine}$), 6.14 (d, J = 2.3 Hz, 1 H, H_{4cpz}), 6.00 (s, 2 H, H_{4pz*}), 2.45 (s, 6 H, CH_3pz*), 1.98 (s, 6 H, CH_3pz*) ppm. ^{13}C NMR (CD_3CN) δ_C 150.98, 142.74, 106.92 (C_{4pz*}), 106.00 (C_{4cpz}), 65.50 ($C_{methine}$), 13.66 (pz*Me), 11.40 (pz*Me), ppm. ^{19}F NMR (CD_3CN) δ_F -79.32 (s) ppm. ESI(+) MS *m/z* (rel. intensity) [assignment]: 647 (100) $[Ag(^{H}L^*)_2]^+$, 418 (2) $[Ag(^{H}L^*)(CH_3CN)]^+$, 377 (23) $[Ag(^{H}L^*)]^+$, 175 (44) [L – pz*]. A sample that was dried under vacuum but without heating analyzed as **3b**·0.5THF·0.5H_2O: Anal. Calcd. (Found) for $C_{31}H_{41}N_{12}AgF_3O_4S$: C, 44.19 (44.04); H, 4.90 (4.75); N, 19.95 (20.08). X-ray quality single crystals were grown by vapor diffusion of Et_2O into a CH_3OH solution (1.3 mL, 0.02 M).

$[Ag(^{H}L)](OTf)$, **4a**. A mixture of 0.196 g (0.915 mmol) ^{H}L and 0.235 g (0.915 mmol) AgOTf gave 0.366 g (85%) of **4a** as a colorless solid. Mp: 175-178 °C, dec. Anal. Calcd. (Found) for $C_{11}H_{10}N_6AgF_3O_3S$: C, 28.04 (28.39); H, 2.14 (2.31); N, 17.84 (17.86). IR (ATR) ν_{NH} = 3154; triflate (s to vs): 1276 (ν_{as}, SO_3), 1224 (ν_s, CF_3), 1167 (ν_{as}, CF_3), 1027 (ν_s, SO_3), 632 (ν_s, SO_3) cm^{-1}. ^1H NMR (CD_3CN) δ_H 11.90 (br s, 1 H, NH), 7.96 (d, J = 2.6 Hz, 2 H, H_{5pz}), 7.93 (s, 1 H, $H_{methine}$), 7.71 (d, J = 2.4 Hz, 1 H, H_{5cpz}), 7.62 (d, J = 1.8 Hz, 2 H, H_3pz), 6.38 (m, 3 H, overlapping $H_{4pz\&4cpz}$) ppm. ^{13}C NMR (CD_3CN) δ_C

143.42 (br), 143.09, 132.70, 131.64, 107.49 (C_{4pz}), 106.49 (C_{4cpz}), 71.70 ($C_{methine}$) ppm. ^{19}F NMR (CD_3CN) δ_F -79.29 (s) ppm. ESI(+) MS *m*/*z* (rel. intensity) [assignment]: 1265 (3) $[Ag_3(^{H}L)_3(OTf)_2]^+$, 1051 (1) $[Ag_3(^{H}L)_2(OTf)_2]^+$, 793 (41) $[Ag_2(^{H}L)_2(OTf)]^+$, 678 (3) $[Ag_2(^{H}L)_2Cl]^+$, 643 (32) $[Ag_2(^{H}L)(^{H}L\text{-}H)]^+$, 579 (4) $[Ag_2(^{H}L)(OTf)]^+$, 535 (95) $[Ag(^{H}L)_2]^+$, 465 (6) $[Ag_2(^{H}L)(Cl)]^+$, 361 (35) $[Ag(^{K}L)]^+$, 323 (100) $[Ag(^{H}L)]^+$. X-ray quality single crystals were grown by vapor diffusion of Et_2O into a CH_3CN solution (1.4 mL, 0.04 M).

$[Ag(^{H}L)_2](OTf)$, **4b**. A mixture of 0.192 g (0.896 mmol) ^{H}L and 0.115 g (0.448 mmol) AgOTf in 20 mL THF gave a solution (no precipitate) after 1 h, so solvent was removed by vacuum distillation. The colorless residue was washed with Et_2O and was dried at 100oC under vacuum 4h to give 0.218 g (71 %) of **4b** as a colorless solid. Mp: 124-126 ^{o}C, dec. Anal. Calcd. (Found) for $C_{21}H_{20}N_{12}AgF_3O_3S$: C, 36.80 (36.44); H, 2.94 (3.12); N, 24.52 (24.50). IR (ATR) $_{NH}$ = 3126; triflate (s to vs): 1276 (ν_{as}, SO_3), 1224 (ν_s, CF_3), 1158 (ν_{as}, CF_3), 1029 (ν_s, SO_3), 637 (ν_s, SO_3) cm^{-1}. ^1H NMR (CD_3CN) δ_H 11.82 (br s, 1 H, NH), 7.91 (d, *J* = 2.6 Hz, 2 H, H_{5pz}), 7.90 (s, 1 H, $H_{methine}$), 7.69 (d, *J* = 2.4 Hz, 1 H, H_{5cpz}), 7.58 (d, J = 1.8 Hz, 2 H, H_3pz), 6.37 (m, 3 H, overlapping $H_{4pz\&4cpz}$) ppm. ^{13}C NMR (CD_3CN) δ_C 142.62, 132.12, 131.55, 107.48 (C_{4pz}), 106.25 (C_{4cpz}), 72.45 ($C_{methine}$) ppm. ^{19}F NMR (CD_3CN) δ_F -79.31 (s) ppm. ESI(+) MS *m*/*z* (rel. intensity) [assignment]: 535 (57) $[Ag(^{H}L)_2]^+$, 362 (5) $[Ag(^{H}L)(CH_3CN)]^+$, 321 (100) $[Ag(^{H}L)]^+$, 147(60) [L-Hpz]. X-ray quality single prism crystals of **4b**·acetone·H_2O were obtained by evaporation of a solution of mixture of acetone and water. The crystals analyzed as **4b**·acetone·H_2O Anal. Calcd. (Found) for $C_{23}H_{26}N_{12}AgF_3O_{4.5}S$: C, 37.86 (37.77); H, 3.71

(3.62); N, 22.07 (22.38). Under other most other conditions (1,2-dichloroethane solutions, evaporation of THF or CH_2Cl_2 solutions, vapor diffusion of pentane into THF or acetone solutions, of Et_2O into CH_3CN or MeOH solutions, layering hexane onto acetone solutions) a mixture of mainly very long (>2 mm), highly crystalline, but extremely thin needles of **4b**·solvate were obtained along with a few plates of **4a**. After drying under vacuum at room temperature (and exposure to air) these analyzed as **4b**·solvate·H_2O. Example: Anal. Calcd. (Found) for **4b**·CH_3CN·H_2O, $C_{23}H_{25}N_{13}AgF_3O_4S$: C, 37.11 (37.44); H, 3.38 (3.12); N, 24.46 (24.50).

C. Reactions

General Procedure for Preparation of tricarbonylmanganese(I) complexes. Under an argon atmosphere and with exclusion of light (Al foil wrapped apparatus), a mixture of $Mn(CO)_5Br$ and [Ag(L)](OTf) (1 eq) in 10 mL CH_3CN were heated at reflux 3 h during which time a precipitate formed. The solution was filtered, CH_3CN was removed under vacuum and the yellow residue was washed with two 2 mL portions Et_2O and was dried under vacuum. The yellow solids are slightly light sensitive, so they are best stored in the dark (Al foil wrapped vials). The quantities of reagents used, of products obtained, and characterization data for each of the four new compounds is given below.

[*fac*-$Mn(CO)_3(^{Ts}L^*)$](OTf), **5**. A mixture of 0.127 g (0.186 mmol) **1a** and 0.0512 g (0.186 mmol) $Mn(CO)_5Br$ gave 0.118 g (89%) **5** as a yellow solid. Mp: > 210 ^oC. Anal. Calcd. (Found) for $C_{25}H_{24}N_6F_3MnO_8S_2$: C, 42.14 (41.97); H, 3.39 (3.43); 11.79 (11.54). IR: ν_{CO} (ATR) = 2038, 1931; tosyl: 1396 (ν_{as}, SO_2), 903(ν_{S-N}); triflate (CH_2Cl_2/KBr, s to

vs): 1252 (ν_{as}, SO_3), 1203 (ν_s, CF_3), 1153 (ν_{as}, CF_3), 1026 (ν_s, SO_3), 630 (ν_s, SO_3) cm^{-1}. ^1H NMR (CD_3CN, 333 K) δ_H Two species in a 5:1 ratio: Major, 8.49 (br s, 1 H, H_{5cpz}), 7.78 (d, J = 7.5 Hz, 2 H, Ts), 7.61 (s, 1 H, $H_{methine}$), 7.43, (d, J = 7.5 Hz, 2 H, Ts), 7.17 (br s, 1 H, H_{4cpz}), 6.15 (s, 2 H, H_{4pz*}), 2.52 (s, 6 H, pz*CH_3), 2.50 (s, 6 H, pz*CH_3), 2.42 (s, 3 H, TsCH_3); Minor, 7.89 (s, 1 H, $H_{methine}$), 6.90 (s, 1 H, H_{5cpz}), 6.12 (s, 2 H, H_{4pz*}), 5.42 (s, 1 H, H_{4cpz}); Ts and pz*CH_3 protons not observed- overlapping major resonances) ppm. ^{13}C NMR (CD_3CN) δ_C, only resonances for major species given: 221.30 (CO), 220.86 (CO), 157.40, 153.84, 149.33, 145.27, 142.11, 133.84, 131.76, 128.79, 111.61 (C_{4cpz}), 110.16 (C_{4pz}), 60.86 ($C_{methine}$), 21,78 (TsMe), 15.15 (pz*Me), 11.45 (pz*Me) ppm; resonance for CF_3 not observed. ^{19}F NMR (CD_3CN) δ_F -78.87 (s) ppm. ESI(+) MS *m*/*z* (rel. intensity) [assignment]: 563 (100) $[Mn(CO)_3(^{Ts}L*)]^+$, 497 (19) $[Mn(H_2O)(^{Ts}L*)]$, 433 (5) $[Mn(CO)_3(^{Na}L*)]^+$. UV-Vis [CH_3CN], λ, nm (ε, $M^{-1}cm^{-1}$): 359 (2430). Twinned needle crystals were grown by heating a mixture of 50 mg **5** in 0.5 mL MeOH to dissolution, then cooling the solution to room temperature.

[*fac*-$Mn(CO)_3(^{Ts}L)$](OTf), **6**. A mixture of 0.200 g (0.320 mmol) **2a** and 0.088 g (0.320 mmol) $Mn(CO)_5Br$ gave 0.165 g (79 %) **6** as a yellow solid. X-ray quality single crystals were grown by diffusion of a layer of 3 mL hexanes into a CH_2Cl_2 solution (1.5 mL, 0.014 M) or layering 5 mL Et_2O onto a CH_3CN solution (1.4 mL, 0.03 M). Mp: 144 ^oC, dec. Anal. Calcd. (Found) for $C_{21}H_{16}N_6F_3MnO_8S_2$: C, 38.42 (38.46); H, 2.46 (2.61); 12.80 (12.57). IR: ν_{CO} (ATR) = 2045, 1933; tosyl: 1396 (ν_{as}, SO_2), 910 (ν_{S-N}); triflate (s to vs): 1250 (ν_{as}, SO_3), 1159 (ν_{as}, CF_3), 1020 (ν_s, SO_3), 625 (ν_s, SO_3) cm^{-1}. ^1H NMR (CD_3CN, 333 K) δ_H Two species in a 5:1 ratio. Major species: 8.44 (d, J = 3.0 Hz, 1 H,

H_{5cpz}), 8.27 (d, *J* = 2.8 Hz, 2 H, H_{5pz}), 8.24 (s, 1 H, $H_{methine}$), 8.21 (d, J = 2.0 Hz, 2 H, H_{3pz}), 7.80 (d, *J* = 8.4 Hz, 2 H, Ts), 7.44 (d, *J* = 8.4 Hz, 2 H, Ts), 7.06 (d, J = 3.0 Hz, 1 H, H_{4cpz}), 6.55 (dd, *J* = 2.8, 2.0 Hz, 2 H, H_{4pz}), 2.42 (s, 3 H, $TsCH_3$); Minor species: 8.32 (d, *J* = 2.8 Hz, 2 H, H_{5pz}), 8.28 (s, 1 H, $H_{methine}$), 8.15 (d, *J* = 2.0 Hz, 2 H, H_{3pz}), 8.14 (d, *J* = 2.7 Hz, 1 H, H_{5cpz}), 7.72 (d, *J* = 8.5 Hz, 2 H, Ts), 7.42 (d, *J* = 8.5 Hz, 2 H, Ts), 6.74 (dd, *J* = 2.8, 2.0 Hz, 2 H, H_{4pz}), 5.85 (d, *J* = 2.7 Hz, 1 H, H_{4cpz}), 2.43 (s, 3 H, $TsCH_3$) ppm. ^{13}C NMR (CD_3CN) δ_C 221.29 (CO), 214.95 (CO), 149.39, 148.15, 141.19, 136.19, 131.77, 130.99, 129.56, 128.91, 111.55(C_{4cpz}), 109.79 (C_{4pz}), 66.34 ($C_{methine}$), 21.78 (TsMe) ppm. ^{19}F NMR (CD_3CN) δ_F -79.26 (s) ppm. ESI(+) MS *m*/*z* (rel. intensity) [assignment]: 507 (100) $[Mn(CO)_3(^{Ts}L)]^+$, 441 (29) $[Mn(H_2O)(^{Ts}L)]^+$, 423 (3) $[Mn(^{Ts}L)]^+$, 418 (5) $[Mn(CO)_3(^{Na(CH3CN)}L)]^+$, 377 (11) $[Mn(CO)_3(^{Na}L)]^+$, 359 (4) $[Mn(CO)_3(^{Li}L)]^+$. UV-Vis [CH_3CN], λ, nm (ε, $M^{-1}cm^{-1}$): 353 (2430).

[*fac*-$Mn(CO)_3(^{H}L^*)$](OTf), **7**. A mixture of 0.158 g (0.299 mmol) **3a** and 0.0822 g (0.299 mmol) $Mn(CO)_5Br$ gave 0.151 g (85%) **7** as a yellow solid. Mp: 170 ^oC, dec. Anal. Calcd. (Found) for $C_{18}H_{18}N_6F_3MnO_6S$: C, 38.72 (38.59); H, 3.25 (3.62); 15.05 (15.01). IR: ν_{NH} (Nujol/KBr) = 3413; ν_{CO} (ATR) = 2034, 1928; triflate (CH_2Cl_2/KBr, s to vs): 1276 (ν_{as}, SO_3), 1225 (ν_s, CF_3), 1157 (ν_{as}, CF_3), 1028 (ν_s, SO_3), 625 (ν_s, SO_3) cm^{-1}. ^1H NMR (CD_3CN) δ_H 7.89 (br s, 1 H, H_{5cpz}), 6.64 (br s, 1 H, $H_{methine}$), 6.89 (br s, 1 H, H4cpz), 6.12 (br s, 2 H, H4pz*), 2.51 (br s, CH_3), 2.49 (br s, CH_3) ppm; N-H not observed. ^{13}C NMR (CD_3CN) δ_C 221.52 (CO), 215.59 (CO), 156.49, 144.58, 134.96, 109.44 (C_{4pz*}), 106.49 (C_{4cpz}), 60.87 ($C_{methine}$), 15.15 (pz*Me), 11.41(pz*Me) ppm. ^{19}F NMR (CD_3CN) δ_F -79.28 (s) ppm. ESI(+) MS *m*/*z* (rel. intensity) [assignment]: 409

(100) $[Mn(CO)_3(^{H}L^*)]^+$, 366 (11) $[Mn(CH_3CN)(^{H}L^*)]^+$, 353 (21) $[Mn(CO)(^{H}L^*)]^+$, 325 (43) $[Mn(^{H}L^*)]^+$. UV-Vis [CH_3CN], λ, nm (ε, $M^{-1}cm^{-1}$): 347 (2360). Crystals can be obtained by diffusion of a layer of 5 mL Et_2O into a CH_3CN solution (1.4 mL, 0.03 M).

[*fac*-$Mn(CO)_3(^{H}L)$](OTf), **8**. A mixture of 0.200 g (0.425 mmol) **4a** and 0.117 g (0.425 mmol) $Mn(CO)_5Br$ gave 0.187 g (88%) **8** as a yellow solid. Mp: > 210 °C. Anal. Calcd. (Found) for $C_{14}H_{10}N_6F_3MnO_6S$: C, 33.09 (33.31); H, 1.98 (2.03); N, 16.54 (16.44). IR: ν_{NH} (Nujol/KBr) = 3396; ν_{CO} (ATR) = 2043, 1944; triflate (CH_2Cl_2/KBr, s to vs): 1288 (ν_{as}, SO_3), 1221 (ν_s, CF_3), 1145 (ν_{as}, CF_3), 1018 (ν_s, SO_3), 619 (ν_s, SO_3) cm^{-1}. ^1H NMR (CD_3CN, 333 K) δ_H 12.85 (br s, N-H), 8.22 (br s, 2H, H_{3pz}), 8.18 (d, J = 2 Hz, 2 H, H_{5pz}), 8.14 (br s, $H_{methine}$), 7.87 (br s, 1 H, H_{5cpz}), 6.81 (br s, 1 H, H_{4cpz}), 6.49 (br m, 2 H, H_{4pz}) ppm. ^{13}C NMR (CD_3CN, 295 K) δ_C 221.29 (CO), 213.17 (CO), 147.67, 145.38, 135.50, 134.64, 109.13 (C_{4cpz}), 106.87 (C_{4pz}), 66.71 ($C_{methine}$) ppm; CF_3 resonances not observed. ^{19}F NMR (CD_3CN) δ_F -79.24 (s) ppm. ESI(+) MS *m*/*z* (rel. intensity) [assignment]: 353 (96) $[Mn(CO)_3(^{H}L)]^+$, 310 (48) $[Mn(CH_3CN)(^{H}L)]^+$, 287 (11) $[Mn(CO)_3(^{H}L^*)\text{-pz}]^+$, 269 (100) $[Mn(^{H}L)]^+$. UV-Vis [CH_3CN], λ, nm (ε, $M^{-1}cm^{-1}$): 346 (2300). X-ray quality single crystals were grown by diffusion of a layer of 3 mL hexanes into a CH_2Cl_2 solution (1.9 mL, 0.04 M).

$[Fe(^{H}L)_2](OTf)_2$, **9**. *Method A.* A solution of 0.250 g (1.17 mmol) ^{H}L in 10 mL THF was added to a solution of 0.207 g (0.585 mmol) $Fe(OTf)_2$ in THF under argon. A yellow orange solid initially precipitated but changed pink within 30 min. After the resulting pink suspension had been stirred 16 h, the THF was removed by cannula filtration and the

solid was washed with 5 mL Et_2O, then dried in a 140°C oven 2h, to give 0.341 g (75 %) of **9** as a pink powder. Purple single crystals suitable for X-ray diffraction were grown by vapor diffusion of Et_2O into a solution of 15 mg **9** in 1.5 mL MeOH. Characterization data listed below are for crystals or dissolved crystals.

Method B. A solution of 0.205 g (0.434 mmol) **4a** in 10 mL MeOH was added to an argon-purged solution of 0.0275 g (0.217 mmol) $FeCl_2$ in 10 mL H_2O. Upon mixing a purple solution and colorless precipitate formed. After the mixture had been stirred 45 min, the precipitated AgCl was removed by filtration and solvent was removed from the filtrate under vacuum to leave 0.150 g (89 %) **9** as a pink-purple powder.

Method C. A mixture of 0.0500 g (0.106 mmol) **4a** and 0.0030 g (0.053 mmol) Fe^0 powder in 8 mL of CH_3CN was heated at reflux 14 h with vigorous stirring. The resulting pink solution was separated from metallic residue by cannula filtration. The residue was washed with two 2 mL portions of CH_3CN. After removing solvent from the combined CH_3CN soluble fractions by vacuum distillation, a purple solid remained. The solid was dissolved in 1 mL MeOH and the solution was subjected to Et_2O vapor diffusion over 2 d. The mother liquor was decanted from the so-formed red-purple crystals. The crystals were washed with Et_2O and were dried under vacuum 30 min to give 0.028 g (53%) of **9** as red-purple crystals.

Characterization Data for **9**:

Mp. Colorless by 110 °C, did not melt below 250°C. Anal. Calcd. (Found) for $C_{22}H_{20}N_{12}F_6FeO_6S_2$: C, 33.77 (34.05); H, 2.58 (2.71); 21.48 (21.40). μ_{eff} (Evan's, CD_3OD) = 2.0 μ_B. IR: ν_{NH} (Nujol/KBr) = 3140; triflate (CH_2Cl_2/KBr, s to vs): 1265 (ν_{as}, SO_3), 1232 (ν_s, CF_3), 1164 (ν_{as}, CF_3), 1018 (ν_s, SO_3), 623 (ν_s, SO_3) cm^{-1}. UV-vis

[CH_3CN] λ, nm (ε, $M^{-1}cm^{-1}$): 214 (25700), 271 (4650), 315 (sh, 6200), 331 (7300), 520 (100), 1103 (6). ^{1}H NMR (CD_3OD) δ_H 46.21, 30.71, 23.33, 20.19, 11.56, 7.17, -9.96 ppm. ESI(+) MS *m*/*z* (rel. intensity) [assignment]: 633 (1) $[Fe(^HL)_2(OTf)]^+$, 483 (10) $[Fe(^HL)(L)]^+$, 243 (8) $[Fe(^HL)_2]^{2+}$, 209 (9) $[Fe(^HL)(HL\text{-}pz)]^{2+}$, 177 (15) $[Fe(^HL)(CH_3CN)_2]^{2+}$, 156 (11) $[Fe(^HL)(CH_3CN)]^{2+}$, 147 (100) $[^HL\text{-}pz]^+$. If crystals are dried under vacuum 30 min, but not heated at 140°C 2h, then the sample repeatedly analyzed as **9**·MeOH: Anal. Calcd. (Found) for $C_{23}H_{24}N_{12}F_6FeO_7S_2$: C, 33.92 (33.86); H, 2.97 (2.69); 20.64 (20.65).

D. Catalytic Aziridination

To ensure reproducibility, AgOTf and other silver(I) complexes to be used as catalysts were dried at 100°C under vacuum 2h prior to use.

General Procedure. A 0.5 g sample of activated 4 Å molecular sieves and a Teflon-coated magnetic stir bar were added to a Schlenk flask under an argon blanket. The flask was flame-dried under vacuum then was backfilled with argon and allowed to cool to room temperature. Next, the silver catalyst (0.020 mmol), 0.171 g (1.00 mmol) tosylamine, and 0.322 g (1.00 mmol) $PhI(OAc)_2$ were added under an argon blanket. The reaction flask was subjected to three evacuation and argon backfill cycles. Next, 4 mL dry distilled CH_3CN was added by syringe. The reaction flask was placed in an oil bath maintained at 80 °C and allowed to equilibrate for 15 min. Then, 0.57 mL (0.521 g, 5.00 mmol) styrene was added by syringe, at which time the solution changed color to orange or, in some instances, orange-brown. After the reaction mixture had been stirred at 80°C for 16 h, it was filtered through a sintered glass frit. The solid residue was washed with

two 2 mL portions CH_3CN. Next, between 25 to 30 mg of bis(trimethylsilyl)benzene was added to the solvate as a nonvolatile NMR standard and solvent was removed by rotary evaporation to leave a brown-orange oily residue. The residue was separated by column chromatography on silica gel first flushing with hexanes to remove the first fraction (that moves with the solvent front) that contains the NMR standard and iodobenzene. The eluent was then changed to 4:1 (v:v) hexanes : ethyl acetate. The next (second) fraction (R_f = 0.7) is a diastereomeric mixture of 2,4-diphenyl-N-tosyl-pyrrolidine,[55] and the third fraction (R_f ~ 0.4) contains the desired aziridine. The excess H_2NTs and an unidentified brown product remain on the column (but can be eluted with MeOH, if desired). The yields of aziridine given in Table 2.10 are the average of a minimum of three catalytic runs.

E. Crystallography

X-ray intensity data from a colorless needle of **1a**, a colorless plate of **1b**, a colorless prism of **1b**·MeOH, a colorless needle of **2a**, a colorless irregular block of **2b**, a colorless prism of **3a**, a colorless plate of **3b**, a colorless plate of **4a**, a yellow plate of **6**, a yellow prism of **8**, and a pink prism of **9** were each collected at 100.0(1) K with an Oxford Diffraction Ltd. Supernova diffractometer equipped with a 135 mm Atlas CCD detector using Cu(Kα) radiation for the data of **1a, 1b**·1.5CH_3CN**, 1b**·CH_3OH**, 3b, 4b**·acetone·H_2O**, 8**, and **9** while Mo(Kα) radiation was used for the other experiments. Raw data frame integration and Lp corrections were performed with CrysAlis Pro (Oxford Diffraction, Ltd.).[56] Final unit cell parameters were determined by least-squares refinement of 15713, 22719, 14418, 10710, 25334, 19082, 19683, 14285, 18698, 27362,

6891, and 6853 reflections of **1a, 1b**·1.5CH_3CN**, 1b**·MeOH**, 2a, 2b, 3a, 3b, 4a, 4b**·acetone·H_2O**, 6, 8,** and **9**, respectively, with $I > 2\sigma(I)$ for each. Analysis of the data showed negligible crystal decay during collection in each case. Direct methods structure solutions were performed with Olex2.solve[57] while difference Fourier calculations and full-matrix least-squares refinements against F2 were performed with SHELXTL.[58] Numerical absorption corrections based on Gaussian integration over a multifaceted crystal model were applied to the data for each of the complexes except for **9**, which employed a multi-scan empirical absorption correction using spherical harmonics as implemented in the SCALE3 ABSPACK scaling algorithm. All non-hydrogen atoms were refined with anisotropic displacement parameters. Hydrogen atoms bond to nitrogen in structures **3a, 3b, 4a**, **4b**·acetone·H_2O**, 8**, and **9** were located and refined whereas all other hydrogen atoms were placed in geometrically idealized positions and included as riding atoms. The X-ray crystallographic parameters and further details of data collection and structure refinements are given in Tables 2.1-2.3. *Special details:* The crystal of **3b** was a non-regular twin with a 2:1 component ratio where component 2 was rotated by 5.441^o around [0.59 0.68 0.43] in reciprocal space. The structure of **4a** shows polymeric chains along *z* that possess strong quasi-symmetry – a two-fold axes through ions Ag1 and Ag2 results in a higher centrosymmetric pseudo-symmetry of the crystal – P2/c. However, an attempt of refinement in the centrosymmetric space group resulted in a much higher R~13% whereas the refinement as a racemic twin (with a 31:69 component ratio) in space group Pc gave R = 6.8% (Flack parameter, 0.00(16)

Identification code	**1a**	**1b**·1.5CH_3CN	**1b**·CH_3OH	**2a**	**2b**
Empirical formula	$C_{22}H_{24}N_6O_5F_3S_2Ag$	$C_{46}H_{52.5}N_{13.5}O_7F_3S_3Ag$	$C_{44}H_{52}AgF_3N_{12}O_8S_3$	$C_{36}H_{32}N_{12}O_{10}F_6S_4Ag_2$	$C_{35}H_{32}AgF_3N_{12}O_7S_3$
Formula weight	681.46	1167.57	1138.03	1250.72	993.78
Temperature/K	100.00(10)	100.15(10)	100.15(10)	100.00(10)	100(2)
Crystal system	orthorhombic	triclinic	triclinic	triclinic	monoclinic
Space group	Pbca	P-1	P1	P-1	$P2_1/n$
a/Å	14.42803(13)	10.6607(3)	10.1306(3)	9.7107(2)	14.7374(2)
b/Å	14.28519(15)	13.2121(3)	10.6707(3)	10.5529(3)	13.82259(16)
c/Å	26.1584(2)	19.8960(4)	12.7290(4)	12.4514(3)	21.3019(3)
α/°	90.00	71.772(2)	72.330(3)	95.3617(19)	90.00
β/°	90.00	87.8272(18)	87.557(2)	96.2869(18)	108.6404(15)
γ/°	90.00	74.436(2)	72.101(3)	116.694(2)	90.00
Volume/$Å^3$	5391.43(9)	2560.87(10)	1245.68(6)	1118.40(4)	4111.76(10)
Z	8	2	1	1	4
ρ_{calc} g/cm^3	1.679	1.515	1.517	1.857	1.605
μ/mm^{-1}	8.040	4.939	5.066	1.158	0.719
F(000)	2752.0	1202.0	586	624.0	2016
Crystal size/mm^3	0.373 × 0.071 × 0.042	0.349 × 0.123 × 0.042	0.196 × 0.088 × 0.070	0.4725 × 0.1396 × 0.0541	0.449 × 0.272 × 0.217
Radiation	CuKα (λ = 1.54184)	CuKα (λ = 1.54184)	CuKα (λ = 1.54184)	MoKα (λ = 0.71073)	MoKα (λ = 0.71073)
2Θ range for data	9.12 to 148.42	7.32 to 141.36	7.3 to 141.36	7.36 to 58.96	6.64 to 59.4
Index ranges	-17 ≤ h ≤ 18, -13 ≤ k ≤ 17, -31 ≤ l ≤ 32	-13 ≤ h ≤ 13, -15 ≤ k ≤ 16, -23 ≤ l ≤ 24	-12 ≤ h ≤ 12, -13 ≤ k ≤ 13, -15 ≤ l ≤ 15	-13 ≤ h ≤ 13, -14 ≤ k ≤ 14, -17 ≤ l ≤ 17	-20 ≤ h ≤ 15, -18 ≤ k ≤ 18, -29 ≤ l ≤ 26
Reflections collected	32024	47684	23185	25113	47491
Independent reflections	5418 [R_{int} = 0.0334, R_{sigma} = 0.0208]	9706[R_{int} = 0.0420, R_{sigma} = 0.0282]	8602 [R_{int} = 0.0353, R_{sigma} = 0.0382]	5641[R_{int} = 0.0415, R_{sigma} = 0.0395]	10663 [R_{int} = 0.0245, R_{sigma} = 0.0230]
Data/restraints/parameters	5418/0/358	9706/60/748	8602/3/656	5641/0/317	10663/57/625
Goodness-of-fit on F^2	1.041	1.020	1.029	1.044	1.032
Final R indexes [I ≥ 2σ (I)]	R_1 = 0.0262, wR_2 = 0.0647	R_1 = 0.0350, wR_2 = 0.0850	R_1 = 0.0290, wR_2 = 0.0686	R_1 = 0.0346, wR_2 = 0.0733	R_1 = 0.0264, wR_2 = 0.0615
Final R indexes [all data]	R_1 = 0.0314, wR_2 = 0.0678	R_1 = 0.0408, wR_2 = 0.0892	R_1 = 0.0302, wR_2 = 0.0696	R_1 = 0.0472, wR_2 = 0.0792	R_1 = 0.0331, wR_2 = 0.0651
Largest diff. peak/hole / e $Å^{-3}$	0.38/-0.47	0.79/-0.81	0.35/-0.34	0.62/-0.62	0.54/-0.37

[a] $R_1 = \Sigma||F_o| - |F_c||/\Sigma|F_o|$ [b] $wR_2 = [\Sigma w(|F_o| - |F_c|)^2/\Sigma w|F_o|^2]^{1/2}$.

Table 2.1. Crystal data and structure refinement for Ag(^{Ts}L*)](OTf), **1a**, [Ag(^{Ts}L*)$_2$](OTf)·1.5CH_3CN, **1b**·1.5CH_3CN, [Ag(^{Ts}L*)$_2$](OTf)· CH_3OH, **1b**·CH_3OH, [Ag(^{Ts}L)](OTf), **2a**, and [Ag(^{Ts}L)$_2$](OTf), **2b**.

Identification code	**3a**	**3b**	**4a**	**4b**·acetone·H_2O
Empirical formula	$C_{30}H_{36}Ag_2F_6N_{12}O_6S_2$	$C_{29}H_{36}AgF_3N_{12}O_3S$	$C_{11}H_{10}N_6O_3F_3SAg$	$C_{24}H_{28}N_{12}O_5F_3SAg$
Formula weight	1054.57	797.63	471.18	761.51
Temperature/K	100.00(10)	100.0(2)	100.3(5)	100.2(5)
Crystal system	triclinic	triclinic	monoclinic	monoclinic
Space group	P-1	P-1	Pc	C2/c
a/Å	8.29819(12)	10.57500(16)	12.1166(2)	22.1664(3)
b/Å	13.71516(18)	12.58293(16)	10.37159(15)	13.15660(14)
c/Å	17.2294(2)	13.8640(2)	27.0174(5)	21.6700(2)
α/°	96.6432(11)	73.8099(13)	90.00	90.00
β/°	93.8250(11)	72.4934(15)	98.0715(16)	102.5918(11)
γ/°	94.9320(11)	86.1133(11)	90.00	90.00
Volume/Å^3	1934.69(4)	1689.33(4)	3361.59(9)	6167.71(12)
Z	2	2	8	8
ρ_{calc} g/cm^3	1.810	1.568	1.862	1.640
μ/mm^{-1}	1.209	5.953	1.379	6.542
F(000)	1056.0	816	1856.0	3088
Crystal size/mm^3	0.245 × 0.167 × 0.057	0.581 × 0.416 × 0.039	0.31 × 0.228 × 0.051	0.31 × 0.12 × 0.077
Radiation	MoKα (λ = 0.71073)	CuKα (λ =	MoKα (λ =	CuKα (λ =
2Θ range for data	6.6 to 57.18	6.94 to 141.32	6.54 to 57.16	7.86 to 141.5
Index ranges	-11 ≤ h ≤ 11, -18 ≤ k ≤ 17, -22 ≤ l ≤ 22	-12 ≤ h ≤ 12, -15 ≤ k ≤ 15, -16 ≤ l ≤ 16	-15 ≤ h ≤ 16, -13 ≤ k ≤ 13, -35 ≤ l ≤ 36	-21 ≤ h ≤ 27, -16 ≤ k ≤ 15, -26 ≤ l ≤ 26
Reflections collected	42545	31762	38030	29159
Independent reflections	9165 [R_{int} = 0.0385, R_{sigma} = 0.0358]	6391 [R_{int} = 0.1071, R_{sigma} = 0.0538]	15163 [R_{int} = 0.0311, R_{sigma} = 0.0423]	5850 [R_{int} = 0.0921, R_{sigma} = 0.0450]
Data/restraints/parameters	9165/0/531	6391/0/458	15163/272/902	5850/0/434
Goodness-of-fit on F^2	1.081	1.035	1.033	1.045
Final R indexes [I ≥ 2σ (I)]	R_1 = 0.0392, wR_2 = 0.0882	R_1 = 0.0373, wR_2 = 0.0980	R_1 = 0.0677, wR_2 = 0.1849	R_1 = 0.0361, wR_2 = 0.0993
Final R indexes [all data]	R_1 = 0.0540, wR_2 = 0.0965	R_1 = 0.0375, wR_2 = 0.0983	R_1 = 0.0872, wR_2 = 0.2067	R_1 = 0.0366, wR_2 = 0.0999
Largest diff. peak/hole / e Å^{-3}	2.02/-0.60	0.87/-1.09	2.14/-0.76	0.71/-1.24

[a] $R_1 = \Sigma||F_o| - |F_c||/\Sigma|F_o|$ [b] $wR_2 = [\Sigma w(|F_o| - |F_c|)^2/\Sigma w|F_o|^2]^{1/2}$.

Table 2.2. Crystal data and structure refinement for [Ag(^{H}L*)](OTf), **3a** , [Ag(^{H}L*)$_2$](OTf), **3b**, [Ag(^{H}L)](OTf), **4a**, and [Ag(^{H}L)$_2$](OTf) ·acetone·H_2O, **4b**·acetone·H_2O.

Identification code	**6**	**8**	**9**
Empirical formula	$C_{21}H_{16}F_3MnN_6O_8S_2$	$C_{14}H_{10}F_3MnN_6O_6S$	$C_{22}H_{20}N_{12}O_6F_6S_2Fe$
Formula weight	656.46	502.28	782.47
Temperature/K	100.00(10)	100.15(10)	99.9(2)
Crystal system	triclinic	triclinic	monoclinic
Space group	P-1	P-1	P2/c
a/Å	13.0986(3)	8.9770(3)	7.7524(4)
b/Å	14.0933(4)	9.0807(3)	10.2503(5)
c/Å	15.8397(3)	11.9410(3)	18.7519(6)
α/°	98.8216(18)	76.473(2)	90.00
β/°	93.0717(18)	78.445(3)	90.108(4)
γ/°	112.946(2)	81.728(2)	90.00
Volume/Å^3	2640.10(11)	922.40(5)	1490.10(11)
Z	4	2	2
ρ_{calc} g/cm^3	1.652	1.808	1.744
μ/mm^{-1}	0.737	7.630	6.284
F(000)	1328.0	504.0	792.0
Crystal size/mm^3	0.4114 × 0.3781 × 0.0965	0.225 × 0.148 × 0.092	0.194 × 0.107 × 0.066
Radiation	MoKα (λ = 0.71073)	CuKα (λ = 1.54184)	CuKα (λ = 1.54184)
2Θ range for data collection/°	5.6 to 59	7.74 to 141.44	8.62 to 147.98
Index ranges	-18 ≤ h ≤ 17, -19 ≤ k ≤ 19, -20 ≤ l ≤ 21	-10 ≤ h ≤ 10, -11 ≤ k ≤ 11, -14 ≤ l ≤ 14	-9 ≤ h ≤ 9, -9 ≤ k ≤ 12, -23 ≤ l ≤ 22
Reflections collected	58985	6601	14929
Independent reflections	13369 [R_{int} = 0.0322, R_{sigma} = 0.0304]	6601 [R_{int} = 0.0000, R_{sigma} = 0.0119]	3001 [R_{int} = 0.0456, R_{sigma} = 0.0298]
Data/restraints/parameters	13369/0/741	6601/0/281	3001/0/223
Goodness-of-fit on F^2	1.056	1.038	1.064
Final R indexes [I ≥ 2σ (I)]	R_1 = 0.0468, wR_2 = 0.1216	R_1 = 0.0715, wR_2 = 0.1932	R_1 = 0.0481, wR_2 = 0.1279
Final R indexes [all data]	R_1 = 0.0582, wR_2 = 0.1312	R_1 = 0.0736, wR_2 = 0.1968	R_1 = 0.0492, wR_2 = 0.1297
Largest diff. peak/hole / e Å^{-3}	1.06/-0.93	0.76/-0.80	0.84/-1.16

[a] $R_1 = \Sigma||F_o| - |F_c||/\Sigma|F_o|$ [b] $wR_2 = [\Sigma w(|F_o| - |F_c|)^2/\Sigma w|F_o|^2]^{1/2}$.

Table 2.3. Crystal data and structure refinement for [*fac*-Mn(CO)$_3$(^{Ts}L)](OTf), **6**, [*fac*-Mn(CO)$_3$(^{H}L)](OTf), **8**, and [Fe(^{H}L)$_2$](OTf)$_2$, **10**.

Therefore, the non-centrosymmetric model was chosen. The crystal of **4b**·acetone·H_2O was a non-regular twin with a 2:1 component ratio and a 2.38° rotation around [-0.97 0.18 0.16] (reciprocal space). The structure of **9** represents a regular quasi-merohedral (pseudo-orthogonal) twin (rotation 180° around x) with a 61:39 component ratio.

2.3 RESULTS AND DISCUSSION

The new N-confused scorpionate ligands, ^{Ts}L* and ^{H}L*, each with two 3,5-dimethylpyrazolyl groups and either an N-tosyl or N-H moiety, respectively, were prepared in a manner similar to that reported[50] for the parent ligands (with two unsubstituted pyrazol-1-yl groups), as summarized in Scheme 2.1. That is, the $CoCl_2$-catalyzed Peterson rearrangement[59] between the N-tosyl-3- carboxaldehydepyrazole and

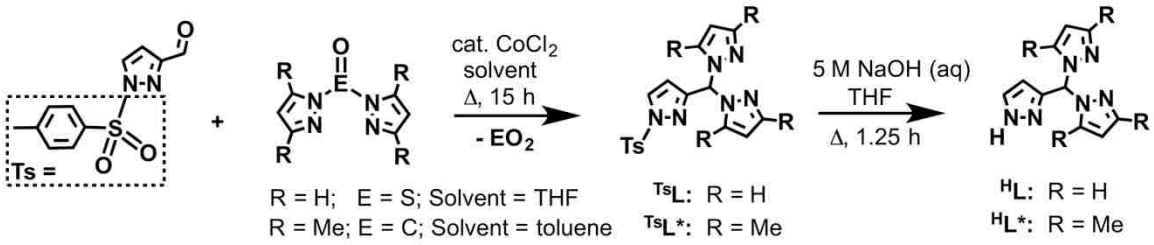

Scheme 2.1. Preparative routes to N-confused scorpionate ligands.

an excess of bis(3,5-dimethylpyrazol-1-yl)carbonyl in toluene gave the desired ligand, ^{Ts}L*, in high yield. Excess O=C(pz*)$_2$ is required for high yield because the reaction with only 1 equivalent consistently gave 63(±2) % yield after purification. The alternative use of O=S(pz*)$_2$ in THF (like used in the synthesis of ^{Ts}L) in place of O=C(pz*)$_2$ in toluene gave lower yields (ca. 60%), presumably due to steric issues which required higher reaction temperature. Deprotection of ^{Ts}L* by aqueous base proceeded

smoothly to give ^{H}L* but required longer reaction time than the deprotection of ^{Ts}L, (45 min versus 10 min) as indicated by TLC monitoring. In contrast to the parent deprotected ligand, ^{H}L, that required extensive extraction, ^{H}L* is much less soluble in water, so extraction and subsequent purification were uncomplicated. The N-tosyl ligands give characteristic IR bands near 1380 and 1180 cm^{-1} for antisymmetric and symmetric S-O stretches, respectively. The IR spectra for ^{H}L and ^{H}L* show weak bands for N-H stretches at 3430, and 3450 cm^{-1}, respectively.[60] For these latter ligands in CD_3CN, the ^{1}H NMR resonance for the N-H group appears as a broad singlet downfield near 11.3 ppm, a region similar to that found for other pyrazoles.

With the four ligands in hand, their 1:1 and 2:1 L:Ag(OTf) complexes were prepared in high yields by mixing THF solutions of the appropriate ligand (1 or 2 molar equivalents), one equivalent of the silver salt, and collecting the precipitate by filtration. All of the silver complexes are light stable colorless solids. Most are air stable but **3b** and **4b** readily absorb adventitious water, so care must be taken if one wants anhydrous complexes. Each complex is soluble in many Lewis basic organic solvents, with the exception of Et_2O (insoluble) or THF (slightly soluble), and has modest solubility in $CHCl_3$ or CH_2Cl_2. Vapor diffusion of Et_2O into either CH_3CN or CH_3OH solutions of the various complexes afforded X-ray quality single crystals in most cases except for $[Ag(^{H}L)_2](OTf)$, **4b**, for which evaporation from acetone:water mixtures gave the mixed solvate.

A. Solid State

As illustrated in Figure 2.2, **1a** features a four coordinate silver as a result of binding to the tridentate, κ^3*N*-, ligand and a triflate oxygen. Noteworthy, is that while the

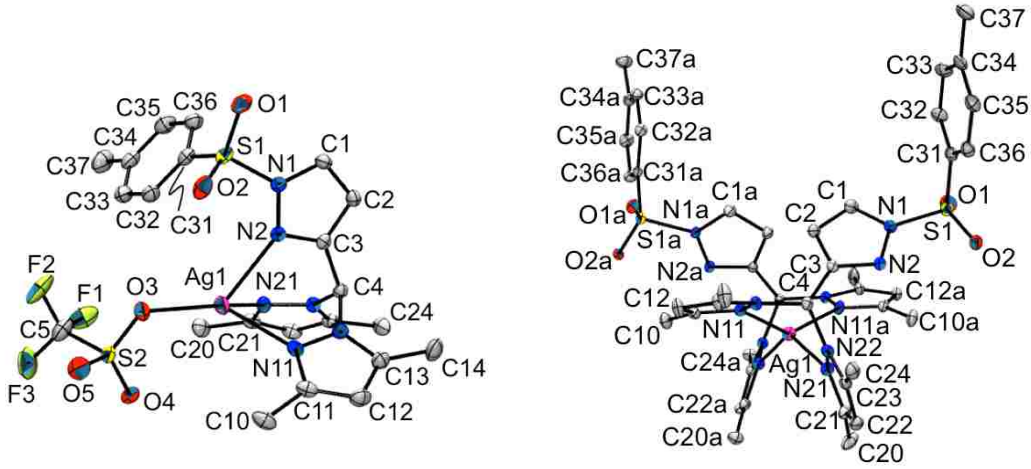

Figure 2.2. Structures of [Ag(^{Ts}L*)](OTf), **1a** (left), and of the cation in [Ag(^{Ts}L*)$_2$](OTf)·1.5CH$_3$CN, **1b**·1.5CH$_3$CN (right) with hydrogens removed for clarity.

Ag-N bond of tosylpyrazolyl is nearly 0.1 Å longer than those of the other pyrazolyls (Table 2.4), the average Ag-N$_{pz}$ distance of 2.37 Å is firmly in the 2.3 - 2.4 Å range for other four-coordinate silver pyrazolyl complexes[61] including {[κ^3-(3-tBupz)$_3$CH]Ag}(OTf) (2.38 Avg)[41a] and {[κ^3-(3-Phpz)$_3$CH]Ag(CH$_3$CN)})BF$_4$ (2.36 Å).[41b] The three pyrazolyls are also disparately twisted as quantified by either the AgN-CC$_{meth}$ torsion angle of the 'confused' pyrazolyl (4^o, here) or the AgN-NC$_{methine}$ torsion angles of the 'normal' pyrazolyls (6, and 18^o, for rings containing N11 and N21, respectively). The Ag-O distance (Ag-O3 2.224(2) Å) is among the shortest known for silver triflate complexes; it is shorter than relatives such as{Ag[C$_6$H$_5$CH$_2$OCH$_2$Cpz$_3$]}OTf (2.343 Å),[62] [Ag(4-MeO-2,6-pz*$_2$-triazine)]OTf (2.292 Å),[44] Ag[HC(pz^{3tBu})$_3$]}OTf (2.264 Å),[41a] and is in between the distances found in {Ag$_2$(μ_2-4,13-dibenzyl-4,13-diaza-18-crown-6)}(OTf)$_2$ (2.252(3), 2.215(3) Å).[64] In

Bond Distances (Å)			
1a		**1b**·1.5CH_3CN	
Ag1-N2	2.4273(17)	Ag1-N21	2.318(2)
Ag1-N11	2.3391(18)	Ag1-N11	2.339(2)
Ag1-N21	2.3434(18)	Ag1-N11a	2.315(2)
Ag1-O3	2.2235(16)	Ag1-N21a	2.332(2)
Bond Angles (°)			
O3-Ag1-N2	127.21(6)	N11-Ag1-N21	79.42(7)
O3-Ag1-N11	131.19(6)	N11-Ag1-N11a	143.21(7)
O3-Ag1-N21	138.16(7)	N11-Ag1-N21a	111.72(8)
N2-Ag1-N11	80.90(6)	N21-Ag1-N11a	119.94(7)
N2-Ag1-N21	77.27(6)	N21-Ag1-N21a	130.92(7)
N11-Ag1-N21	80.61(6)	N11a-Ag1-N21a	80.30(7)

Table 2.4. Selected bond distances (Å) and angles (°) in [Ag(^{Ts}L*)](OTf), **1a** and Ag(^{Ts}L*)$_2$](OTf)·CH_3CN, **1b**·1.5CH_3CN.

1b·1.5CH_3CN or **1b**·CH_3OH, silver is four-coordinate due to binding to the pz* groups with an average Ag-N distance of 2.33 Å in each solvate; the confused tosyl pyrazolyl is not bound to silver in either case (Fig. 2.2, right). The silver centers in both solvates of **1b** adopt nearly identical distorted sawhorse geometries with τ_δ parameters[65] of 0.56 (closer to distorted tetrahedral, τ_δ = 0.63, than a sawhorse, τ_δ = 0.45). Interestingly, the SO groups of the tosyl unit (rather than of the triflate) are hydrogen bonded to the methine hydrogens of neighboring cations to help organize the three-dimensional extended structure.

Complex **2a** exists as a dimer with inversion symmetry as a result of two ligands that sandwich two closely spaced silver centers (Ag···Ag separation 3.0588(4) Å), Figure 2.3. The μ-κ^1,κ^1- ligands act in a manner where the two 'normal' pyrazolyls on each ligand bind to two different silver centers with Ag-N11 of 2.182(2) Å and Ag-N21 of 2.232(2) Å. The average Ag-N distance of 2.207 Å is much longer than the 2.10-2.14 Å range found for two coordinate silver bound to pyrazolyls[61] and is at the lower end of the 2.2-2.3 Å range for three-coordinate silver. The tosyl-protected 'confused' pyrazolyl is highly twisted ('pz twist' = 76°) such that the very long Ag-N2 of distance 2.672 Å is probably better described as an Ag-π secondary interaction rather than a σ- bonding interaction. As a comparison, the 'pz twists' of the 'normal' pyrazolyls (here, with shorter Ag-N bonds are 19° for the ring with N21 and 55° for the ring with N11. Instead, the coordination sphere about each silver center is completed by an interaction with an oxygen atom of a triflate anion, Ag···O32.586(2) Å, that is within the ca. 2.07–2.75 Å range (average Ag···O distance 2.48±0.13 Å) found for other complexes of silver triflate.[66]

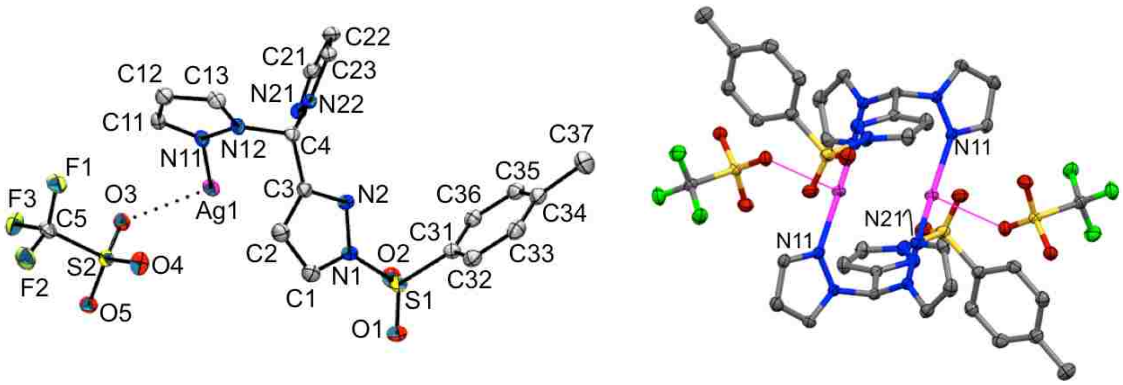

Figure 2.3. Views of the structure of [Ag(^{Ts}L)](OTf), **2a**, with hydrogens removed for clarity. Left: Asymmetric unit with atom labeling. Right: Dimeric unit.

The complex $[Ag(^{Ts}L)_2](OTf)$, **2b**, similar to **1b**, has a four-coordinate metal center as a result of binding to the 'normal' pyrazolyls of two ligands (average Ag-N_{pz} 2.31 Å) instead of the 'confused' tosyl pyrazolyls. In the case of **2b**, the silver center is distorted tetrahedral with $\tau_\delta = 0.71$, a value that shows the metal to be more ideally tetrahedral than that in either solvate of **1b**. The low steric profile of the normal pyrazolyls in **2b** allows contact between the triflate anion and the acidic methine hydrogen that, in turn, plays an integral role in the assembly of the three-dimensional supramolecular structure.

Figure 2.4 shows the dimeric structure of $[Ag(^{H}L^*)](OTf)$, **3a**, while Table 2.5 gives selected interatomic distances and angles. As opposed to dimeric **2a** that had μ-κ^1,κ^1-ligands with an unbound 'confused' pyrazolyl, the dimer in **3a** is constructed of two bridging, μ-κ^1,κ^1- ligands sandwiching two silvers. Here, the two dimethylpyrazolyl rings chelate one silver center while the confused pyrazolyl binds the second proximal silver to give a short Ag···Ag separation 2.8271(4) Å (compare to twice the van der Waals radii of silver = 3.44 Å).

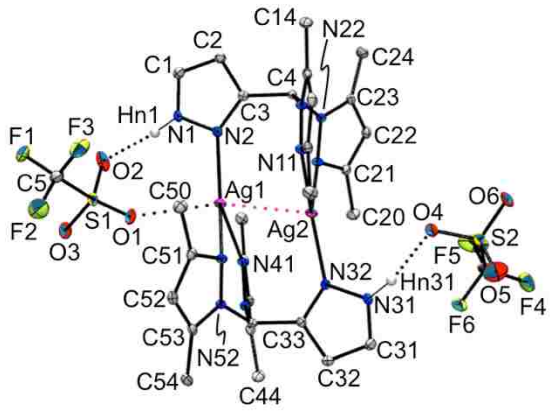

Figure 2.4. Structure of $[Ag(^{H}L^*)](OTf)$, **3a**, with partial atom labeling. Most of the hydrogen atoms are omitted for clarity.

The ligands are arranged such that each silver is bound to one 'confused' pz nitrogen and to two pz* nitrogens. Two triflate anions are also affixed to the dimer by short hydrogen bonds involving the confused pyrazolyl's N-H groups (N1H1n···O2 1.935 Å; N31H31n···O4 1.897 Å). The triflate anion with O1 also forms a long bond with silver (Ag1-O1 = 2.724 Å) but the other triflate is not bound; the closest contact to Ag2 is with O4 at 3.632 Å. The disparity in anion binding sites is responsible for the longer average Ag-N distance involving Ag 1 (2.278 Å) than that for Ag2 (2.254 Å), distances that straddle the borderline demarcating three- or four-coordinate silver pyrazolyl complexes.

Bond Distance			
Ag1-O1	2.724(3)	Ag2-N32	2.173 (2)
Ag1-N2	2.196(2)	Ag2-N11	2.316(3)
Ag1-N41	2.307(3)	Ag2-N21	2.274(3)
Ag1-N51	2.331(2)	Ag1···Ag2	2.8271(4)
Bond Angles			
O1-Ag1-N2	96.08(9)	N11-Ag2-N21	82.83(9)
O1-Ag1-N41	100.53(8)	N11-Ag2-N32	136.66(9)
O1-Ag1-N51	85.39(9)	N21-Ag2-N32	138.86(9)
N2-Ag1-N41	135.99(9)		
N2-Ag1-N51	141.51(9)		
N41-Ag1-N51	80.63(9)		

Table 2.5. Selected interatomic distances (Å) and angles (^{o}) in [Ag(^{H}L*)](OTf), **3a**.

Views of the structure of **3b** are found in Figure 2.5 while bond distances and angles are tabulated in Table 2.6. Complex **3b** adopts a distorted tetrahedral AgN_4 kernel ($\tau_\delta = 0.56$) as a result of binding only pz* nitrogen atoms (avg Ag-N. 2.34 Å). The two 'confused' pyrazolyl arms are involved in different hydrogen bonding interactions.

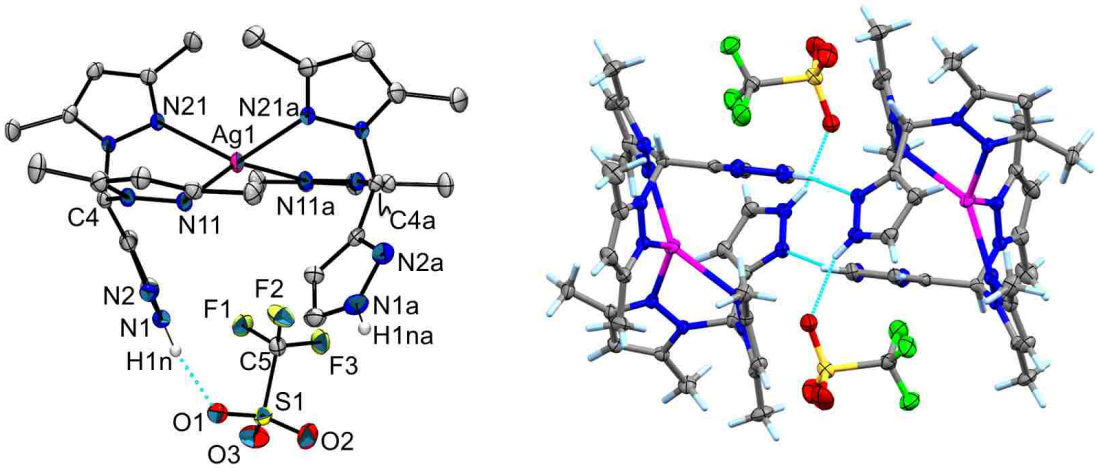

Figure 2.5. Views of **3b** with most of the hydrogen atoms removed for clarity and with partial atom labeling. Left: Asymmetric unit. Right: Hydrogen-bonded (cyan lines) dimer.

First, one 'confused' pyrazolyl acts as a hydrogen bond donor to a triflate oxygen acceptor (N1H1n···O1, 2.088 Å, 153°). The second 'confused' pyrazolyl acts as a hydrogen bond donor to a nitrogen atom (N1aH1na···N2', 1.984 Å, 168°) of the triflate-bonded confused pyrazolyl ring on a neighboring complex to form a H-bonded dimer (Figure 2.5, right). Such an interaction positions the triflate ion in close van der Waals contact with the pz* ring hydrogen and one of the methyl hydrogen atoms on the neighboring complex (C12H12···O2, 2.793 Å, 140°; C10H10b···O1, 2.788 Å, 143°) further securing the dimer.

Bond Distance	
Ag1-N11	2.3839(19)
Ag1-N21	2.3067(19)
Ag1-N11a	2.3218(19)
Ag1-N21a	2.3387(19)

Bond Angles	
N11-Ag1-N21	83.42(6)
N11-Ag1-N11a	143.43(7)

N21-Ag1-N21a	125.16(6)
N11a-Ag1-N21	126.25(6)
N21-Ag1-N11a	100.52(6)
N11a-Ag1-N21a	80.31(7)

Table 2.6. Selected interatomic distances (Å) and angles (°) in $[Ag(^{H}L^{*})_2](OTf)$, **3b**.

Complex **4a** crystallizes as a 1D coordination polymer that propagates along the *c*-axis as a result of bridging ligands that bind neighboring silver centers, Figure 2.6. The ligands show a μ-κ^1,κ^1- binding mode, where the chelating portion of the ligand is composed of the 'normal' pyrazolyls while the unidentate portion involves the 'confused' pyrazolyl. These ligands are arranged such as to alternate AgN_4 and AgN_2 kernels (i.e., one silver is bound to the chelating portions of two ligands while the other silver is bound to two κ^1*N*- 'confused' pyrazolyl nitrogens). Selected bond distances and angles are given in Table 2.7. The average Ag-N distances of 2.299 Å and 2.321 Å for Ag3 and Ag4 respectively are clearly indicative of four-coordinate silver whereas those of 2.153 Å for Ag1 and 2.162 Å for Ag2 are between the ranges usually found for two- and three-coordinate silver pyrazolyls. Inspection of the coordination sphere about Ag reveals two long Ag-O interactions on each silver center; one that is below the 2.75 Å Ag-O bonding limit (Ag1-O7 2.734 Å and Ag2-O4 2.719 Å) and one that is just above the limit (Ag1-O10 2.756 Å, Ag2-O1 2.767 Å). If the longer Ag-O distance were considered a secondary contact then Ag1 and Ag2 would both be three-coordinate.

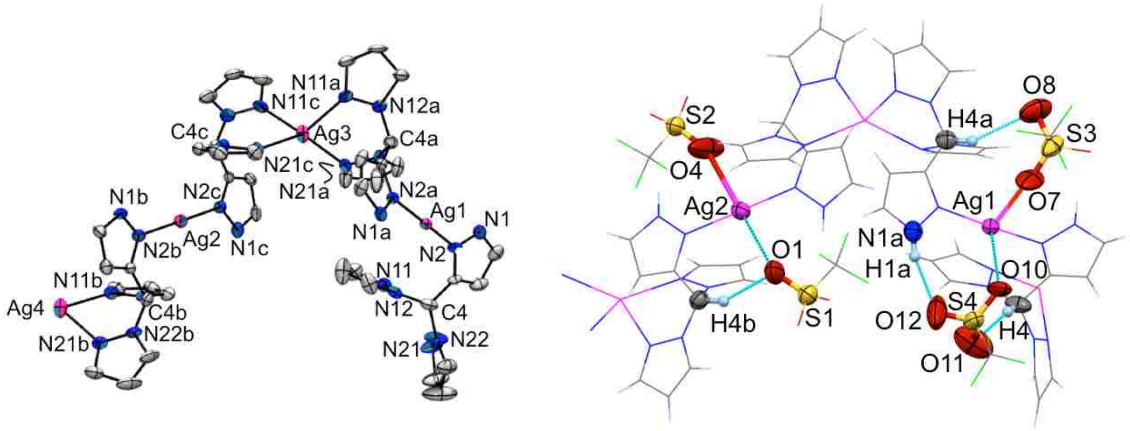

Figure 2.6. A portion of the structure of [Ag(^{H}L)](OTf), **4a**, with partial atom labeling. Most hydrogen atoms are removed for clarity and thermal ellipsoids are shown at 30% probability.

Bond Distances (Å)			
Ag1-N2	2.158(8)	Ag2-N2b	2.176(8)
Ag1-N2a	2.150(8)	Ag2-N2c	2.148(8)
Ag3-N11a	2.322(10)	Ag4-N11	2.266(10)
Ag3-N11c	2.339(10)	Ag4-N21	2.365(12)
Ag3-N21a	2.275(9)	Ag4-N11b	2.282(8)
Ag3-N21c	2.258(9)	Ag4-N21b	2.370(9)
Bond Angles (°)			
N2-Ag1-N2a	175.3(3)	N2b-Ag2-N2c	179.0(3)
N11a-Ag3-N11c	113.0(3)	N11-Ag4-N11b	138.3(4)
N11a-Ag3-N21a	86.6(4)	N11-Ag4-N21	84.5(4)
N11a-Ag3-N21c	121.7(4)	N11-Ag4-N21b	124.3(4)
N11c-Ag3-N21a	123.7(4)	N11b-Ag4-N21	120.2(4)
N11c-Ag3-N21c	83.9(4)	N11b-Ag4-N21b	81.7(3)
N21a-Ag3-N21c	130.9(3)	N21-Ag4-N21b	109.1(4)

Table 2.7. Selected bond distances (Å) and angles (°) in [Ag(^{H}L)](OTf), **4a.**

Then, since Ag1 sits 0.084 Å out of the O7N2N2a plane, the four atoms form an acute triclinic pyramid (based on a 3% folded T) while the planar Ag2N2bN2cO4 unit represents a slightly distorted T-shape (or, more specifically, a γ-constricted near-closed Y).[48] The 'confused' pyrazolyl's N-H group serves as a hydrogen bond donor to triflate oxygen atoms to further secure triflate ions to the chain and between chains to assemble the supramolecular structure.

Views of the structure of **4b**·acetone·H_2O shown in Figure 2.7. Selected bond distances and angles are provided in Table 2.8. The crystal contains two independent cations in the asymmetric unit.

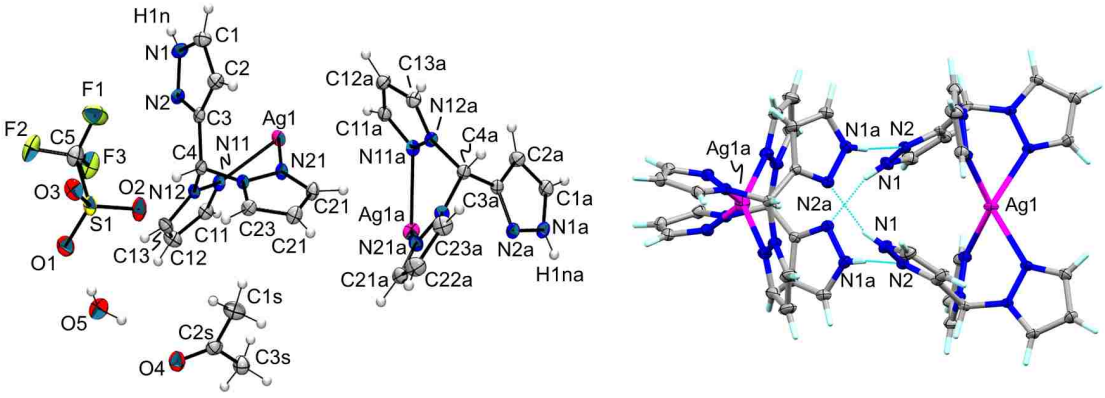

Figure 2.7. Structure of **4b**·acetone·H_2O. Left: Asymmetric unit with atom labeling. Right: Hydrogen bonded (cyan lines) dimer of cations.

As with the other [AgL_2](OTf) complexes, the metal center in each of the independent cations is tetracoordinate as a result of binding the two nitrogen atoms of the 'normal' pyrazolyls on each ligand. One silver center, Ag1, is distorted tetrahedral (τ_δ = 0.63) with an average Ag-N distance of 2.35 while the other silver, Ag1a, is closer to a

distorted sawhorse ($\tau_\delta = 0.59$) with an average Ag-N distance of 2.36 Å, distances characteristic of four-coordinate silver. The 'confused' pyrazolyls are not bound to silver in either cation, rather they participate in hydrogen bonding interactions with analogous rings on a neighboring cation to give a C_2-symmetric dimer (right of Figure 2.7).

Bond Distance			
Ag1-N11	2.293(2)	Ag1a-N11a	2.465 (2)
Ag1-N12	2.412(2)	Ag1a-N12a	2.248 (2)
Bond Angles			
N11-Ag1-N11'	137.56(9)	N11a-Ag1a-N11a'	125.30(8)
N11-Ag1-N21	80.69(6)	N11a-Ag1a-N21a	85.14(6)
N11-Ag1-N21'	121.15(7)	N11a-Ag1a-N21a'	113.16(6)
N11'-Ag1-N21'	80.69(6)	N11a'-Ag1a-N21a'	85.14(6)
N11'-Ag1-N21	121.15(7)	N11a'-Ag1a-N21a	113.16(6)
N21-Ag1-N21'	121.17(8)	N21a-Ag1a-N21a'	140.77(10)

Table 2.8. Selected bond distances (Å) and angles (^{o}) for **4b**·acetone·H_2O.

The triflate ions are hydrogen bonded to the methine hydrogens on one cation with Ag1 (C4-H4···O2: 2.215 Å, 162^o) while the acetone solvate weakly hydrogen bonded to the methine hydrogens on the other cation (C4aH4a···O4 2.411 Å, 147^o). The solvate water serves as a hydrogen donor to a triflate oxygen on one dimer (O5H5b···O1 2.001 Å, 171^o) and the acetone oxygen (O5H5a···O4 2.133 Å, 152^o) of an adjacent dimer to help organize the three-dimensional supramolecular structure.

B. Solution

The nature of the silver(I) complexes in acetonitrile solution were investigated intensively by spectroscopic methods (1D and diffusion NMR, IR) and by ESI(+) mass spectrometry since this solvent is used for catalytic reactions described later. The collective data indicate that all have dynamic solution structures where the static solid-state structures are not retained. Instead, it is likely that the complexes are dissociated and that multiple species exist in solution as a result of two or more of the following equilibria (Equations 1-4).

$$^{1}/_{n}\,[Ag(L)]_n(OTf)_n \leftrightarrows [Ag(L)](OTf) \quad (1)$$

$$[Ag(L)](OTf) \leftrightarrows Ag(OTf) + L \quad (2)$$

$$[Ag(L)](OTf) + L \leftrightarrows [Ag(L)_2](OTf) \quad (3)$$

$$[Ag(L)](OTf) \leftrightarrows \tfrac{1}{2}\,[Ag(L)_2](OTf) + \tfrac{1}{2}\,Ag(OTf) \quad (4)$$

The equilibria are demonstrated by multiple different observations. First, crystallizations of analytically pure samples of [AgL](OTf) in either CH_3CN or CH_3OH produce mixtures of crystals. Vapor diffusion of dilute solutions (0.005 M) give mainly the mono-ligated silver along with small amounts of the di-ligated $[AgL_2](OTf)$, whereas more concentrated solutions (0.02 to 0.04 M) begin to favor the bis-ligated species over the mono-, as determined by careful analysis of crystal morphologies and subsequent unit cell measurements. Interestingly, crystallizations of $[AgL_2](OTf)$ did not produce noticeable amounts of [AgL](OTf); the equilibrium constant for Eq. 3 must be relatively large in all cases. It is conjectured that the lower solubility of [Ag(L)](OTf) versus $[AgL_2](OTf)$ in THF (and the limiting L) allows the isolation of the former by

precipitation. Upon dissolution of the pure [Ag(L)](OTf) in more polar solvents, equilibrium mixtures are obtained.

Secondly, NMR titrations of the ligands, L, with silver triflate (reverse of Eq 2 and forward Eq. 3) or of $[AgL_2](OTf)$ with AgOTf (reverse of Eq 4) in CD_3CN only gave one set of resonances (with different chemical shifts) regardless of the stoichiometry or the temperature within the solvent's liquid range, showing that these four species are in rapid equilibrium.

Thirdly, the diffusion oriented spectroscopy (DOSY) NMR experiments of various metal complexes of the new ligands were acquired at room temperature to provide further insight into their molecularity. Table 2.9 collects the diffusion constants, the hydrodynamic radii (calculated by using the Stokes Einstein relation), and the calculated radii from both X-ray diffraction studies and molecular modeling of the various ionic compounds. The data indicate that the complexes are most likely monomeric in CD_3CN at room temperature as the hydrodynamic radii of all silver(I) complexes are similar to one another (even those with dimeric and polymeric solid state structures) and to those of the kinetically inert monomeric tricarbonylmanganese(I) complexes of the same ligands described later.

Next, the number and chemical shifts of the resonances in the NMR spectrum of each compound indicates that the complexes have dynamic solution structures that are different than their solid-state structures. The complexation of the ligands to cationic metal centers is characterized by a downfield shift in the 'normal' pyrazolyl ring hydrogen H4 resonances, with respect to those in the free ligands. In every silver complex (and for the inert $[Mn(CO)_3]^+$ complexes, described later), the 'normal' pincer

pyrazolyls have downfield-shifted H4 resonances and, hence, are silver-bound. For the 'confused' pyrazolyl ring in each complex, the chemical shift of the resonance for the H5-ring hydrogen (next to the ring nitrogen's tosyl or N-H group) indicates whether or not this heterocycle is metal-bound. In the spectra of each **3a**, **3b**, **4a**, and **4b** (with ^{H}L or ^{H}L*), the H5- resonance is shifted downfield indicating that the 'confused' ring is bound whereas in the remaining cases (with ^{Ts}L or ^{Ts}L*) the chemical shift of this resonance matches that for the free ligand, so the confused ring is likely not bound.

Compound	*D* (x10^{-10} m^2/s)	r_{DOSY} (Å)	r_{Xray} (Å)	r_{model} (Å)	r_{model} (bonding)
$NBu_4(OTf)$	9.3(1)	5.7(2)	6.0[ref]	5.9	
[Ag(^{Ts}L*)](OTf), **1a**	7.0(9)	7.7(9)	6.5	6.8	κ^3, monomer
				7.5	κ^3, + CH_3CN
				8.7	κ^2, + CH_3CN
				11.3	κ^2,κ^1N-dimer
[Ag(^{Ts}L*)$_2$](OTf), **1b**	7.3(1)	7.2(1)	8.5	10.0	tetrahedral
[Ag(^{Ts}L)](OTf), **2a**	7.6(9)	7.8(8)		7.0	κ^3, monomer
				8.5	κ^2, + CH_3CN
				8.9	Ag(^{Ts}L)$_2$, tet.
				11.3	κ^2,κ^1N-dimer
			10.7	11.7	κ^1,κ^1N-dimer
[Ag(^{H}L*)](OTf), **3a**	9.0(9)	6.1(9)		6.0	κ^3,monomer
				6.3	κ^3, + CH_3CN
				7.4	Ag(^{H}L*)$_2$, tet.
			7.82	8.0	κ^2,κ^1N-dimer
[Ag(^{H}L)](OTf), **4a**	7.9(4)	6.9(5)		5.33	κ^3,monomer
				7.45	κ^3, + CH_3CN
			7.10[frg]	6.7	Ag(^{H}L)$_2$, tet.
				8.2	κ^2,κ^1N-dimer

$[Mn(CO)_3(^{Ts}L^*)](OTf)$, **5**	7.4(1)	7.1(2)		6.4	κ^3,monomer
$[Mn(CO)_3(^{H}L)](OTf)$, **8**	8.3(1)	6.4(2)	5.8	6.1	κ^3,monomer
Longest dist					

Table 2.9. Summary of data from ^{1}H NMR DOSY experiments and radii from longest interatomic distances in reference structures or models.

Thus, the ligands in **1a**, **2a**, **3b**, and **4b**, have different denticities in solution versus the solid state. It is reasonable that the latter two complexes may be six-coordinate in solution given the sandwich structures of $[Ag(\kappa^3\text{-}Tpm^x)_2]^{+}$[41] and the low energy barrier calculated for κ^2/κ^3-$[Ag(Tpm)]^+$ interconversions.[68] Considering the DOSY experiments, $[Ag(CH_3CN)_n(\kappa^2\text{-}^{Ts}L^x)]^+$ (n = 1-2) would be possible for **1a** and **2a** (and by analogy for **3a**). These formulations do not include a silver-bound triflate because the spectroscopic data for each complex indicates a free (unbound) triflate anion in solution. That is, the ^{19}F NMR spectrum of each in CD_3CN shows only one resonance at -79.3 ppm that matches that for NBu_4OTf. It is also noteworthy that the solution IR spectra of each has one set of strong bands in the 1280 to 1025 cm^{-1} range for symmetric and asymmetric SO_3 and CF_3 stretching modes that are characteristic of an unbound triflate anion.[69] Thus, the solution structures of **1a-4a** with unbound triflates are different than the solid that showed silver-bound triflates. Although the triflate ion is not bound to silver in acetonitrile solution, there is evidence for ion pairing most cases, except **4a** and **4b**, from anomalous upfield shifts in certain hydrogen resonances, as seen with other metal complexes.[70] That is, for complexes **1a**, **1b**, **3a**, and **3b** with pz* groups, the resonance for the acidic methine, for H_4 of the 'confused' pyrazolyl ring, and that for one set of methyl pz* hydrogens (closest to the methine) are unexpectedly shifted *upfield*

from those in the spectrum of the free ligand. Given the different groups on the confused pyrazolyls and the propensity for triflate to be located near the methine positions of silver poly(pyrazolyl)methane complexes in the solid state,[66] it is likely these hydrogens are shielded by proximity to a nearby triflate ion.

It is noted that the ^{1}H NMR spectrum of a concentrated mixture of NBu_4OTf and each charge neutral ligand is a simple sum of the individual spectra of the pure components. Since the presence of the triflate does not affect the chemical shift of the charge-neutral ligands, ion pairing is essential for the observation of the unusual upfield shifts (charge-assisted weak hydrogen bonding). In **2a** and **2b**, only the resonance for H_4 of the confused ring is significantly shifted upfield. It is unclear why upfield shifts were not observed in the spectrum of either **4a** or **4b** of similar concentration to the other complexes. The simplicity of the ^{1}H NMR spectrum of **2a** also indicates the static solid-state structure is not retained in solution. If it was retained, then two sets of resonances would be expected since the tosyl pyrazolyl arm points toward one of the 'normal' pyrazolyls (see right of Fig 2.3) and would differentiate these heterocycles. Fast free rotation about the $C_{methine}$-C bond of the 'confused' pyrazolyl could explain equivalence at room temperature. Again, it was not possible to slow the dynamic behavior in the liquid range of CH_3CN. Given the results of the NMR titrations and the DOSY experiment described above, it is most likely that rather than retaining a dimeric solid-state structure, complex **2a** likely dissociates to a monomeric structure (Eq 1), which then participates multiple fast dynamic equilibria according to Eqs. 2-4. Similarly, the spectrum of **4a** is simpler than expected based on the polymeric solid-state structure. There was only one set of sharp resonances for the 'normal' pyrazolyls when two sets

would be expected if the solid structure of **4a** remained intact and static in solution (those pyrazolyls in Figure 2.6 with N11 would be different than those with N21 by proximity to the confused pyrazolyl or to the pseudo-C_2 axis that passes through Ag3). In this case direct dissociation (by breaking the Ag-N bonds on two-coordinate Ag) to give **4b** and AgOTf directly (Equation 4) or dissociation to monomeric $[Ag(CH_3CN)_n(\kappa^3\text{-}^{H}L)]^+$ are reasonable possibilities.

Finally, ESI(+) mass spectral data of discrete complexes and coordination polymers of *inert* metal ions are generally accepted to be representative of solution structures.[71] Electrospray ionization is soft enough that labile complexes, supramolecular species, and other non-covalent interactions can also be measured by this technique.[72] The results described here and the extensive studies by the Reger group on the structures and ESI(+) mass spectra of silver(I) poly(pyrazolyl)methane complexes demonstrate the existence of multiple solution species.[41,73,74] For instance, the ESI(+) mass spectrum of a solution of analytically pure **1a**, which had a monomeric $Ag(^{Ts}L^*)(OTf)$ solid structure consists of a parent 100% relative abundance peak at m/*z* 329 for a ligand fragment ($^{Ts}L^*$ - pz*), a lower intensity peak (with 87% relative abundance) at m/*z* 957 for $[Ag(^{Ts}L^*)_2]^+$, and a still lower intensity peak (41% rel. abund.) at m/*z* 531 for the expected parent ion, $[Ag(^{Ts}L^*)]^+$. Clearly the $[Ag(^{Ts}L^*)_2]^+$ species could arise from a redistribution reaction (Eq 4) or from self-assembly of fragments whether already present in solution (Eq 3) or, less likely, that are generated during ionizing conditions. Unfortunately, peaks for $[Ag(CH_3CN)_n]^+$ (n = 3, 4) species were not observed in the spectral window (m/*z* 200 to 1400). The mass spectrum of **1b** differs from **1a** only by intensities of peaks. Given the NMR titration data and the fact that mixtures of crystals are obtained from crystallization

of analytically pure **1a** in CH_3CN (the solvent also used in ESI(+) experiments), we favor the notion that the ESI(+) data are more likely representative of solution structures partitioned via Eqs (2-4) rather than being representative of species generated during or after ionization. The mass spectral data for the remaining silver complexes agrees with many (but not all) trends outlined previously by the Reger group on related systems. Thus, the spectrum of **2a** and **3a**, which exhibit dimeric solid state structures, feature weak intensity (< 30% rel. abund.) peaks corresponding to $[Ag_2L_2(OTf)]^+$ and, for **3a**, to $[Ag_2(^HL^*)_2OTf - pz^*]^+$ and $[Ag_2(^HL^*)(L^* = \text{deprotonated ligand})]^+$. The highest intensity peaks in each spectrum were for $[AgL_2]^+$ (100% rel. Abund.) and $[AgL]^+$ (> 70% rel. abund.). The lack of half integer m/*z* peaks establishes the monomeric nature of the $[AgL]^+$ species. The mass spectrum of **4a**, which has a polymeric solid state structure, displayed very weak intensity (< 5% rel. abund.) peaks for $[Ag_3(^HL)_3(OTf)_2]^+$, $[Ag_3(^HL)_2(OTf)_2]^+$, $[Ag_3(^HL)_2(OTf)(Cl)]^+$, $[Ag_3(^HL)(L)(OTf)]^+$, and $[Ag_3(L)_2]^+$, where L is deprotonated ligand and Cl^- comes from the trace ions normally present in the mass spectrometer. There is also a series of higher intensity (between 5 to 40 % rel. abundance) peaks for dimeric monocationic species such as $[Ag_2(^HL)_2(OTf)]^+$ as well as di-silver fragments $[Ag_2L(X = Cl, OTf)]^+$. These peaks are rather unexpected since Reger had indicated that in cases of silver(I) poly(pyrazolyl)methanes with polymeric solid state structures, peaks for dimeric units were notably absent.[73a,c] It may be possible that crystallization under different conditions may lead to a yet-to-be-discovered dimeric form of **4a**. As with the other three $[AgL]^+$ complexes, the most abundant peaks in the mass spectrum of **4a**, were for $[Ag(^HL)_2]^+$ (95% rel. abund.) and $[Ag(^HL)]^+$ (100% rel. abund.). The origin of the relatively high abundance of monomeric monocations and decreasing

abundance of higher order monocations is most likely the result of the overall equilibrium constant of Eqs 1-4. It is also noteworthy that the mass spectrum of **2b**, **3b**, or **4b**, are devoid of peaks for disilver or other higher order fragments. So the equilibrium constant for Eq 3 must again be relatively large.

C. Reactivity

The synthetic utility of the silver complexes as ligand delivery agents was demonstrated first via preparation of tricarbonylmanganese(I) complexes. The reactions between any of **1a**, **2a**, **3a** or **4a** and $Mn(CO)_5Br$ in refluxing CH_3CN for 3 h gave high yields of $[Mn(CO)_3(^{Ts}L^*)](OTf)$, **5**, $[Mn(CO)_3(^{Ts}L)](OTf)$, **6**, $[Mn(CO)_3(^{H}L^*)](OTf)$, **7**, or $[Mn(CO)_3(^{H}L)](OTf)$, **8**, as appropriate. Complexes **5**-**8** are slightly light sensitive yellow solids that are soluble in many organic solvents except hydrocarbons and Et_2O. Solutions of the complexes are noticeably more light-sensitive than the solids. So, solution characterization data were obtained only for freshly prepared solutions and with precautions to exclude light, vide infra. The IR spectra of **5**-**8**, Table 2.10, each give characteristic bands for the *fac*-$Mn(CO)_3$ moiety. That is, one sharp, higher-energy and one broad, lower-energy band are found in the spectra of the solids. In CH_2Cl_2 solutions, the broad band is split to give three resolved bands in the cases of **5**-**7**; the local symmetry about Mn in **8** is probably high enough (C_{3v}) that the nominal *E* stretching mode is not split. The larger band broadening in the solids compared to solution likely does not allow resolution of any splitting in the broader band in this state. Also, as usual, the (weighted) average energies of CO stretching frequencies in the solid are 10 to 20 cm^{-1} lower than that in solution.

Ligand	ν_{CO} (cm^{-1})	reference
$HC(pz^*)_3$	2044, 1949; Wt. avg.: 1981	JOMC 2000
$HC(pz)_3$	2051, 1956; Wt. avg.: 1988	Reger
$^{Ts}L^*$	2046, 1957, 1942; Avg.; 1982	This work
^{Ts}L	2052, 1965, 1952; Avg.; 1990	This work
$^{H}L^*$	2046, 1955, 1943; Avg.; 1981	This work
^{H}L	2050, 1955; Wt. avg.: 1987	This work

Table 2.10. IR spectral data (CH_2Cl_2, KBr) for $[(Ligand)Mn(CO)_3](O_3SCF_3)$ complexes.

In either medium, complexes **5** and **7**, with 3,5-dimethylpyrazolyl donors, exhibit lower average CO-stretching frequencies than **6** and **8** with unsubstituted pyrazolyls because the ligands in the former are stronger donors than the latter and increase the backbonding capabilities of the Mn(I) center to the carbonyl. These findings are in agreement with those previously reported for $[(HC(pz^{R3,R5})_3)Mn(CO)_3](O_3SCF_3)$ (R = H, Me) (in CH_2Cl_2).[44] In the current complexes, the replacement of a tosyl group with a hydrogen has a marginal impact on the average CO stretching frequencies in CH_2Cl_2 solution.

The *fac*-coordination mode was verified by X-ray diffraction for **6** and **8**, Figure 2.8 and Table 2.11. In each, the ligands exhibit κ^3*N*- coordination to the metal center. In **6**, there are two independent cations in the asymmetric unit. In each, the Mn-N bond involving the tosyl pyrazolyl (average 2.140 Å) is significantly longer that the other two Mn-N bonds (averaging 2.057 Å). The overall average Mn-N distance of 2.085 Å is longer than 2.07 Å found in $[HC(3\text{-}iPrpz)_3)Mn(CO)_3](O_3SCF_3)$[44] and 2.040 Å in

$[(PhCpz_2py)Mn(CO)_3](O_3SCF_3)$.[75] The disparity in Mn-N distances also leads to a dichotomy in Mn-C distances where the Mn-C bond *trans*- to the tosyl pyrazolyl (average 1.805 Å) is shorter than the other two Mn-C bonds (average 1.821 Å).

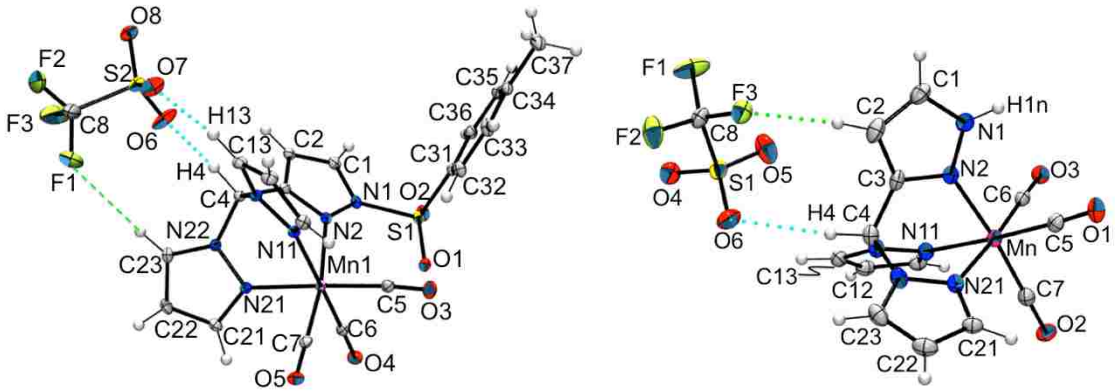

Figure 2.8. Left: Structure of one of two symmetry independent units in the crystal of **6**. Right: Structure of **8** with partial atom labeling.

Bond Distance (Å)					
	6			**8**	
Mn1-N2	2.1354(18)	Mn1a-N2a	2.149(2)	Mn1-N2	2.041(2)
Mn1-N11	2.0501(18)	Mn1a-N11a	2.0494(19)	Mn1-N11	2.058(2)
Mn1-N21	2.0652(18)	Mn1a-N21a	2.0613(19)	Mn1-N21	2.059(2)
Mn1-C5	1.822(2)	Mn1a-C5a	1.805(3)	Mn1-C5	1.807(3)
Mn1-C6	1.824(2)	Mn1a-C6a	1.826(2)	Mn1-C6	1.815(3)
Mn1-C7	1.803(2)	Mn1a-C7a	1.812(2)	Mn1-C7	1.812(3)

Bond Angles (°)					
N2-Mn1-N11	82.18(7)	N2a-Mn1a-N11a	81.89(7)	N2-Mn1-N11	84.08(10)
N2-Mn1-N21	83.47(7)	N2a-Mn1a-N21a	83.78(7)	N2-Mn1-N21	82.55(10)
N11-Mn1-N21	86.84(7)	N11a-Mn1a-N21a	86.07(7)	N11-Mn1-N21	84.86(9)

C5-Mn1-C6	89.98(10)	C5a-Mn1a-C6a	89.64(12)	C5-Mn1-C6	87.91(12)
C5-Mn1-C7	87.31(10)	C5a-Mn1a-C7a	85.08(11)	C5-Mn1-C7	91.49(13)
C6-Mn1-C7	90.17(10)	C6a-Mn1a-C7a	90.01(11)	C6-Mn1-C7	89.54(12)
C5-Mn1-N2	99.57(8)	C5a-Mn1a-N2a	172.24(10)	C5-Mn1-N2	92.52(11)
C5-Mn1-N11	91.86(8)	C5a-Mn1a-N11a	92.45(10)	C5-Mn1-N11	176.59(11)
C5-Mn1-N21	176.51(9)	C5a-Mn1a-N21a	90.55(10)	C5-Mn1-N21	94.71(11)
C6-Mn1-N2	95.95(8)	C6a-Mn1a-N2a	95.80(9)	C6-Mn1-N2	94.33(11)
C6-Mn1-N11	177.57(9)	C6a-Mn1a-N11a	176.88(9)	C6-Mn1-N11	92.35(11)
C6-Mn1-N21	91.42(9)	C6a-Mn1a-N21a	91.59(9)	C6-Mn1-N21	176.01(10)
C7-Mn1-N2	170.76(8)	C7a-Mn1a-N2a	100.41(9)	C7-Mn1-N2	174.52(11)
C7-Mn1-N11	90.17(10)	C7a-Mn1a-N11a	92.48(9)	C7-Mn1-N11	91.91(12)
C7-Mn1-N21	89.48(9)	C7a-Mn1a-N21a	175.34(10)	C7-Mn1-N21	93.40(11)

Table 2.11. Selected bond distances (Å) and angles (^{o}) in $[Mn(CO)_3(^{Ts}L)](OTf)$, **6**, and $[Mn(CO)_3(^{H}L)](OTf)$, **8.**

There is no significant discrepancy in C-O bond distances which average 1.141(3) Å. In **8**, the average Mn-N bond distance of 2.052 Å is shorter than that found for **6** and the distances are more uniform, as might be expected after considering the relative steric demands of the 'confused' pyrazolyls in each complex. The triflate anions in **6** and **8** are affixed to the cations via short CH···O (cyan dotted lines, Fig 2.8) and CH···F (green dotted lines Figure 2.8) interactions and in the case of **8**, NH···O weak hydrogen bonding (not shown) and serve to organize the three-dimensional supramolecular structure.

In CD_3CN solution, the NMR spectra for each **7** and **8** were in accord with expectations of complexes with κ^3*N*- ligands coordinated to the *fac*-$Mn(CO)_3$ fragment. At room temperature the resonances for ligand hydrogens are broadened slightly by the quadrupolar ^{55}Mn nucleus ($I = {}^5/_2$, 100%) but sharpen on heating. All resonances are

shifted downfield from those found in the free ligand. The spectrum of each **5** and **6** in CD_2Cl_2 or acetone-d_6 are in accord with expectations but those in CD_3CN are more complicated than expected as two sets of resonances in a 5:1 ratio are observed. The major resonances agree with expectations for a κ^3*N*- ligated species where all resonances for ligand hydrogen nuclei are shifted downfield compared to those of the free ligand. The minor resonances have all downfield shifted resonances except for those of the confused pyrazolyl, which are shifted upfield from those in the free ligand. It is likely that the minor species has a dissociated tosylpyrazolyl group and solvent bound to the metal instead. Due to the different relaxation times of the ^{13}C nuclei versus ^{1}H, the ^{13}C NMR spectra of **7** and **8** are not broadened. The resonances for the carbonyl carbons are observed at room temperature near 221 and 215 ppm, consistent with the chemical shifts reported for the tricarbonylmanganese(I) complexes of tris(pyrazolyl)methane derivatives.[44] The electronic absorption spectrum of each **5**-**8** consists of a medium intensity ($\varepsilon \sim 2500\ M^{-1}cm^{-1}$) low energy MLCT band ($d_{Mn}$-$\pi^*_{CO}$) with a λ_{max} near 360 nm that trails into the violet which is responsible for the yellow color of the complexes. The intraligand transitions are found at higher energy. The light sensitivity of the complexes is likely due to the known photo-activated CO releasing properties of $[(HCpz_3)Mn(CO)_3]^+$ and related complexes (thereby removing the chromophore).[76] This property is outside of the scope of the current work, so was not investigated further.

The use of silver complexes as stoichiometric ligand delivery agents was also demonstrated in preparation of the iron(II) complex, $[Fe(^{H}L)_2](OTf)_2$, **9** by two routes. First, the metathesis reaction between a methanol solution of **4a** (2 eq.) and an aqueous solution of $FeCl_2$ (1 eq.) gave a high yield of pure **9** after simply removing AgCl by

filtration and solvent under vacuum. Alternatively, a lower yield of **9** was obtained by the redox reaction between two equivalents of **4a** and iron metal in CH_3CN. The lower yield of this latter route was a result of both incomplete reaction and difficulties associated with separating **9** from residual **4a** by fractional crystallization. It is noted that the direct reaction between the two equivalents of ligand and commercial $Fe(OTf)_2$ to give **9** gave a lower yield than the metathetical route because of issues with solubility of reagents, as well as the difficulties separating the product from the unidentified yellow intermediate. Thus, the alternative routes to **9** proved useful when unexpected difficulties occurred in the direct reaction and could be useful in the future with certain cases where a metal triflate salt is not readily available or is more expensive than a metal halide or elemental metal (cobalt, for instance).

Vapor diffusion of Et_2O into a MeOH solution of **9** gave crystals suitable for X-ray diffraction. The structure of **9** obtained at 100 K is given in Figure 2.9. The complex crystallizes as a *cis*- isomer in the P2/c space group where iron resides on a C_2 crystallographic axis that bisects the 'confused' pyrazolyls through iron giving only three inequivalent Fe-N bonds in the FeN_6 kernel. The Fe1-N2 bond of the 'confused'

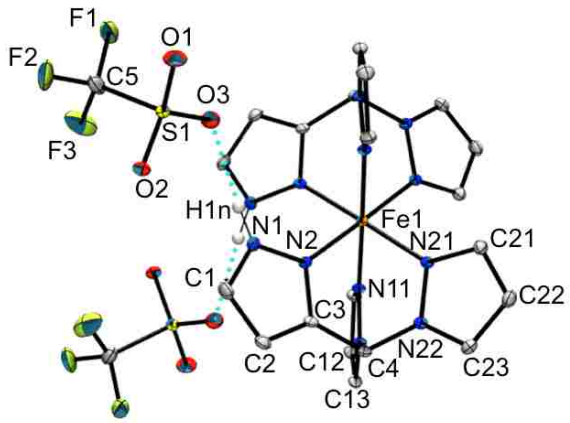

Figure 2.9. Structure of $[Fe(^{H}L)_2](OTf)_2$, **9**, with most hydrogen atoms removed for clarity.

pyrazolyl of 1.941(3) Å is shorter than the similar bonds of the other two pyrazolyls (Fe1-N11 1.978(3) Å, Fe1-N21 1.983(3) Å) and all are consistent with low spin rather than high spin iron(II). The triflate counterions are affixed to the dication via charge-assisted weak hydrogen bonding with the confused pyrazolyl (N1H1n···O3 2.025 Å, 176°). Further weak CH···O interactions between triflate oxygen and acidic (methine and pyrazolyl) hydrogen atoms of neighboring dications serve to organize the three-dimensional supramolecular structure.

Although complex **9** is pink, a color characteristic of LS Fe^{II}, it is slightly paramagnetic at room temperature. Crystalline or powder samples reversibly change between pink and colorless on cycling between heating to 150 °C and then cooling back to room temperature. This behavior is similar to $[Fe(^{H}L)_2](BF_4)_2$, **10**, a compound that showed a gradual (S=2 to S=0) spin transition with $T_{1/2}$ near 360 K (beginning at ca. 275 K and is only 80 % complete at 400 K).[50] The solid state magnetic behavior of **9** (Figure 2.10) shows a spin transition $T_{1/2}$ near 365 K but the SCO is more abrupt than in that in **10**. The SCO in **9** begins at ca. 330 K and reaches ca. 95% completion at 400 K. Weak charge-assisted hydrogen bonding organizes the solid-state structure in each **9** and **10**. Clearly the abruptness of the $\chi_M T$ versus T curve in the 300-400 K range indicates that NH···O and CH···O interactions in **9** are stronger that the NH···F and CH···F interactions in **10**, as might be expected. It is also noteworthy that solutions of **9** are also slightly paramagnetic despite being pink. The solution magnetic moment of 2.0 μ_B (Evan's method) for **9** in CD_3OD at 295 K is indicative of a significant fraction of high

spin iron(II) and is similar to the solid state magnetic moment at 295 K. The electronic absorption spectrum shows characteristic bands for d-d transitions and MLCT bands of LS spin iron and a very weak feature in the near-IR (ca. 9000 cm^{-1}) for the weak d-d transition for HS Fe(II).

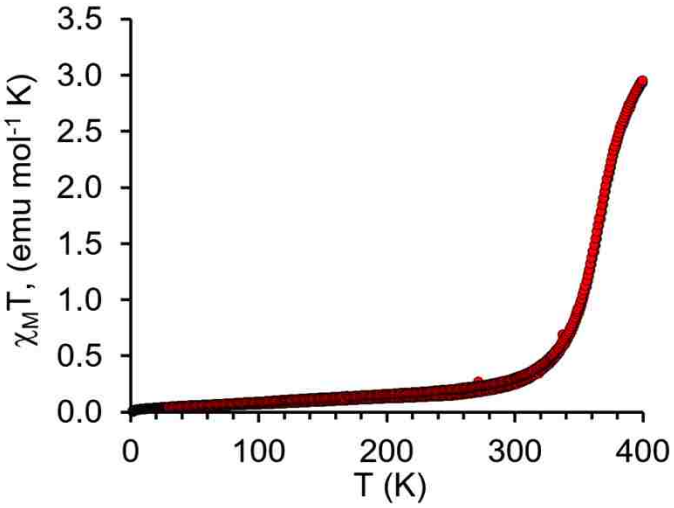

Figure 2.10. Temperature dependence of $\chi_M T$ for **9** from SQUID magnetometry.

D. Nitrene Transfer Catalysis

The ability for the new silver complexes to catalyze nitrene transfer at a 2 mol% loading was probed by reaction between styrene, N-tosylamine, and a commercial hypervalent iodine reagent, $PhI(OAc)_2$, in CH_3CN. Table 2.12 summarizes the results of these initial investigations. Surprisingly, the best performing catalyst of those tested was **1b** followed by **1a** ≈ **2a,** and then **3a**. The other new silver complexes performed similarly to control experiments that show activated molecular sieves, alone, have some activity under these conditions (16 h at 80°C). It is noted that the aziridination reactions did not proceed either at room temperature, in CH_2Cl_2, or when using pre-formed

PhI=NTs (as in other silver- catalyzed aziridination reactions). For those complexes that successfully catalyzed the aziridination of styrene, the use of strictly anhydrous silver triflate (for in-situ reactions) or oven-dried samples of preformed complexes was crucial for ensuring both reproducibility and maximum activity (as reported in other cases). Interestingly, in the reactions where catalysis was successful, a small amount (1-2%) of a statistical diastereomeric mixture of 2,4- diphenyl-N-tosylpyrrolidine (B, see Table 2.12) was also identified (by ^{1}H NMR and ESI(+) MS).

This side product, B, is a result of [3+2] cycloaddition between styrene and 2-phenyl-*N*-tosylaziridine (A). While this particular transformation has been reported to be catalyzed by manganese(III) tetraphenylporphyrin[55], to our knowledge, it has never previously been effected by a silver(I) complex. However, [3+2] cycloadditions between aziridines and either alkynes , aldehydes, or napthols are known to be catalyzed (or promoted) by $AgSbF_6$ or AgOTf. Control reactions on the NMR scale showed that heating a mixture of styrene and aziridine did not lead to any productive transformation (other than the slow formation of polystyrene). The addition of **1a** also did not give pyrrolidine (B). The presence of the by-product requires the oxidant and heating at 80^{o}C. The higher activity of **1b** versus **1a** is rather surprising, considering the relative reactivity of the remaining complexes that favor complexes with 1:1 rather than 2:1 ligand:metal ratios. It can be speculated that both $[AgL]^{+}$ and $[AgL_2]^{+}$ may catalyze the reactions (and both exist in solution via Eqs 1-4) but the larger steric requirements of ^{Ts}L* decreases the likelihood for the di-ligated species to adopt a six-coordinate (and, presumably catalytically inactive) silver center in solution. Future experimental and computational efforts will be directed toward determining the mechanism of catalysis and if altering

ligand sterics or electronics can give silver C-scorpionate catalysts that are more competitive with the $AgTp^x$ or other silver catalysts for aziridination reactions.

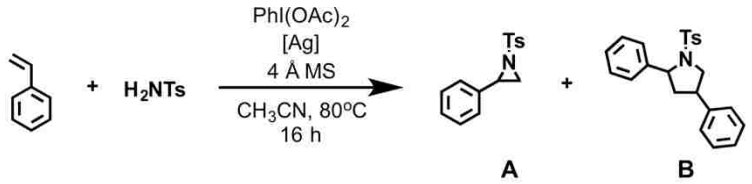

Entry	[Ag]	(NMR yield A)	(% yield A)[a]	(% yield B)[a]	TON[b]
1	none	3 (2)	0	0	0
2	AgOTf	3 (2)	0	0	0
3	**1a**	17 (6)	18 (5)	2.2 (0.1)	10
4	**1b**	34 (4)	27 (3)	2 (1)	15
5	**1b**[c]	27 (3)			
6	**2a**	16 (8)	10 (2)	2.1 (0.5)	11
7	**2a**[d]	trace			
8	**2b**	6 (2)	8 (2)	0	4
9	**3a**	15 (3)	12 (4)	1 (0.2)	7
10	**3b**	6 (1)			
11	**4a**	8 (2)	2	0	1
12	**4b**[c]	6 (1)			

Conditions: 5 mmol styrene, 1 mmol $PhI(OAc)_2$, 1 mmol H_2NTs, 0.02 mmol [Ag], 0.5 g 4 Å MS, 4 mL CH_3CN, 16 h, 80°C.

Notes: [a]isolated yields based on H_2NTs, average of three runs (average deviation in parentheses); [b]TON = mmol (A+B, isolated)/mmol [Ag]; [c]in situ; [d]Room temperature. 16 h.

Table 2.12. Summary of results from nitrene transfer reactions.

2.4 CONCLUSIONS

Two new N-confused C-scorpionate ligands with 3,5-dimethylpyrazolyl 'pincers' and either an *N*-tosyl (^{Ts}L*) or an N-H (^{H}L*) 'stinger' have been prepared in high yield. Together with the previously known, less bulky derivatives, a complete set of four N-confused scorpionate ligands with a wide range of steric profiles is now available for coordination chemistry studies. It was possible to structurally characterize the complete set of eight silver complexes that had both 1:1 and 2:1 L:Ag ratios. In the solid state, the 2:1 complexes had tetracoordinate silver by binding only the pincers; the confused scorpionate stinger was not bound. This is a remarkable finding in light of the structures $[Ag(Tpm^{x})_2]^+$ complexes that showed only hexacoordinate sandwich structures and of theoretical studies that showed a barrierless transition from κ^2-Tpm to κ^3-Tpm complexation. Steric bulk and electronic effects may both favor the formation of tetracoordiate complexes of the N-tosylated ligands, while stabilization through hydrogen bonding interactions in the solid state may play an integral role for $[Ag(^{H}L^*)_2]^+$ and $[Ag(^{H}L)_2]^+$. In 1:1 complexes, the bulkiest derivative, ^{Ts}L*, gave a monomeric species, the least bulky derivative, ^{H}L, gave a polymeric species and the other two ligands of medium steric profiles gave dimeric complexes in the solid state. The ^{1}H NMR, DOSY NMR, and ESI(+) mass spectral studies indicate that the solid state structures are not preserved in solution. Rather, all have dynamic solution behavior and are involved in multiple rapid equilibria. The labile nature of silver(I) complexes is expected and allows for their use of silver(I) complexes as effective ligand delivery agents. This property was demonstrated by the preparation of tricarbonylmanganese(I) complexes and of $[Fe(^{H}L)_2](OTf)_2$, a complex with spin crossover properties. Also, for the first time, the

use of silver(I) C-scorpionates as nitrene transfer catalysts has been demonstrated by the aziridination of styrene in CH_3CN using H_2NTs and $PhI(OAc)_2$ as an oxidant. The variation in ligand sterics differentiated the catalytic activity of the new silver complexes with the bulkiest derivative, $[Ag(^{Ts}L^*)_2](OTf)$, outperforming $[Ag(^{Ts}L^*)](OTf)$ and all others tested. This letter observation is relatively surprising since with other silver complexes of N-donor ligands, catalytic activity toward aziridination is generally favored when silver adopts lower coordination numbers. Regardless, the current complexes require more demanding conditions and exhibit overall lower activity for catalyzing aziridination of styrene compared to those reported for $AgTp^x$ complexes. This may be related to the more complex solution behavior including the possibility for coordination to ions. Perhaps with proper substituents on the pyrazolyls (further increasing steric bulk) or the use of other less-coordinating ions, challenges such as the formation of byproduct, B, the requirement of elevated reaction temperature, and relatively low turnover numbers can be overcome to make these current catalysts more competitive with others for intermolecular aziridination.

Chapter 3

IRON(II) TRIFLUOROMETHANESULFONATE COMPLEXES ON AN N-CONFUSED C-SCORPIONATE, ^{H}L*

3.1 INTRODUCTION

There is great interest in iron(II) complexes that undergo reversible spin state switching between the paramagnetic high spin (HS) $^5T_{2g}$ and the diamagnetic low spin (LS) $^1A_{1g}$ electronic states upon application or relief of external perturbations for various technological applications.[7,80] This electronic spin crossover (SCO) can be provoked via changes in temperature,[1,81,82,83] pressure,[84,85] guest absorption,[86-90] application of electric[91] or magnetic[92] fields, or with light irradiation.[93-97] Since the SCO properties are detectable even down to the single molecule level, their potential in molecular electronics has driven reinvigorated scrutiny of these complexes.[98-103] With some exceptions,[104-112] a vast majority of iron(II) complexes that exhibit SCO behavior possess octahedral FeN_6 cores.[113-118] Of those, iron(II) hetero- and homo-scorpionates[20a,b] such as those shown in Chart 3.1 represent important subsets because they provide structurally and magnetically diverse SCO compounds with convenient syntheses that allows for either systematic studies or means to tailor material properties.

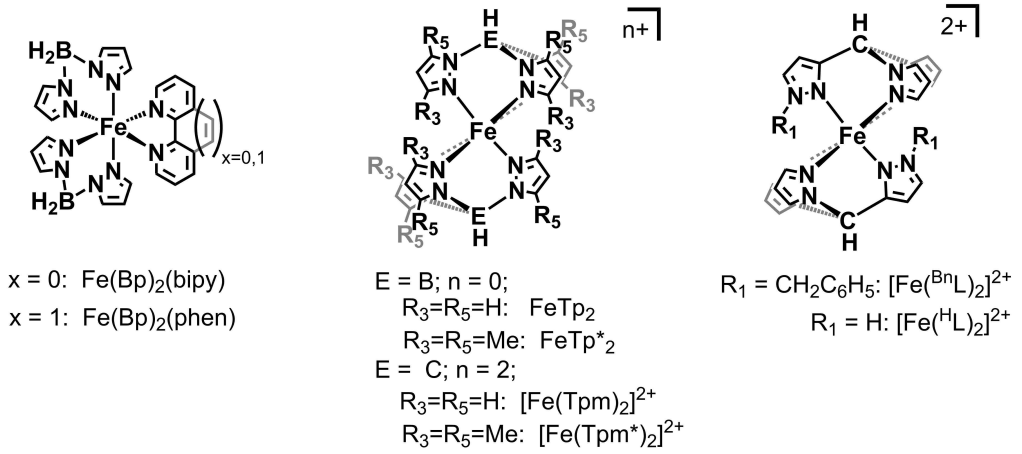

Chart 3.1. Representative iron(II) scorpionate complexes that exhibit electronic spin crossover.

In 1967, Trofimenko first reported the preparation of metal complexes of the heteroscorpionates Bp ($[H_2B(pz)_2]^-$, pz = pyrazol-1-yl), Bp* ($[H_2B(pz^*)_2]^-$, pz* = 3,5-dimethylpyrazol-1-yl), and of the homoscorpionates, Tp, ($[HB(pz)_3]^-$) and Tp*, ($[HB(pz^*)_3]^-$).[119,120] The large temperature dependence of the magnetic moment and electronic spectra of $FeTp_2$ in CH_2Cl_2 and $CHCl_3$ solution due to spin crossover was noted by Trofimenko's group later that year.[10,121] Subsequent work verified SCO behavior of both $FeTp_2$ and $FeTp^*_2$ (Chart 3.1, center) in the solid state by structural, spectroscopic, and magnetic studies.[122,123] In fact, SCO behavior was found to be a prevalent feature for most other $FeTp^x_2$ compounds with different substitution patterns on the scorpionate backbone in the solid state, as long as the average pyrazolyl ring twisting (measured by the FeN-NB torsion angle) was less than 11^o.[16] Interestingly a recent re-examination of the magnetic properties of $FeTp_2$ showed that the SCO behavior of the first heating and cooling cycle differed from its subsequent cycles due to an irreversible phase from a meta-stable tetragonal crystal system (formed during purification by sublimation) to the thermodynamically stable monoclinic crystal system.[12] This unique

magnetic behavior was exploited in the development of a read-only memory device.[124] Similar anomalous magnetic behavior has been found for $FeTp^*_2$.[125,126] Here, the bulk material from crystallization has an abrupt spin transition with $T_{1/2}$ (temperature with 50% HS) near 195 K[122] but thin film samples that were deposited by vacuum sublimation show hysteresis with $T_{1/2}\downarrow$ near 150 K and $T_{1/2}\uparrow$ near 190 K, depending on the size of crystallites. The authors suspected that a crystallographic phase change was responsible for the unique magnetic behavior.[125] Indeed, a phase change from a metastable tetragonal phase to the thermodynamically stable triclinic phase was found later by another group.[126]

A seminal report by the Real group described the preparation of adducts of Trofimenko's $FeBp_2$ with 2,2-bipyridyl or 1,10-phenanthroline, left of Chart 3.1.[127] The former had an abrupt SCO with $T_{1/2}$ near 160 K while the latter shows a 4 K hysteresis with $T_{1/2}\downarrow$ 162 K and $T_{1/2}\uparrow$ 166 K. The pressure and light induced spin state switching was demonstrated later,[128,129] results which have inspired numerous investigations into other properties of these systems and on variants with modified poly(pyridyl)backbones.[130-139]

The SCO behavior of $[Fe(Tpm^x)_2]^{2+}$ complexes (Chart 3.1, bottom center) mirrors the borate counterparts in many ways, but the ionic nature of the former and the greater propensity of inclusion of solvate molecules can greatly impact the properties. For instance, the parent complex $[Fe(Tpm)_2](BF_4)_2$ is LS at room temperature and undergoes a somewhat abrupt SCO to HS near 400 K, very much like the first heating cycle of sublimed $FeTp_2$.[15a] On the other hand, $[Fe(Tpm^*)_2](I)_2 \cdot xCH_2Cl_2$ showed disparate SCO; the solvent-free complex has a 15 K hysteresis centered around 203 K but the tetra-

solvate is high spin at all temperatures.[13,140] Alterations of the ligand provide means to tune SCO behavior. For $[Fe(Tpm^*)_2](BF_4)_2$, an abrupt SCO at 203 K is found but the transition was only 50% complete due to a crystallographic phase change in which the low temperature phase gives two uniques sites (even in Co and Ni complexes). One site had a dication with very twisted rings (pz twist 24°) and was high spin while the other site had lesser twisting (3°) and was low-spin; again pyrazolyl ring twisting can prevent SCO behavior.[14,15b,140,141] The Lavrenova group has comprehensively explored the effects of replacing ions and solvent in $[Fe(Tpm^x)_2]$ $(Y)_2 \cdot x$ solvate complexes and has found drastically different SCO behaviors.[142-145] The mixed scorpionate complex, $[Fe(Tpm)(Tpm^*)](BF_4)_2$ crystallizes as two polymorphs where the triclinic form with closer intermolecular interactions gave lower $T_{1/2}$ (228 K) and more abrupt SCO than the monoclinic form ($T_{1/2}$ ca 310 K).[17] The Goodman group has demonstrated that substitution at the 5-position (R_5, center Chart 3.1) or replacing the methine proton with methyl groups serve to close the bite angles to favor LS iron(II).[18,146] Similar observations have been made in a borate analogues.[147,148]

Recently, our group described the large scale preparation of several N-confused tris(pyrazolyl)methane derivatives where one of the three pyrazolyls is attached to the methine carbon by a carbon rather than by the more typical nitrogen atom of the heterocycle (right, Chart 3.1).[50] Such a bonding pattern allows for unprecedented control of steric and electronic properties of the scorpionate ligand through the use of simple nitrogen protection and deprotection reaction sequences. The initially studied iron(II) complexes of the parent ligand, ^{H}L, with an N-H group on the confused pyrazolyl and no substituents on the normal pyrazolyls, showed gradual spin crossover with $T_{1/2}$

(temperature with 50% HS) above room temperature. Replacement of the normal pyrazolyls with 3,5-dimethylpyrazolyls in the ligand, $^{H}L^{*}$, was expected to lower $T_{1/2}$ due to unfavorable steric interactions between methyls that would favor the HS state. While this expectation was met, unusual magnetic behavior in the iron(II) triflate complex was encountered that originated from the distinct properties associated with the multifaceted crystal chemistry associated with this compound, which is the subject of this chapter.

3.2 EXPERIMENTAL

General Considerations. The compounds $^{H}L^{*}$ and [Ag($^{H}L^{*}$)](OTf) were prepared as described elsewhere.[83] Anhydrous $Fe(OTf)_2$ and $NiCl_2 \cdot 6H_2O$ were purchased from commercial sources, stored under argon in a drybox. Commercial solvents were dried by conventional means and distilled under a nitrogen atmosphere prior to use. The iron(II) complex was prepared under argon using Schlenk line techniques, however, after isolation, it was stored and manipulated under normal laboratory atmospheric conditions.

Instrumentation. Midwest MicroLab, LLC, Indianapolis, Indiana 45250, performed all elemental analyses. Melting point determinations were made on samples contained in glass capillaries using an Electrothermal 9100 apparatus and are uncorrected. IR spectra were recorded for samples as KBr pellets in the 4000-500 cm^{-1} region on a Nicolet Magna-IR 560 spectrometer or on solid samples using a Thermo Scientific Nicolet iS5 IR spectrometer equipped with an iD3 Attenuated Total Reflection (ATR) accessory. ^{1}H NMR spectra were recorded on a Varian 400 MHz spectrometer. Chemical shifts were referenced to residual solvent resonances[150] at δ_H 1.94 for CD_3CN or at δ_H 3.31 for CD_3OD. Solution magnetic moment were measured by the Evan's method.[52a-c] Magnetic

susceptibility data were collected on a Quantum Design MPMS3 SQUID magnetometer. Raw moment data were corrected for sample shape and radial offset corrections using the MPMS 3 Sample Geometry Simulator.[53] Diamagnetic corrections of -372x10^{-6} emu/mol for each *co*-**1** and *cis*-**1** or of -385 x10^{-6} for *trans*-**1**·H_2O, calculated from tabulated Pascal's constants[54] were applied to the measured susceptibility data, as appropriate. Electronic absorption (UV-Vis/NIR) measurements were made on a Cary 5000 instrument. Powder X-ray diffraction patterns were collected with an Oxford Diffraction Ltd. Supernova equipped with a 135 mm Atlas CCD detector.

A. Synthesis

$[Fe(^{H}L^*)_2](OTf)_2$, **1**. A solution of 0.500 g (1.85 mmol) $^{H}L^*$ in 20mL THF was added to a solution of 0.327 g (0.925 mmol) $Fe(OTf)_2$ in 20 mL THF. After the resulting suspension had been stirred 14 h, the colorless solid was collected by cannula filtration, was washed twice with 10 mL Et_2O and was vacuum dried 2 h, to give 0.756 g (91%) of **1** as a colorless powder. A mixture of crystals of colorless, thin needle-like plates of, *cis*-**1** and large blocks of a 1:1 co crystal of *cis*-:*trans*-**1**, or *co*-**1**, were grown by vapor diffusion of Et_2O into 1.5 mL of a 0.025 M solution of **1** in CH_3CN. Single crystals suitable for X-ray diffraction have also been grown by vapor diffusion of Et_2O into methanol solutions that ranged between 0.02 and 0.04 M in **1**. The X-ray quality crystals from this latter solvent system are a mixture of f *cis*-**1**, as well as large block-like crystals (with a pale violet hue when large) for *trans*-**1**·2MeOH. The former of *cis*-**1** retain crystallinity but the latter of *trans*-**1**·2MeOH lose methanol solvent, lose crystallinity, turn violet on drying under vacuum and absorb 1 equivalent of H_2O from the air if

exposed to the atmosphere. The bulk properties were measured using either as-formed powder or hand-separated vacuum dried crystals (exposed to air) as indicated below.

As-isolated powder:

Mp. did not melt below 200°C. Anal. Calcd. (found) for **1**, $C_{30}H_{36}F_6FeN_{12}O_6S_2$: C, 40.28 (40.16); H, 4.06 (4.21); N, 18.79 (18.40). μ_{eff} (Evan's, CD_3OD) = 4.9 μ_B. IR: ν_{NH} (Nujol/KBr) =3139; triflate (Nujol/KBr, s to vs): 1286 (ν_{as}, SO_3), 1256 (ν_s, CF_3), 1160 (ν_{as}, CF_3), 1033 (ν_s, SO_3), 638 (ν_s, SO_3) cm^{-1}. UV-vis [CD_3CN] λ, nm (ε, $M^{-1}cm^{-1}$): 224 (20998), 312 (605), 338 (497). ^1H NMR (CD_3OD) δ_H 48.81, 47.25, 42.95, 41.90, 36.43, 34.95, 20.53, 19.02, -39.24 ppm. ^{19}F NMR (CD_3OD) δ_F -80.02 ppm.

co-**1**: Anal. Calcd. (found) for **1**, $C_{30}H_{36}F_6FeN_{12}O_6S_2$: C, 40.28 (40.07); H, 4.06 (4.04); N, 18.79 (18.66).

cis-**1**:

Anal. Calcd. (found) for *cis*-**1**, $C_{30}H_{36}F_6FeN_{12}O_6S_2$: C, 40.28 (40.29); H, 4.06 (4.08); N, 18.79 (18.79).

trans-**1**·2MeOH vacuum dried, air-exposed:

Anal. Calcd. (found) for *trans*-**1**·H_2O, $C_{30}H_{38}F_6FeN_{12}O_7S_2$: C, 39.48 (39.47); H, 4.20 (4.24); N, 18.42 (18.16).

$[Ni(^HL^*)_2](OTf)_2$, **2**. A solution of 0.200 g (0.380 mmol) $[Ag(^HL^*)](OTf)$ in 10 mL methanol was added to a solution of 0.0451 g (0.190 mmol) $NiCl_2·6H_2O$ in 10 mL H_2O resulting in immediate precipitation of AgCl. After the resulting suspension had been stirred 1 h, it was filtered through Celite, the Celite was washed with 5 mL each H_2O and MeOH, then solvent was removed under vacuum to leave 0.0892 g (52% yield) of **2** as a

pale lilac-colored powder. Mp. did not melt below 200°C. Anal. Calcd. (found) for **2**, $C_{30}H_{36}F_6NiN_{12}O_6S_2$: C, 40.15 (40.16); H, 4.04 (4.21); N, 18.73 (18.40). μ_{eff} (Evan's, CD_3OD) = 3.3 μ_B. IR: ν_{NH} (Nujol/KBr) =3140; triflate (Nujol/KBr, s to vs): 1285 (ν_{as}, SO_3), 1258 (ν_s, CF_3), 1163 (ν_{as}, CF_3), 1032 (ν_s, SO_3), 638 (ν_s, SO_3) cm^{-1}. UV-vis [CD_3OD] λ, nm (ε, $M^{-1}cm^{-1}$): 350 (53), 530 (31), 604 (27), 830 (22), 1431 (9). ^1H NMR (CD_3OD) δ_H 70.79, 51.71, 50.19, 36.31, 4.57, -2.23, -8.67 ppm. ^{19}F NMR (CD_3OD) δ_F -80.00 ppm. Crystals suitable for single crystal X-ray diffraction were grown by vapor diffusion of Et_2O into a 0.03 *M* solution of **2** in methanol.

B. X-ray Crystallography

X-ray intensity data from a violet irregular crystal of *co*-**1**, a violet prism of *cis*-**1**, a violet prism of α-*trans*-**1**·2MeOH, a pink prism of β-*trans*-**1**·2MeOH, a light violet needle of *cis*-**2**, and a light violet prism of *trans*-**2**·2MeOH were collected at 100.0(1) K with an Oxford Diffraction Ltd. Supernova equipped with a 135 mm Atlas CCD detector. The data for *co*-**1** and cis-**1** were also collected at 250 K while that for α-*trans*-**1**·2MeOH were collected at 150 and 250 K. Cu Kα radiation, λ = 1.54184 Å was used for all but two experiments (high temperature experiments of α-*trans*-**1**·2MeOH) for which used Mo Kα (0.70173 Å) radiation. Raw data frame integration and Lp corrections were performed with CrysAlis Pro (Oxford Diffraction, Ltd.).[56] Final unit cell parameters were determined by least-squares refinement of 22417 (100K) and 17127 (250 K) reflections from the data sets of co-**1**, of 18495 (100 K) and 14400 (250 K) reflections from the data sets of *cis*-**1**, 8916 (100 K) and 5722 (150 K) and 7390 (250 K) reflections from data sets of α-*trans*-**1**·2MeOH , of 2422 reflections from data set of β-*trans*-

1·2MeOH, of 10053 and 12941 reflections from the data sets of *cis*-**2** and *trans*-**2**·2MeOH, respectively, with $I > 2\sigma(I)$ for all cases. Analysis of the data showed negligible crystal decay during collection in each case. Direct methods structure solutions were performed with Olex2.solve[57] while difference Fourier calculations and full-matrix least-squares refinements against F2 were performed with SHELXTL.[58] Empirical absorption corrections were applied using spherical harmonics implemented in the SCALE3 ABSPACK scaling algorithm. The hydrogen atom bound to nitrogen of the pyrazol-3-yl group in *cis*-**1** and *trans*-**1**·2MeOH as well as that on oxygen of the methanol solvate molecule(s) were located and refined. All other hydrogen atoms were placed in idealized positions and included as riding atoms.

Special Details: For *co*-**1**, one of the triflate ions is disordered over two nearby positons. The major component (84%) is hydrogen bonded to the pyrazolyl. The minor component occupies an alternative position in a cavity. The content of the cavity could not be elucidated but may involve small amount of unidentified solvent and/or a third orientation of the anion. For *cis*-**1**, one of the triflate anions is well ordered while the other is unequally disordered 67%:33% over two nearby positions. Also a modulated phase with q-vector (0.077 0 0.171) was found at 100 K; no satellites were detected at 250 K. For β-*trans*-**1**·2MeOH, a small single crystal of α- polymorph was mounted on the diffractometer and rapidly cooled to 150 K, then was much more slowly cooled near the phase transition temperature in the range of 140 K to 100 K. During cooling, the sample changed color from colorless (293 K to 250 K) to violet (140 K) to pink (100 K), and after a few minutes at 100 K, the crystal cracked into layers. To prevent an immediate mechanical destruction, the sample was covered in a layer of thick mineral oil.

The resulting polycrystal contained appropriately large domains of the original phase and the new phase (along with many smaller domains). To separate the multiple overlapping diffraction patterns, short 0.3° ω-scans were employed. Under these most favorable conditions, a 75% experiment completeness was achieved before the sample was ultimately destroyed due to mechanical stress during the data collection.

C. Powder X-ray Diffraction

Under a microscope, crystals of α-*trans*-**1**·2MeOH were manually separated from the mixture in the crystallization mother liquor. The separation was imperfect as very small quantity of tiny needles/fragments of *cis*-**1** was also present. Regardless, the separated crystals of mostly α-*trans*-**1**·2MeOH were then ground in mineral oil to give a spheroid of approximate dimensions 0.3 x 0.3 x 0.5 mm that was mounted on a diffractometer that was pre-cooled to 150 K. Diffraction data were collected after 15 min at this temperature. Then, the sample was cooled to 100 K in 10 K steps and data were collected 30 to 40 min after each step temperature was attained; changes to the appearance of the sample were noticeable at 130 K and below. After reaching 100 K, the sample was held for 1.5 hr, then data were collected. Afterward, the temperature was raised to 150 K, the sample was equilibrated 40 min, then data were re-collected. Finally, the sample was annealed by warming to 293 K and held 5 min, then the sample was re-cooled to 150 K held 10 min, and data were recollected.

Identification code	*co*-**1**, 250 K	*co*-**1**, 100K	*cis*-**1**, 250 K	*cis*-**1**, 100K
Empirical formula	$C_{30}H_{36}F_6FeN_{12}O_6S_2$	$C_{30}H_{36}F_6FeN_{12}O_6S_2$	$C_{30}H_{36}F_6FeN_{12}O_6S_2$	$C_{30}H_{36}F_6FeN_{12}O_6S_2$
Formula weight	894.68	894.68	894.68	894.68
Temperature/K	250.0(1)	100.0(3)	250.0(1)	100.1(6)
Crystal system	monoclinic	monoclinic	monoclinic	monoclinic
Space group	I2/a	I2/a	$P2_1/c$	$P2_1/c$
a/Å	23.1055(3)	22.96795(18)	12.9325(3)	12.78177(10)
b/Å	13.2707(2)	13.20086(9)	21.3789(4)	21.02035(20)
c/Å	27.9530(4)	27.72924(19)	14.7731(3)	14.74699(12)
α/°	90.00	90.00	90.00	90.00
β/°	108.6125(16)	108.3556(8)	103.050(2)	103.0849(8)
γ/°	90.00	90.00	90.00	90.00
Volume/Å^3	8122.8(2)	7979.65(10)	3979.02(15)	3859.30(6)
Z	8	8	4	4
ρ_{calc} g/cm^3	1.463	1.489	1.493	1.540
μ/mm^{-1}	4.683	4.767	4.780	4.928
F(000)	3680	3680	1840	1840
Crystal size/mm^3	0.39 × 0.356 × 0.208	0.39 × 0.356 × 0.208	0.383 × 0.233 × 0.144	0.383 × 0.233 × 0.144
Radiation	CuKα (λ = 1.54184)	CuKα (λ = 1.54184)	CuKα (λ = 1.54184)	CuKα (λ = 1.54184)
2Θ range for data collection/°	7.46 to 148.12	7.5 to 148.3	7.02 to 149.22	7.1 to 148.28
Index ranges	-22 ≤ h ≤ 28, -13 ≤ k ≤ 16, -34 ≤ l ≤ 34	-28 ≤ h ≤ 23, -16 ≤ k ≤ 16, -34 ≤ l ≤ 34	-15 ≤ h ≤ 16, -26 ≤ k ≤ 26, -18 ≤ l ≤ 18	-15 ≤ h ≤ 15, -25 ≤ k ≤ 25, -18 ≤ l ≤ 18
Reflections collected	29314	38795	36060	37282
Independent reflections	8118 [R_{int} = 0.0332, R_{sigma} = 0.0239]	8025 [R_{int} = 0.0277, R_{sigma} = 0.0180]	7971 [R_{int} = 0.0424, R_{sigma} = 0.0312]	7739 [R_{int} = 0.0279, R_{sigma} = 0.0191]
Data/restraints/parameters	8118/19/524	8025/38/557	7971/143/603	7739/95/603
Goodness-of-fit on F^2	1.053	1.060	1.098	1.034
Final R indexes [I ≥ 2σ (I)]	R_1 = 0.0498, wR_2 = 0.1474	R_1 = 0.0703, wR_2 = 0.1988	R_1 = 0.0517, wR_2 = 0.1398	R_1 = 0.0360, wR_2 = 0.0928
Final R indexes [all data]	R_1 = 0.0509, wR_2 = 0.1492	R_1 = 0.0718, wR_2 = 0.2004	R_1 = 0.0651, wR_2 = 0.1650	R_1 = 0.0396, wR_2 = 0.0958
Largest diff. peak/hole / e Å^{-3}	1.11/-1.00	4.16/-0.96	0.47/-0.56	0.36/-0.48

[a] $R_1 = \Sigma||F_o| - |F_c||/\Sigma|F_o|$ [b] $wR_2 = [\Sigma w(|F_o| - |F_c|)^2/\Sigma w|F_o|^2]^1$

Table 3.1. Crystal data and structure refinement for 1:1 *cis*-:*trans*- co-crystal of Fe(^{H}L*)$_2$](OTf)$_2$, *co*-**1,** and [*cis*-Fe(^{H}L*)$_2$](OTf)$_2$, *cis*-**1**.

Identification code	*trans*-**1**·2MeOH	*trans*-**1**·2MeOH	*trans*-**1**·2MeOH	*trans*-**1**·2MeOH
Empirical formula	$C_{32}H_{44}F_6FeN_{12}O_8S$	$C_{32}H_{44}F_6FeN_{12}O_8S$	$C_{32}H_{44}F_6FeN_{12}O_8S$	$C_{32}H_{44}F_6FeN_{12}O_8S$
Formula weight	958.76	958.76	958.76	958.76
Temperature/K	250.0(1)	150.0(1)	100.3(6)	100.1(3)
Crystal system	monoclinic	monoclinic	monoclinic	monoclinic
Space group	$P2_1/c$	$P2_1/c$	$P2_1/c$	$P2_1/c$
a/Å	12.0272(3)	11.8540(5)	11.81322(18)	12.8426(8)
b/Å	12.3220(3)	12.1331(3)	12.00602(15)	12.1447(8)
c/Å	15.0632(4)	15.0817(5)	15.0970(2)	14.0980(14)
α/°	90.00	90.00	90.00	90.00
β/°	103.555(3)	103.213(3)	103.1296(15)	111.737(9)
γ/°	90.00	90.00	90.00	90.00
Volume/Å^3	2170.18(9)	2111.70(12)	2085.24(5)	2042.5(3)
Z	2	2	2	2
ρ_{calc} g/cm^3	1.467	1.508	1.527	1.559
μ/mm^{-1}	0.530	0.545	4.637	4.734
F(000)	992	992	992	992
Crystal size/mm^3	0.232 × 0.213 × 0.12	0.232 × 0.213 × 0.12	0.158 × 0.108 × 0.065	0.25 × 0.22 × 0.18
Radiation	MoKα (λ = 0.71073)	MoKα (λ = 0.71073)	CuKα (λ = 1.54184)	CuKα (λ = 1.54184)
2Θ range for data	6.7 to 59.1	6.72 to 58.98	7.68 to 148.16	7.42 to 148.86
Index ranges	-16 ≤ h ≤ 16, -16 ≤ k ≤ 16, -20 ≤ l ≤ 20	-16 ≤ h ≤ 13, -16 ≤ k ≤ 15, -20 ≤ l ≤ 20	-14 ≤ h ≤ 14, -13 ≤ k ≤ 14, -18 ≤ l ≤ 18	-16 ≤ h ≤ 13, -14 ≤ k ≤ 10, -13 ≤ l ≤ 12
Reflections collected	24363	20178	20162	7770
Independent reflections	5577 [R_{int} = 0.0378, R_{sigma} = 0.0334]	5365 [R_{int} = 0.0426, R_{sigma} = 0.0467]	4181 [R_{int} = 0.0290, R_{sigma} = 0.0209]	3131 [R_{int} = 0.0608, R_{sigma} = 0.0501]
Data/restraints/parameter	5577/0/287	5365/0/287	4181/0/291	3131/0/290
Goodness-of-fit on F^2	1.030	1.030	1.018	1.155
Final R indexes [I ≥ 2σ (I)]	R_1 = 0.0487, wR_2 = 0.1233	R_1 = 0.0498, wR_2 = 0.1170	R_1 = 0.0305, wR_2 = 0.0780	R_1 = 0.0796, wR_2 = 0.2464
Final R indexes [all data]	R_1 = 0.0792, wR_2 = 0.1441	R_1 = 0.0823, wR_2 = 0.1361	R_1 = 0.0355, wR_2 = 0.0823	R_1 = 0.0912, wR_2 = 0.2605
Largest diff. peak/hole / e Å^{-3}	0.40/-0.42	0.49/-0.70	0.28/-0.34	0.95/-0.74

[a] $R_1 = \Sigma||F_o| - |F_c||/\Sigma|F_o|$ [b] $wR_2 = [\Sigma w(|F_o| - |F_c|)^2/\Sigma w|F_o|^2]^1$

Table 3.2. Crystal data and structure refinement for two polymorphs of [trans-Fe(HL*)$_2$](OTf)$_2$·2MeOH, α-*trans*-**1**·2MeOH and β-trans-**1**·2MeOH.

Identification code	*cis*-**2**, 100K	*trans*-**2**·2MeOH
Empirical formula	$C_{30}H_{36}F_6NiN_{12}O_6S_2$	$C_{32}H_{44}F_6NiN_{12}O_8S_2$
Formula weight	897.54	961.62
Temperature/K	100.15	100.15(1)
Crystal system	triclinic	monoclinic
Space group	P-1	$P2_1/c$
a/Å	12.8153(3)	11.79415(11)
b/Å	13.0608(3)	12.10706(13)
c/Å	14.7332(3)	15.06185(13)
α/°	64.985(2)	90.00
β/°	76.5464(19)	103.1806(9)
γ/°	60.976(2)	90.00
Volume/Å^3	1952.88(8)	2094.06(3)
Z	2	2
ρ_{calc} g/cm^3	1.526	1.525
μ/mm^{-1}	2.490	2.397
F(000)	924	996
Crystal size/mm^3	0.323 × 0.133 × 0.082	0.313 × 0.253 × 0.171
Radiation	CuKα (λ = 1.54184)	CuKα (λ = 1.54184)
2Θ range for data collection/°	6.62 to 131.42	7.7 to 141.8
Index ranges	-15 ≤ h ≤ 15, -15 ≤ k ≤ 14, -17 ≤ l ≤ 17	-14 ≤ h ≤ 14, -13 ≤ k ≤ 14, -18 ≤ l ≤ 18
Reflections collected	12910	19117
Independent reflections	12910 [R_{int} = 0.0000, R_{sigma} = 0.0162]	3981 [R_{int} = 0.0169, R_{sigma} = 0.0115]
Data/restraints/parameters	12910/0/531	3981/0/292
Goodness-of-fit on F^2	1.061	1.057
Final R indexes [I ≥ 2σ (I)]	R_1 = 0.0464, wR_2 = 0.1242	R_1 = 0.0283, wR_2 = 0.0762
Final R indexes [all data]	R_1 = 0.0548, wR_2 = 0.1331	R_1 = 0.0292, wR_2 = 0.0770
Largest diff. peak/hole / e Å^{-3}	0.92/-0.42	0.53/-0.43

[a] $R_1 = \Sigma||F_o| - |F_c||/\Sigma|F_o|$ [b] $wR_2 = [\Sigma w(|F_o| - |F_c|)^2/\Sigma w|F_o|^2]^{1/2}$

Table 3.3. Crystal data and structure refinement for [*cis*-Ni(^{H}L*)$_2$](OTf)$_2$, *cis*-**2**, and [*trans*-Ni(^{H}L*)$_2$](OTf)$_2$·2MeOH, *trans*-**2**·2MeOH.

3.3 RESULTS AND DISCUSSION

The reaction between ^{H}L* and $Fe(OTf)_2$ in a 2:1 mol ratio in THF produced a colorless precipitate of $[Fe(^{H}L^*)_2](OTf)_2$, **1**, in high yield after filtration and vacuum drying. Recrystallization by vapor diffusion of Et_2O into CH_3CN solutions gives mostly elongated needles or plates of *cis*-**1** and some large isometric blocks of a 1:1 co-crystal of *cis*-**1**:*trans*-**1**, named *co*-**1** (Figure 3.1). The quantity of *co*-**1** increases relative to *cis*-**1** after a second recrystallization of the initial mixture of crystals. On the other hand, dissolution of the initial precipitate of **1** in methanol followed by vapor diffusion gave a mixture of X-ray quality crystals; elongated needles or plates of *cis*-**1** and large cubic/octahedral blocks of *trans*-**1**·$2CH_3OH$ (Figure 3.2) The quantity of *cis*- and *trans*-isomer is approximately equal by mass.

Figure 3.1. Photographs (left and center are the same but under different external lighting) of the mixture of crystals obtained after recrystallization of **1** by vapor diffusion of Et_2O into a 0.025 *M* CH_3CN, filtering, and after drying under vacuum.

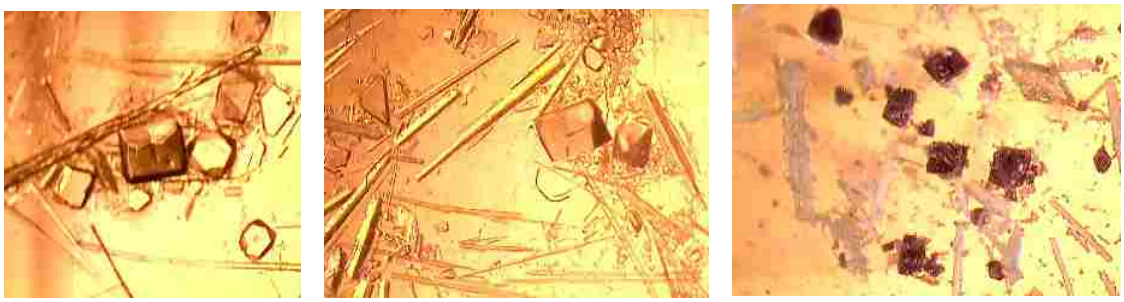

Figure 3.2. Photographs of the mixture of crystals obtained after vapor diffusion of Et_2O

into a 0.02 *M* methanol solution of $[Fe(^{H}L^{*})_2](OTf)_2$, **1** (left and center) and after drying under vacuum (right).

If manually separated crystals are recrystallized, a mixture of crystals is again obtained, indicating that isomerization occurs in solution. When removed from crystallization solvent, *cis*-**1** retains crystallinity but *trans*-**1**·$2CH_3OH$ does not. The latter slowly (minutes to hours) loses solvent under atmospheric conditions (or more quickly under vacuum), becoming opaque and concomitantly turning violet, a color characteristic of LS iron(II) (Fig. 3.2, right).

The crystals of *co*-**1** turn violet on cooling in liquid nitrogen, so single crystal X-ray diffraction experiments were performed at both 250 K (colorless) and 100 K (violet). Views of the 100 K structure are found in Figure 3.3, while bond distances and interatomic angles are listed in Table 3.4. The asymmetric unit consists of one well-ordered triflate (with terminal atoms bound to the S1-C5 unit), one triflate that is disordered unequally over two nearby positions (84% containing S1a-C5a and 16% containing S1b-C5b) and two Fe(^{H}L*) moieties (one with Fe1 on an inversion center and one with Fe2 on a two-fold rotation axis). Thus, the dication with Fe1 is

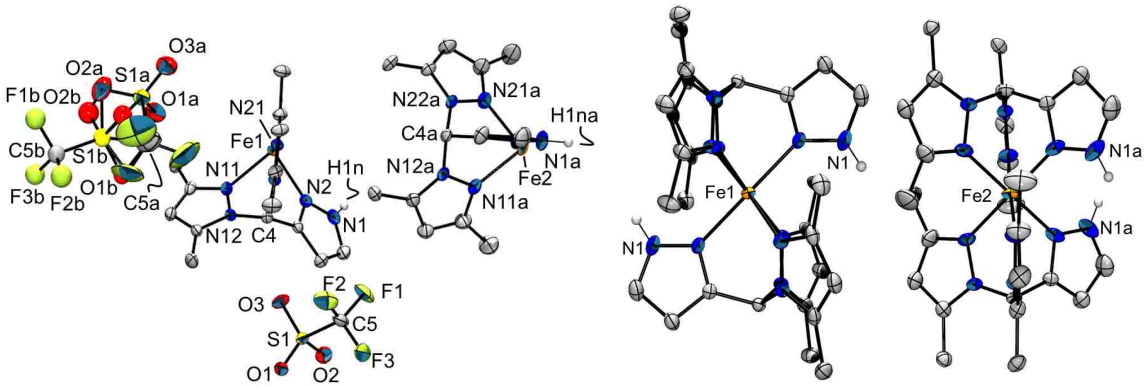

(a) (b)

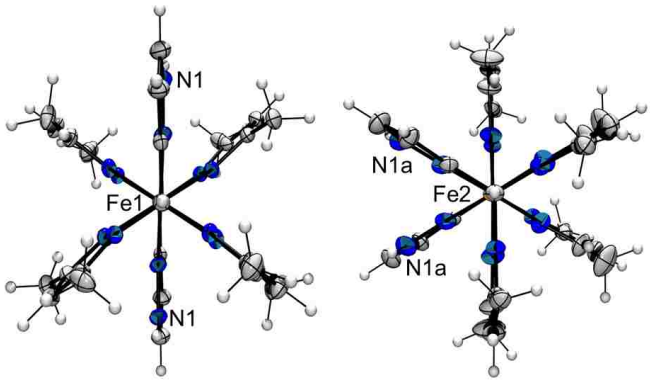

(c)

Figure 3.3. Views of the structure of a 1:1 co-crystal of *cis*-**1**:*trans*-**1**, *co*-**1.** (a) asymmetric unit with partial atom labelling and most hydrogen atoms removed. (b) View of the *trans*- (left) and *cis*- (right) dication components. (c) View of the dications down the C(methine)-H bond showing greater pz ring tilting in the *trans*-isomer (left) than the *cis*- (right).

Bond Distances (Å)	250 K	100 K
Fe1-N2	2.1321(19)	2.103(3)
Fe1-N11	2.2059(18)	2.163(3)
Fe1-N21	2.1850(18)	2.154(3)
Fe2-N2a	2.132(2)	2.032(4)
Fe2-N11a	2.178(2)	2.087(3)
Fe2-N21a	2.156(2)	2.064(3)
Bond Angles (°)		
N2-Fe1-N11	85.32(7)	85.68(11)
N2-Fe1-N21	84.10(7)	84.82(11)
N11-Fe1-N21	82.38(7)	83.07(10)
N2a-Fe2-N11a	85.83(8)	86.83(13)
N2a-Fe2-N21a	82.26(8)	84.35(13)
N11a-Fe2-N21a	85.94(8)	87.11(13)
Bond Torsions (°)		
C4C3-N2Fe1	-6.1(3)	-6.1(4)
C4N12-N11Fe1	-4.9(2)	-5.0(4)
C4N22-N21Fe1	-2.2(2)	-3.2(4)
C4aC3a-N2aFe2	-6.9(3)	-5.4(4)
C4aN12a-N11aFe2	-4.5(3)	-3.8(4)
C4aN22a-N21aFe2	5.9(3)	4.4(4)

Table 3.4. Bond distances (Å), angles (deg.) and torsion angles (deg.) for *co*-**1.**

the *trans*- isomer (angle between iron-bound 'confused' nitrogens, N2-Fe1-N2' = 180.0(1)^{o}) whereas that with Fe2 is the *cis*-isomer (N2-Fe2-N2' = 92.5(2)^{o}). At 250 K, the average Fe-N bond distances indicate that both the *trans*- (2.17 Å) and *cis*- (2.16 Å) components are HS. At 100 K, the *trans*- isomer remains HS (Fe-N_{avg} 2.14 Å) while the *cis*-isomer has Fe-N_{avg} of 2.06 Å, a distance intermediate between HS and LS (ca. 1.98 Å). It is noteworthy that the *trans*- component not only has longer bond distances than the *cis*- but the ligand is more distorted with greater pyrazolyl ring twisting (avg. of the absolute values of two FeN-$NC_{methine}$ and Fe-N2-C3$C_{methine}$ torsion angles; 5.8 vs 4.4^{o} at 250 K or 4.8 vs 4.5^{o} at 100 K relative to a value of 0^{o} being untwisted) and ring tilting (avg of the absolute values of the two FeN-NC_{pz} and the FeN2-C3C2 torsion angles; 171^{o} vs 175^{o} at 250 K or 172^{o} vs 176^{o} at 100 K with a value of 180^{o} being untilted). In other words, the least distorted HS complex with shorter bonds undergoes SCO first on cooling (albeit incomplete over this temperature range).

Since the abruptness in spin transition is thought to increase with the strength of intermolecular interactions, the examination of the three-dimensional supramolecular structure is important to inform further studies in crystal engineering SCO behavior. Views of the crystal packing arrangement are found in Figure 3.4, while Table 3.5 lists the short non-covalent interactions that help organize the structure.

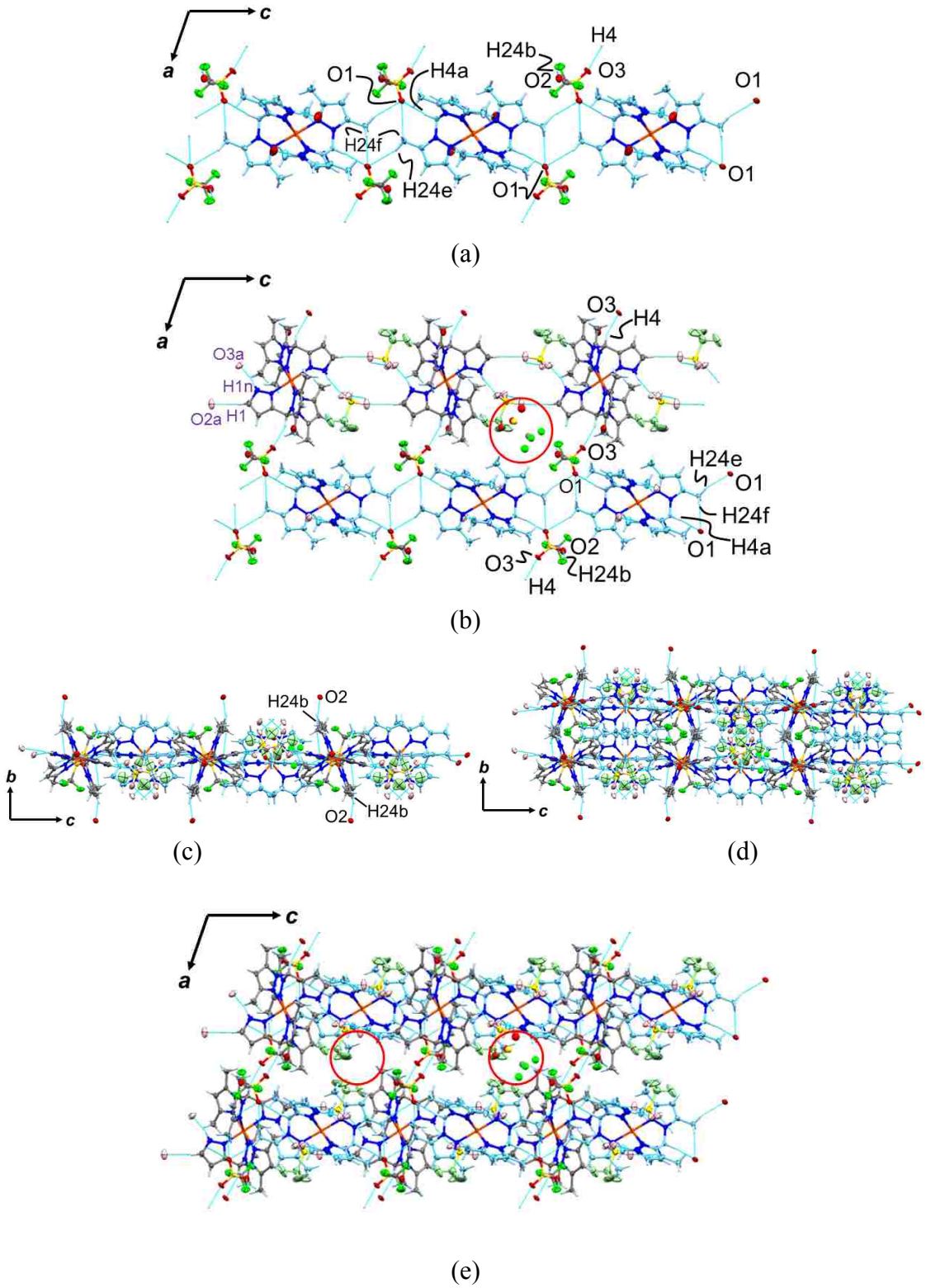

Figure 3.4. Supramolecular structure of *co*-**1**. (a) View down *b* of polymeric chain along *c*-axis (b) view down *b* of *ac*-sheet with major disorder component in pastel colors and the minor circled; (c) view of *ac*-sheet down *a*. (d) stacking of sheets as viewed

down *a*- axis. (e) View down *b* of two stacked sheets with the cavities where minor disorder component is found circled.

Donor(D)(-H)	D-H (Å)	H···A	D···A	D-H···A
ordered triflate				
C2-H2···O3	0.95	2.60	3.286(5)	130
C4-H4···O3	1.00	2.24	3.182(5)	157
C4a-H4a···O1	1.00	2.26	3.211(4)	158
C14-H14a···O3	0.98	2.57	3.434(5)	147
C24-H24b···O2	0.98	2.46	3.366(5)	154
C24-H24e···O1	0.98	2.55	3.477(5)	158
C24-H24f···O1	0.98	2.42	3.279(5)	145
disordered				
N1a-	0.88	1.96	2.807(5)	162
N1-H1n···O1a	0.88	1.93	2.744(5)	154
C1-H1···O2a	0.95	2.45	3.395(6)	173
C1-H1···O2b	0.95	2.53	3.40(2)	153
C1a-H1a···O3b	0.95	2.54	3.20(2)	120
C10a-	0.98	2.59	3.34(2)	133
C22a-	0.98	2.48	3.269(18)	137
C22a-	0.98	2.25	2.868(18)	122
C2-H2···F1b	0.95	2.48	2.977(18)	113

Table 3.5. Geometries of selected weak hydrogen-bonding interactions in *co*-**1** at 100 K.

The three-dimensional structure of the complexes at 250 K and 100 K are nearly identical, so we will discuss the more complicated 100 K structure first. As stated above there are two triflate anions, one well-ordered and one disordered. The three-dimensional structure can be constructed by only considering charge-assisted C-H···O weak hydrogen bonding interactions[151] with the former. The well-ordered triflate bridges *cis*- isomer components of a polymeric chain that runs along *c*- via a trifurcated C-H···O interactions[151] involving O1 as a bridging acceptor to a 5-methyl hydrogen donor (H24e) on one complex and both a methine (H4a) and nearby 5-methyl hydrogen (H24f) donor on a neighboring complex, Figure 3.4a. The interaction of O3 on one chain with the

methine hydrogen of the *trans*- isomer on another chain stacks polymers along *a*- into sheets parallel with the *ac*- plane, Figures 3.4b and 3.4c. The sheets are stacked along *b* by the interaction between O2 on one sheet and a 5-methyl hydrogen of a pz* group on an adjacent sheet. The other non-covalent interactions listed in Table 3.5 further secure this structure. The second, disordered triflate is located within voids of the supramolecular framework. The major disorder component is hydrogen bonded to the trans- isomer via N-H···O hydrogen bonding interactions[152,153] (pastel colored triflate, Figure 3.4c). The minor component is also hydrogen bonded to the *trans*- isomer, but does not bridge neighboring trans-isomers within the polymer chain, rather short C-H···F weak hydrogen bonding interactions[154] occur with the *cis*- isomer of neighboring polymers. At 250 K, the overall connectivity is retained, but non-covalent interactions lengthen. Also, the minor triflate disorder component is not observed instead, there are solvent accessible voids 162 Å ^{3} in the same location as the 100 K structure, that may contain the second component at 250 K.

Single crystal X-ray diffraction data was obtained for a colorless needle of *cis*-**1** at 250 K and then after cooling the needle to 100 K after it turned violet (Figure 3.5). A listing of selected bond distances and interatomic angles for *cis*-**1** at different temperatures are provided in Table 3.6. The compound crystallizes in the space

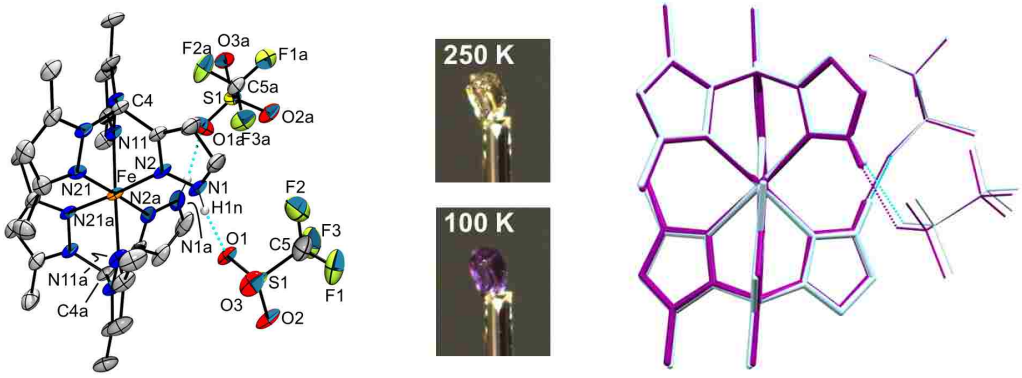

Figure 3.5. Left: Structure of *cis*-[Fe(^{H}L*)$_2$](OTf)$_2$, *cis*-**1**, at 100 K; Middle: Photographs of a crystal at different temperature; Right: Overlay of structures obtained at 250 K (light blue) and 100 K (violet).

group $P2_1/c$ where the asymmetric unit is composed of one cation, one well-ordered triflate anion, and another triflate anion that is disordered unequally (2:1) over two nearby positions. The FeN_6 coordination environment is distorted octahedral since the Fe-N bonds of the confused pyrazolyl are at least 0.02 Å shorter than those of the (inequivalent) pz* groups. At 250 K, the average Fe-N bond distance of the six bonds is 2.17 (2) Å, which is aligned with expectations for HS iron(II). At 100 K, the average distance shortens to 2.11 (2) Å, indicative of an increasing portion of LS iron(II). For reference, the compound [Fe(^{Bn}L)$_2$](BF$_4$)$_2$·2CH$_3$CN (with an N-benzyl on the 'confused' pyrazolyl and unsubstituted 'normal' pyrazolyls) had an average Fe-N bond distance of 2.14 Å at 250 K (partly LS) and 1.99 Å at 100 K (fully LS).[50] The complex [Fe(^{H}L)$_2$](BF$_4$)$_2$ with 100% LS iron(II) had an average Fe-N bond distance of 1.97 Å at 100 K.[50] In *cis*-**1**, the average pyrazolyl ring twist is 6° at both temperatures; thus, spin crossover behavior is expected and is observed in this case, vide infra.

	250 K	100 K
Bond Distances (Å)		
Fe1-N2	2.146(2)	2.0849(17)
Fe1-N11	2.173(2)	2.1089(14)
Fe1-N21	2.192(2)	2.1356(15)
Fe1-N2a	2.146(2)	2.0833(16)
Fe1-N11a	2.196(2)	2.1404(16)
Fe1-N21a	2.177(2)	2.1242(17)
Bond Angles (°)		
N2-Fe1-N11	82.57(9)	83.46(6)
N2-Fe1-N21	83.77(9)	84.47(6)
N11-Fe1-N21	85.25(9)	86.14(5)
N2a-Fe1-N11a	82.36(9)	83.52(6)

N2a-Fe1-N21a	83.75(9)	84.29(6)
N11a-Fe1-N21a	85.52(9)	86.59(6)
Bond Torsions (°)		
C4C3-N2Fe1	-9.3(3)	-8.3(2)
C4N12-N11Fe1	2.3(3)	1.7(2)
C4N22-N21Fe1	-9.7(3)	-9.1(2)
C4aC3a-N2aFe1	-2.7(3)	-3.9(2)
C4aN12a-N11aFe1	5.5(3)	3.2(2)
C4aN22a-N21aFe1	-8.3(3)	-10.8(2)

Table 3.6. Bond distances (Å), angles (deg.) and torsion angles (deg.) for *cis*-**1.**

The three-dimensional supramolecular structure of *cis*-**1** is constructed from N-H···O, C-H···O, and C-H···F weak charge-assisted hydrogen bonding interactions involving hydrogen donors of the dications and either oxygen or fluorine acceptors of the triflate anions. To simplify the structural description, the geometries of only a few of the interactions needed to construct the three-dimensional framework are given in Table 3.7. One of the triflate anions is disordered in a 2:1 ratio over two

Donor(D)(-H)	D-H	H···A	D···A	D-H···A
N1-H1n···O1	0.83(3)	1.98(3)	2.795(2)	170(3)
N1a-	0.83(3)	1.96(3)	2.678(3)	143(2)
N1a-	0.83(3)	2.29(3)	3.103(5)	165(3)
C2a-H2a···O2	0.95	2.55	3.243(3)	130
C4a-H4a···O2	1.00	2.26	3.188(2)	154
C24a-	0.98	2.48	3.401(3)	156
C12-H12···O2	0.95	2.56	3.445(2)	156
C22-H22···O3	0.95	2.48	3.190(2)	132
C4-H4···O2a	1.00	2.23	3.157(14)	154
C4-H4···O2b	1.00	2.42	3.34(3)	153
C2-H2···O2a	0.95	2.54	3.22(2)	128
C2-H2···O2b	0.95	2.57	3.29(3)	133
C20a-	0.98	2.44	3.420(5)	176

Table 3.7. Geometries of main N-H···O and C-H···O weak hydrogen-bonding interactions in *cis*- **1** at 100 K.

positions, thus the discussion will first focus on the well-ordered triflate anion (with atoms O1, O2, and O3). A sheet of cations is formed in the *ac*- plane by N-H···O and C-H···O weak hydrogen-bonding interactions involving these well-ordered triflate anions, Figure 3.6. That is, a dimer is formed by a pair of triflate anions bridging two dications where O1 of the triflate interacts with the N-H of the confused pyrazolyl (N1-H1n···O1, 1.98 Å) on one cation and O2 interacts with the methine hydrogen of the neighboring dication (Figure 3.6a-3.6c). The dimers are organized into sheets parallel with the *ac*-plane by interactions of O2 and O3 of one dimer with the hydrogens at the 4-positions of the dimethylpyrazolyl groups of neighboring dimers (C12-H12···O2 2.56 Å; C22-H22···O3 2.48 Å).

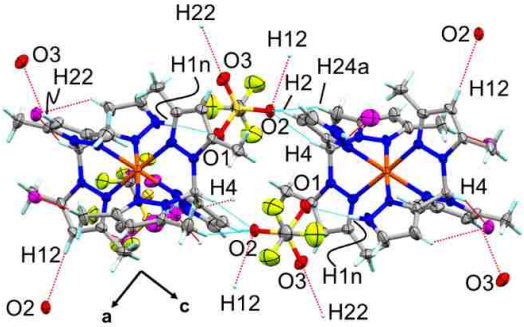

(a)

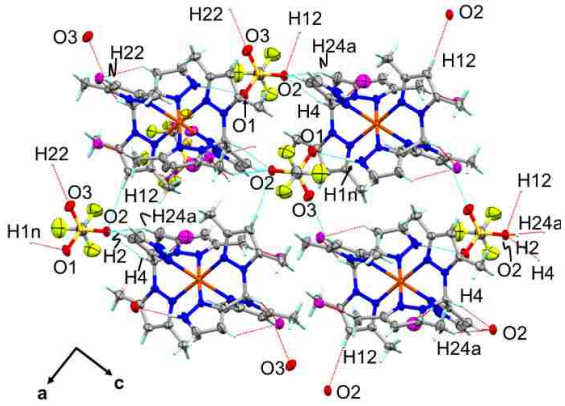

(b)

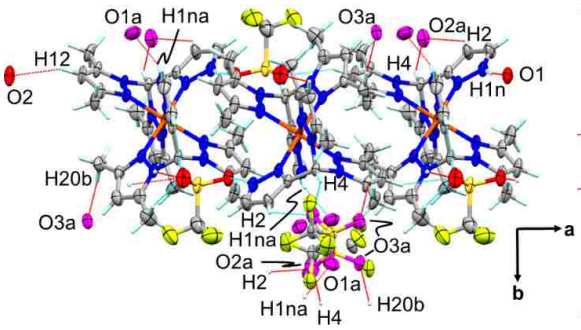

(c)

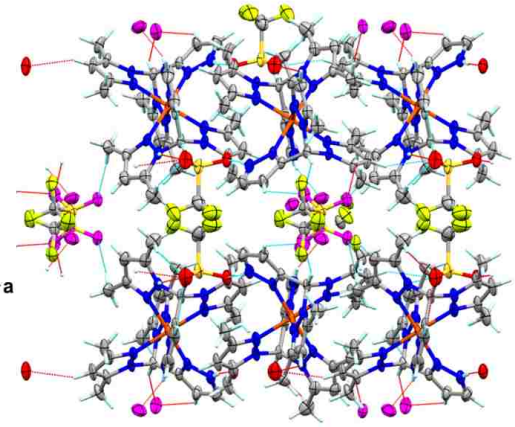

(d)

Figure 3.6. Supramolecular structure of *cis*-**1**. (a) dimeric units viewed down *b*. Red dashed lines: Hanging contacts. Cyan dashed lined completed contacts; (b) Assembly of dimers to form sheet in *ac*-plane. (c) View down side of sheet. Disordered triflate oxygen atoms are magenta and labeled Oxa (x = 1,2,3). (d) stacking of sheets along *b*.

The *ac*-sheets are stacked along the *b*-axis by hydrogen bonding interactions with oxygen atoms of the disordered triflate (Figure 3.6d). It is important to note that each component of the disorder falls well below the limits for NH···O or CH···O interactions. Thus, 67% of the time the confused pyrazolyl N-hydrogen, H1na, is hydrogen bonded to O1a (1.96(3) Å) while the other 33% it is hydrogen bonded to O1b (2.29(3) Å); the latter is 0.46 Å shorter than the sum of the van der Waals radii (Σ_{vdw} (N,H) = 2.75 Å) and the associated N···O distance of 3.103(5) Å is in the range of a medium-strength hydrogen bond.[153] Similarly, the acidic methine hydrogen, H4, of one *ac*-sheet acts as a donor to O2a (2.23 Å) of a triflate from an adjacent sheet 67% of the time and to O2b (2.42 A) the other 33% of the time; both associated C···O distances (3.16, 3.34 Å, respectively) are well within the accepted limits for a CH···O interaction.[151,155] The minor component of the disordered triflate also has a number of CH···F weak hydrogen bonding interactions that serve to support the structure but will not be discussed further. The overall supramolecular structure is retained at 250 K but all contacts are elongated versus those at 100 K.

Two crystalline modifications of *trans*-**1**·2MeOH have been identified by powder and single crystal X-ray diffraction, a high temperature form (α–) and a low temperature form (β–). Importantly, small crystals of the high temperature form undergo a slow enough phase transformation at 100 K to allow a full diffraction data collection before crystal shattering due to phase transformation can occur. In certain cases, during the

phase transformation at 100 K, small domains of β-*trans*-**1**·2MeOH could be kinetically trapped long enough for nearly complete (75%) data collection before mechanical stress completely shatters the domains. Both forms crystallize in the monoclinic system ($P2_1/c$) but with different unit cell parameters and different hydrogen bonding patterns. Views of the structures of α- and β-*trans*-**1**·2MeOH obtained at 100 K are found in Figures 3.7a and 3.7b, respectively. Selected bond distances and interatomic angles are provided in Table 3.8. As with *cis*-**1**, the iron center in both forms of *trans*-**1**·2MeOH, are distorted (compressed) octahedral as a result of the Fe-N bond of the confused pyrazolyl being about 0.05 Å shorter than the Fe-N bonds of the pz* groups. The average Fe-N distance in α-*trans*-**1**·2MeOH at 250 K of 2.15 Å is indicative of HS iron(II) whereas that at 100 K shrinks to 2.02 Å, which suggests approximately 50% HS character. After the phase transition to β-*trans*-**1**·2MeOH at 100 K, the average Fe-N distance falls to 1.98 Å, the typical distance for LS iron(II). Moreover, the pz-twist for α-*trans*-**1**·2MeOH is 6^o at both 250 K and 100 K while that for β-*trans*-**1**·2MeOH is 2^o, likely reflecting both differences in spin state and crystal packing. Another significant difference in the α- and β- forms of *trans*-**1**·2MeOH is also evident in the second coordination sphere. In each case the methanol solvate is hydrogen bonded to the confused pyrazolyl N-H moiety (N1-H1n···O4: α- 1.84(2) Å; β- 1.93(8) Å). In turn, the triflate anion is hydrogen bonded to the methanol solvate (O4-H4s···O2: α- 2.00(4) Å; β- 2.13(9) Å). In the α- form, the triflate is anchored to the confused pyrazolyl via a short C1-H1···O2 (2.44 Å; C···O, 3.146(2) Å) interaction. In β-*trans*-**1**·2MeOH, the triflate bound to methanol is more remote from the confused pyrazolyl; the nearest contact to H1 is with O2 at 6.15 Å (C1···O2, 6.25 Å).

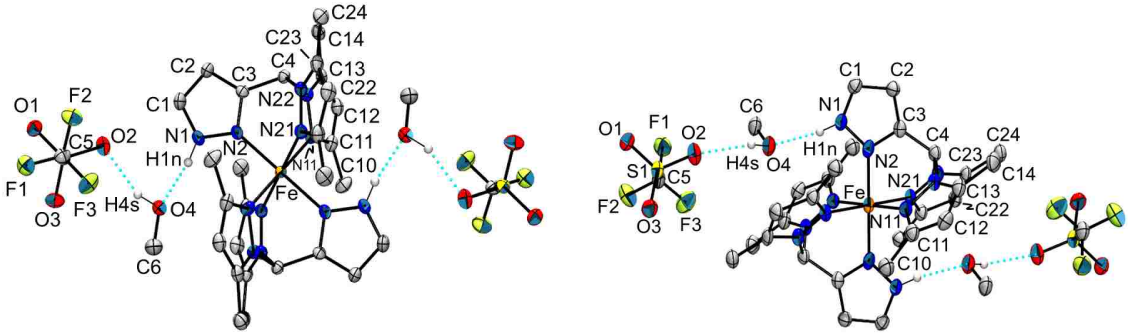

Figure 3.7. Views of the cations in (a) α-*trans*-**1**·2MeOH and (b) β-*trans*-**1**·2MeOH with partial atom labeling and most hydrogen atoms removed for clarity.

	α-*trans*-**1**·2MeOH		β-*trans*-**1**·2MeOH
	250 K	100 K	100 K
Bond Distances			
Fe1-N2	2.116(2)	1.9813(15)	1.943(5)
Fe1-N11	2.1634(19)	2.0354(15)	1.992(5)
Fe1-N21	2.173(2)	2.0382(15)	1.998(4)
Bond Angles (°)			
N2-Fe1-N11	85.11(7)	87.17(5)	87.8(2)
N2-Fe1-N21	85.08(7)	87.42(5)	88.09(17)
N11-Fe1-N21	82.70(7)	85.54(6)	87.33(19)
Bond Torsions (°)			
C4C3-N2Fe1	5.5(3)	5.35(19)	1.0(7)
C4N12-N11Fe1	7.8(2)	8.00(17)	1.1(5)
C4N22-N21Fe1	5.0(3)	4.41(17)	3.3(6)

Table 3.8. Bond distances (Å), angles (deg.) and torsion angles (deg.) for α-*trans*-**1**·2MeOH at 250 K and 100 K and for β-*trans*-**1**·2MeOH at 100 K.

In this case, the triflate ion has reoriented to interact with neighboring cations, as described below.

Despite the apparent difference in structures as depicted in Figure 3.7, the overall supramolecular structure of each form of *trans*-**1**·2MeOH is quite similar. The three-dimensional structure of each polymorph is of sheets stacked by slightly different weak hydrogen bonding interactions due to different orientations of solvate methanol and of

anions. The geometries of the intermolecular interactions of each polymorph in their 100 K structures are given in Table 3.9. Views of the supramolecular structures that highlight the hydrogen bonding pattern most easily are given in Figures 3.8-3.10. The supramolecular structure of α-*trans*-**1**·2MeOH can be described by considering the charge-assisted D-H···O (D = C, N, O) weak hydrogen bonding interactions.

Donor(D)(-H)	D-H (Å)	H···A	D···A	D-H···A
-trans-				
N1-H1n···O4	0.87(2)	1.84(2)	2.698(2)	169(2)
O4-H4s···O2	0.87(4)	2.00(4)	2.826(2)	158(3)
C1-H1···O2	0.95	2.44	3.146(2)	131
C4-H4···O1	1.00	2.34	3.291(2)	159
C10-H10c···O2	0.98	2.53	3.410(2)	149
C12-H12···O2	0.95	2.60	3.414(2)	144
C14-H14c···O3	0.98	2.48	3.374(2)	151
C24-H24b···F2	0.98	2.52	3.434(2)	154
C24-H24c···O1	0.98	2.56	3.293(2)	132
-trans-				
N1-H1n···O4	0.85(8)	1.93(8)	2.769(6)	171(8)
O4-H4s···O2	0.84(10)	2.13(9)	2.897(6)	152(7)
C2-H2···O1	0.95	2.51	3.182(7)	128
C4-H4···O1	1.00	2.26	3.161(6)	149
C20-H20b···O3	0.98	2.51	3.409(7)	152

Table 3.9. Geometries of weak hydrogen-bonding interactions in α- and β-*trans*-**1**·2MeOH at 100 K.

As described earlier, the triflate ions are anchored to the dications via the interaction of O2 with the methanol solvate (O4-H4s···O2) and the 5-pyrazolyl hydrogen (C1-H1···O2), shown again in the top of Figure 3.8. Another oxygen of the same triflate, O1, interacts with the methine hydrogen H4 (C4-H4···O1 2.34 Å; C4 ···O1, 3.791(2) Å) to give a polymer along the *b*- direction. The interaction between the final oxygen of the

triflate O3 and a methyl hydrogen of a pz* group (C14-H14b···O3, 2.48 Å; C14 ···O3, 3.374(2) Å) forms a sheet in the (-2 0 4) plane. As shown in Figures 3.8b and 3.8c, the sheets are stacked in the third dimension by two C-H···O interactions. That is, O2 of the triflate in one sheet interacts with a methyl hydrogen of a pz* group in an adjacent sheet (C10-H10c···O2, 2.53 Å; C14 ···O3, 3.410(2) Å) while triflate O3 of one sheet interacts with the 4-(ring) hydrogen of a pz* group on a neighboring sheet (C12-H12···O3, 2.60 Å; C14 ···O3, 3.414(2) Å). The other two interactions in Table 3.9 serve to further bolster the structure, but are not shown for clarity.

In β-*trans*-**1**·2MeOH, sheets in the (-2 0 4) plane are formed by weak charge-assisted hydrogen bonding interactions involving only two of the three triflate oxygen atoms, O1 and O2; the third oxygen, O3, is used to stack sheets. That is, as shown in the right of Figure 3.7 and in Figure 3.9, the triflate ion is indirectly anchored to the dication by a single hydrogen bonding interaction with the methanol hydrogen (O4-H4s···O2). This orients O1 of the triflate to interact with both the methine hydrogen, H4, and the proximal 4-hydrogen, H2, of the confused pyrazolyl on a neighboring dication. Then, connectivity in the third dimension is established by the triflate O3 of one sheet interacting with a methyl hydrogen of the pz* group on a neighboring sheet, Figures 3.9b and 3.9c.

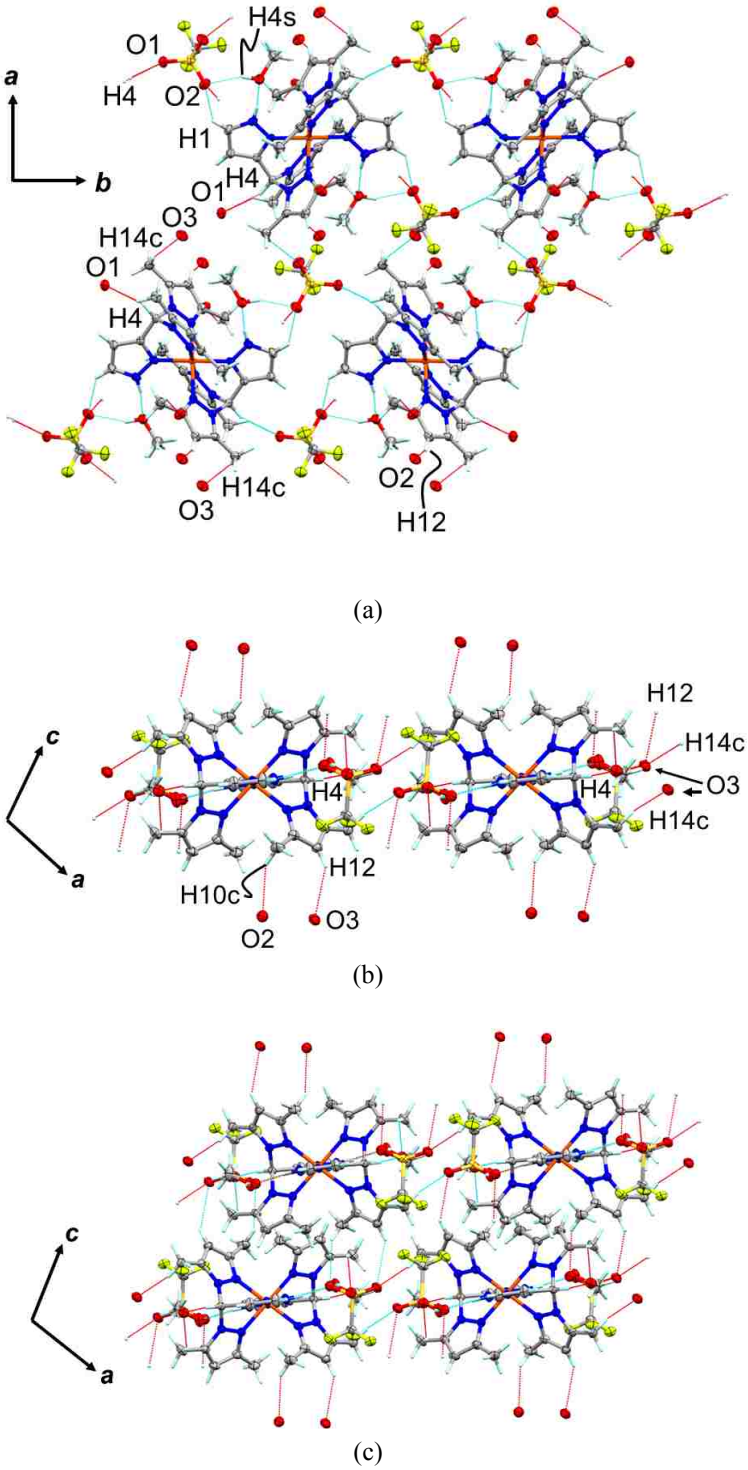

Figure 3.8. Supramolecular structure of α-*trans*-**1**·2MeOH at 100 K. (a) View down *c*- of the sheet in the (-2 0 4) plane; (b) View down *b* of sheet; (c) stacking of sheets. Red dashed lines: Hanging contacts. Cyan dashed lined completed contacts.

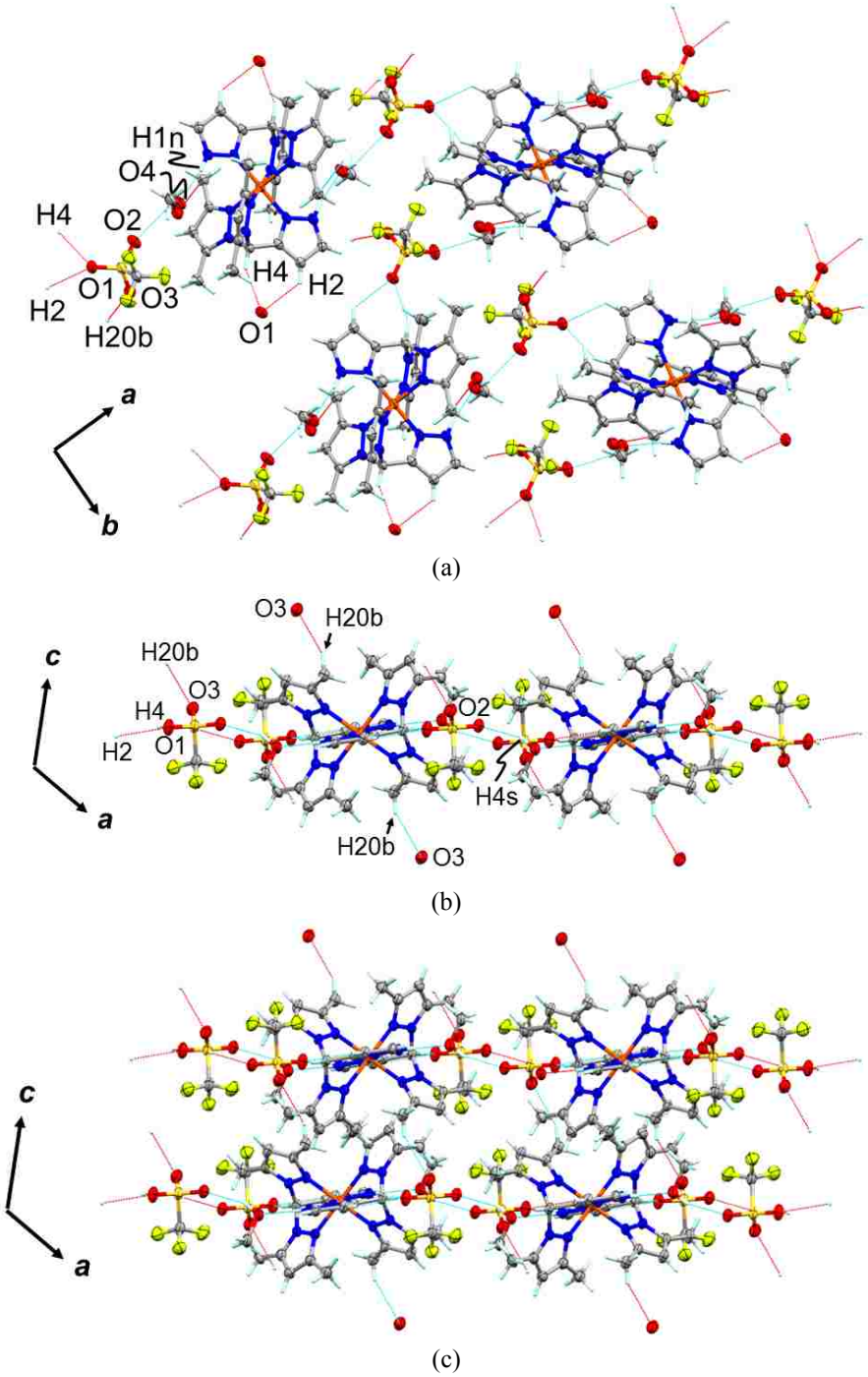

Figure 3.9. Supramolecular structure of β-*trans*-**1**·2MeOH at 100 K. (a) View down *c*- of the sheet in the (-2 0 4) plane; (b) View down *b* of sheet; (c) stacking of sheets. Red dashed lines: Hanging contacts. Cyan dashed lined completed contacts.

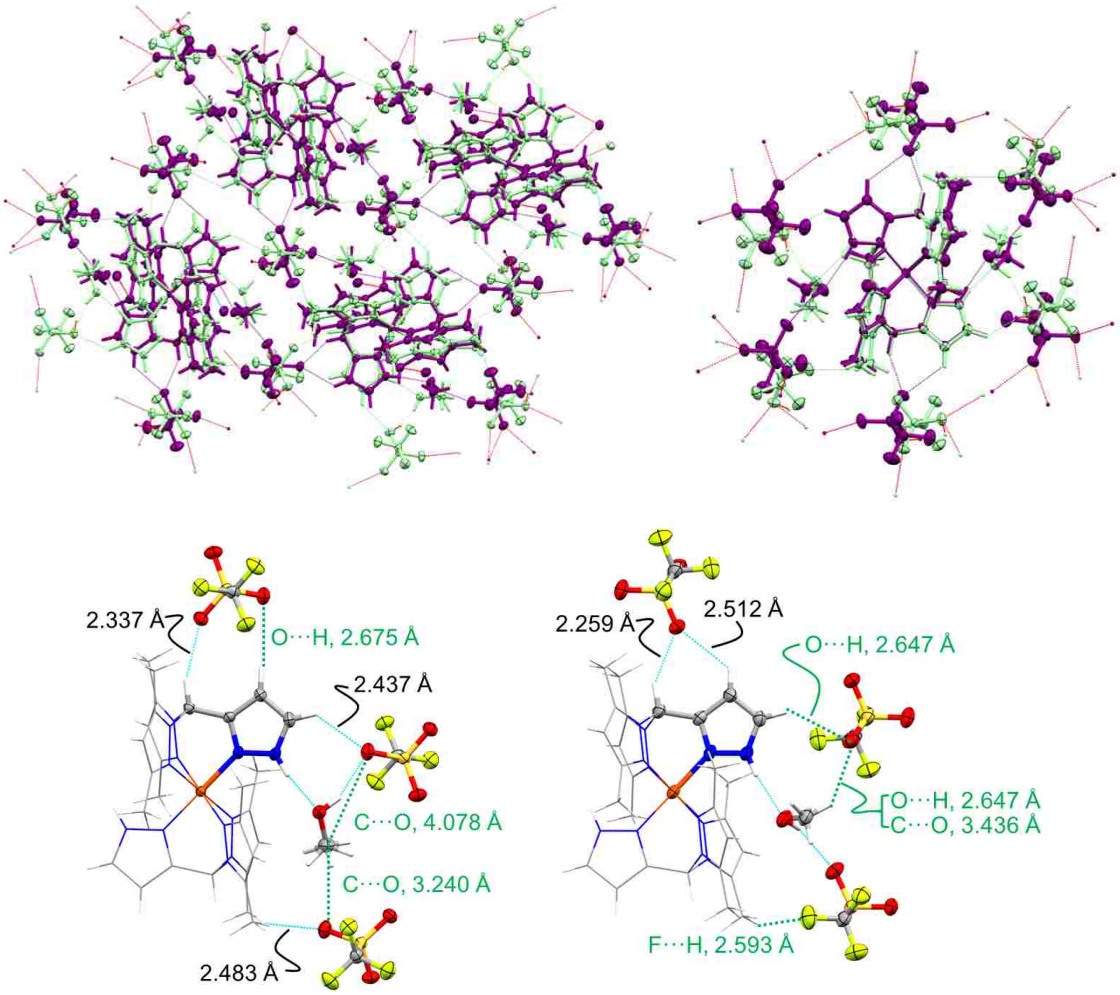

Figure 3.10. Overlays of four complexes and associated ions and methanol solvate molecules in the 100 K structures of α- (green) and β- (violet) *trans*-**1**·2MeOH. Top left: Overlay constructed by minimizing differences between four iron atoms in the (-2 0 4) plane of each structure. Top right: Overlay of FeN_6 cores of one complex (and associated triflate ions and methanol solvate molecules) in each polymorph. Green dashed lines completed contacts of the α- form, violet dashed lines are completed contacts for β- form, and red dashed lines hanging contacts. Bottom left: View of the α- form with selected distances highlighted. Bottom Right: View of β- form with distances shown.

Figure 3.10 overlays the 100 K structures of α- and β-*trans*-**1**·2MeOH in two ways in an attempt to clarify their differences. When the structures are overlaid by either matching as closely as possible four iron atoms in the (-2 0 4) plane of each structure (Figure 3.10, top left) or by minimizing FeN_6 kernels of one cation in each polymorph

(Figure 3.10, top right), the triflate anions and methanol solvate molecules differ subtly in their positions and orientations. In the α-form, the triflate nearest to the methine hydrogen is oriented such that a second oxygen of the triflate is closest to the 4- pyrazolyl ring hydrogen (2.675 Å), see bottom left Fig. 3.10. Also, the triflate oxygen involved in the C-H···O interaction with a methyl hydrogen of a pz* group is positioned near to the methanol methyl group (C···O, 3.240 Å). In the denser β-form with less distorted scorpionate ligands, the methanol solvate re-orients to give a C6O4-N1C1 torsion angle of 130.3^{o} (the alpha torsion angle was 58.3). This reorientation liberates the triflate originally near the confused pyrazolyl from any strong intermolecular interactions such that the shortest contacts to the triflate O3 are with H1 and, now, the methyl hydrogen of the solvate H6c, both at 2.647 Å (bottom right Fig. 3.10). The methanol now hydrogen bonds to the triflate originally near the pz* methyl. This triflate has reoriented such that the closest contact to the pyrazolyl methyl is between F3 and H14c at 2.593 Å. Also the triflate near the methine has reoriented to have O1 chelated by the methine hydrogen and the ring hydrogen H1, as outlined earlier. Thus, while the hydrogen bonding pattern between the methanol solvate and triflate changes significantly, the overall positions of the triflate anions does not. It is of interest to note that the nickel(II) complex, *trans*-[Ni(^{H}L*)$_2$](OTf)$_2$·2MeOH, *trans*-**2**·2MeOH, is isomorphous with α-*trans*-**1**·2MeOH but the former does not undergo a crystallographic phase change even under prolonged standing at 100 K; *the electronic spin crossover in the iron(II) complex likely causes the phase change*. Also, the *cis*-**2** stucture is different than the iron(II) core, suggesting another polymorph of iron might exist.

The phase change in *trans*-**1**·2MeOH was also monitored by variable temperature powder X-ray diffraction. Figure 3.11 shows the calculated diffraction patterns (dotted lines) from single crystal X-ray diffraction experiments of α-*trans*-**1**·2MeOH at 150 K (Fig 3.11a), β-*trans*-**1**·2MeOH at 100 K (Fig 11e), and *cis*-1 at 100 K (Fig 3.11f). Experimental patterns for crushed, hand-separated crystals of α-*trans*-**1**·2MeOH are shown by the solid lines in Figures 3.11b-3.11d. At 150 K, there is excellent agreement between experimental and calculated patterns for α-*trans*-**1**·2MeOH showing that, although the separation from *cis*-**1** was very good (but not perfect), peaks for *cis*-**1** (notably at $2\theta = 8.4$ and 17.7^{o}) are not readily detectable. Upon further cooling, the sample changes appearance from translucent purple to opaque pink, as the crystals shatter, beginning at 130 K (right of Fig. 3.11). Concomitantly, peaks for β-*trans*-**1**·2MeOH appear and begin growing in intensity at the expense of those for the α- form. Figure 3.11c shows the diffractogram for a sample at 120 K with peaks for both the -form (notably at $2\theta = 9.5^{o}$, 11.3^{o}, and 16.9^{o}) and the β-form (notably at $2\theta = 9.9^{o}$, 10.8^{o}, and 14.0^{o}) respectively. The transformation between α- and β- forms is quite slow. Even after sitting 1.5 hr at 100 K (Fig 3.11d), the transformation is mostly complete but peaks for the α- form are still detectable. The transformation is reversible, but sluggish at low temperature. That is, on rewarming from 100 K to 150 K and sitting 40 min, a significant amount of the β-form remains. Upon further warming to 295 K for 5 min, re-cooling to

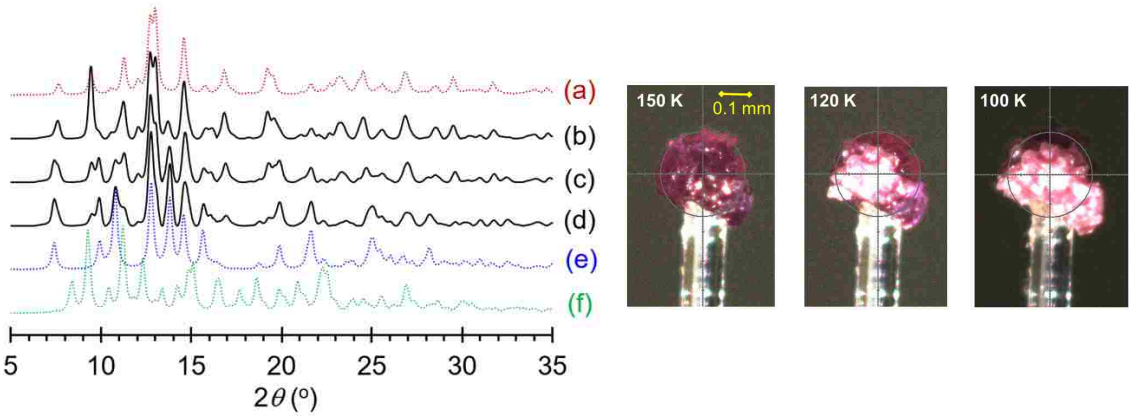

Figure 3.11. Left: Overlay of calculated or experimental powder X-ray diffraction patterns for **1**·2MeOH at various conditions and the calculated pattern for *cis*-**1**. Key: (a) α-*trans*-**1**·2MeOH at 150 K, calculated from single crystal structure; (b) α-*trans*-**1**·2MeOH powder at 150 K; (c) α-*trans*-**1**·2MeOH powder at 120 K; (d) original α-*trans*-**1**·2MeOH powder at 100 K (now converted to the β- form); (e) β-*trans*-**1**·2MeOH at 100 K, calculated from single crystal structure; (f) *cis*-**1** at 100 K, calculated from single crystal structure. Right: Photographs of powder during data collection.

150 K and sitting 10 min, peaks for the β-form are no longer observed; the original 150 K diffractogram for the α-form is regenerated only with subtle changes in the intensity of peaks.

The magnetic properties of hand-separated, air-dried crystals of *co*-**1**, *cis*-**1**, and α-*trans*-**1**·H_2O were investigated by SQUID magnetometry. Figure 3.12 gives the magnetic data, plotted as $\chi_m T$ versus T. The magnetic data for *co*-**1** shows a

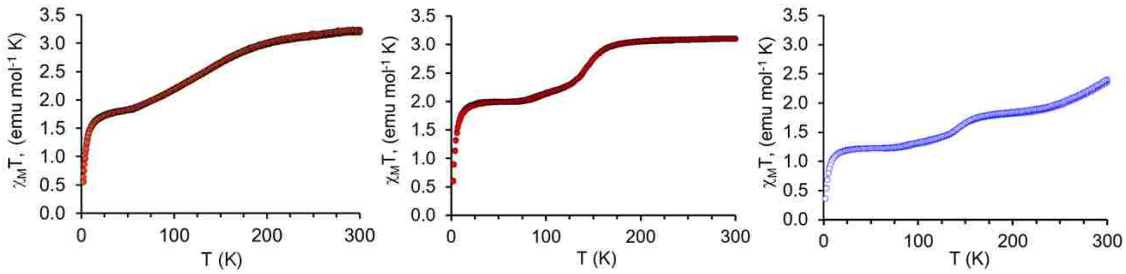

(a) (b) (c)

Figure 3.12. Magnetic susceptibility data obtained from (a) *co*-**1**; (b) hand-separated crystals of *cis*-**1**; (c) hand-separated, air-dried crystals of sample that analyzed as "*trans*-**1**·H_2O".

gradual SCO beginning near 300 K that stops after reaching 50% completion at 55 K. This behavior is aligned with the crystallographic data that showed only the cis-component undergoes SCO. In *cis*-**1**, $\chi_m T$ maintains a constant value between 300 K to about 165 K of 3.2 cm^3Kmol^{-1} consistent with 100% HS Fe(II). Between 80 to 20 K, $\chi_m T$ value drops to a constant value of 2.0 cm^3Kmol^{-1}, indicating about 63% HS Fe(II). Given the X-ray structural data that showed a rather long average Fe-N bond distance (2.11(2) Å) at 100 K consistent with an incomplete crossover and a triflate disordered in a near 2:1 ratio over two sites, we tentatively ascribe the unusual magnetic behavior of the crystals to be the result of the spin crossover of the minor disorder component in the crystals of *cis*-**1**; the majority of the sample remains HS. The subtle "hump" in the curve near 100 K is probably due to incomplete mechanical separation from a small portion of *co*-**1** contaminant. The magnetic properties of the air-dried, hand-separated, violet crystals, initially of α-*trans*-1·2MeOH that analyzed as "*trans*-**1**·H_2O" after drying, are higher than expected for a LS Fe(II) species, with the $\chi_m T$ value dropping from 2.4 cm^3Kmol^{-1} at 300 K to a constant value of 1.2 cm^3Kmol^{-1} at 60 K. Further, as illustrated in Figure 3.12c, the $\chi_m T$ vs T plot contains features in the 165 to 80 K region and near 100 K reminiscent of *cis*-**1** and *co*-**1**. So, despite the care taken during separation, the sample of "*trans*-**1**·H_2O" is a mixture, presumably formed during methanol desolvation and hydration. Given the values of $\chi_m T$ at low temperature and the elemental analysis results, the mixture could be 50% *trans*-**1**·$2H_2O$ and 50% *cis*-**1** or some combination of (100/x)% *trans*-**1**·xH_2O (x > 2), and 100(1-1/x) % unevenly divided between *cis*-**1** and

co-**1**. The presumptive species *trans*-**1**·$2H_2O$ is likely diamagnetic until about 250 K and then begins to undergo SCO on warming further to room temperature as indicated from the increase in $\chi_M T$ versus that in *cis*-**1**. Unfortunately, we have thus far been unable to isolate an authentic sample of *trans*-**1**·$2H_2O$ because, surprisingly, only the *cis*-**1** has been recovered from aqueous solutions.

3.4 CONCLUSIONS

A new iron(II) N-confused C-scorpionate complex, $[Fe(^{H}L^*)_2](OTf)_2$, **1**, was prepared in high yield, and the crystallization and magnetic properties of its polymorphs and solvatomorphs have been described in detail. This was the first attempt to control the $T_{1/2}$ of SCO in N-confused tris(pyrazolyl)methane derivatives by increasing the steric properties of the scorpionate ligand. It was confirmed that by substituting the normal pyrazolyls with 3,5-dimethylpyrazolyls in the ligand, $^{H}L^*$, the $T_{1/2}$ would lower due to the steric interactions between methyls (that would favor elongated Fe-N bond lengths, and subsequently, the HS state). This chapter discussed the structural changes and hydrogen bonding interactions that were attributed to unexpected differences in magnetic behavior between different solid-state structures and solvates.

The Fe-N bond lengths of the 1:1 co-crystal of *cis*-**1**:*trans*-1, *co*-**1** at 100 K and 250 K established that the *trans*- isomer component remained HS, while the *cis*-isomer was intermediately between HS and LS. The *trans*- component was more disordered due to a greater degree of pyrazolyl ring twisting and ring tilting at 100 K and 250 K, and a disordered triflate anion. From crystallographic data, it was expected that the least distorted HS complex with shorter Fe-N bonds would undergo SCO first upon cooling.

The magnetic behavior of *co*-**1** confirmed that only the cis-component underwent SCO, with a gradual SCO beginning near 300 K that stopped at 50% completeness at 55 K. Similarly, the three-dimensional structure of hand-separated *cis*-**1** crystals contained a disordered triflate anion disordered in a 2:1 ratio over two positions, attributed to an unusual SCO at 63% completeness between 80K-20K. The *trans*- compounds analyzed at 100 K and 250 K demonstrated how slight modifications in the placement of solvate and anions impact the hydrogen bonding interactions, undergoing a phase transition at 100 K likely caused by SCO.

As expected, the $T_{1/2}$ of SCO of $[Fe(^{H}L^{*})_2](OTf)_2$ was lowered from that of the parent complex discussed in chapter two, which began at ca. 330 K and reached ca. 95% completion at 400 K. However, its magnetic behavior was more gradual, and revealed complex mixtures of polymorphs. The SCO behavior was ultimately influenced by more than sterics, as this chapter demonstrated. The position of the triflate anion and solvate (and their subsequent hydrogen bonding interactions), crucial to the organization of the crystal lattice, resulted in differing magnetic properties that could be rationalized by a detailed analysis of the solid-state structures.

Chapter 4

FUTURE WORK

The purpose of this thesis was to examine whether hydrogen bonding interactions can be used to assemble iron(II) scorpionate complexes and whether this leads to abruptness in the SCO behavior. To examine these interactions, two new N-confused C-scorpionates, ^{Ts}L* and ^{H}L*, each with two 'normal' 3,5-dimethylpyrazolyl groups, and either an N-tosyl or N-H group on the 'confused' pz, were prepared in high yield. These compounds were prepared alongside the previously reported, less bulky ^{Ts}L and ^{H}L derivatives, and their syntheses and reactivities were compared.

Future work would involve a comprehensive study of iron(II) N-confused C-scorpionate complexes of varied counter-ions. Following the procedure described in this work, new iron(II) scorpionate complexes would be synthesized in a direct reaction of ^{H}L or ^{H}L*, with an iron(II) salt (i.e. $Fe(OTf)_2$, $Fe(BF_4)_2$, $FeCl_2$, $Fe(OTs)_2$ or $FeSO_4$). The counter-ion would expectedly influence the hydrogen bonding interactions in the solid state, as noted in $[Fe(^{H}L)_2](OTf)_2$ and $[Fe(^{H}L)_2](BF_4)_2$. The impact of counter-ion size and electronics on SCO would be studied by analyzing all the subsequent hydrogen bonding interactions (solvent, ligand, and counter-ion) in the solid-state. This work would also provide insight into how the subsequent crystal packing is influenced by the diverse steric profiles of ^{H}L and ^{H}L*, as noted in $[Fe(^{H}L)_2](OTf)_2$ and $[Fe(^{H}L^*)_2](OTf)_2$.

In addition, it could be envisioned that a strong hydrogen bonding acceptor, such as 4-4' bipyridine, could be crystallized in a 1:1 ratio with the desired SCO complex to direct the solid-state assemblies, and yield a highly cooperative system. As described in

this work, SCO behavior is further complicated by solvation, as noted in SCO behavior of $[Fe(^{H}L^{*})_2](OTf)_2$ polymorphs. To further investigate crystal packing, SCO of several polymorphs would be studied.

BIBLIOGRAPHY

1. Brooker, S. *Chem. Soc. Rev.* **2015**, *44*, 2880-2892.

2. Shriver, D.; Weller, M. T.; Overton, T. L.; Rourke, J. P.; Armstrong, F. A. *Inorganic Chemistry*, 6 ed., W.H. Freeman and Company, Ltd, New York, 2014.

3. Kahn, O.; Martinez, C. J. *Science* **1998**, *279*, 44-48.

4. Kahn, O. *Chem. Br.* **1999**, *2*, 24-27.

5. Sorai, M.; Nakazawa, Y.; Nakano, M; Miyazaki, Y. *Chem. Rev.* **2013**, *113*, PR41-PR122; Sorai, M. *Top. Curr. Chem.* **2004**, *235*, 153-170.

6. Halcrow, M. A. *Chem. Soc. Rev.* **2011**, *40*, 4119-4142.

7. Halcrow, M. A. *Spin-Crossover Materials: Properties and Applications*, John Wiley & Sons, Ltd, 2013.

8. Sugahara, A.; Kamebuchi, H.; Okazawa, A.; Enomoto, M; Kojima, N. *Inorganics* **2017**, *5*, 1-23.

9. Long, G. J.; Grandjean, F; Reger, D. L. *Top. Curr. Chem.* **2004**, *233*, 91.

10. Jesson, J. P.; Trofimenko S.; Eaton, D. R. *J. Am. Chem. Soc.* **1967**, *89*, 3158–3167.

11. Grandjean, F.; Long, G. J.; Hutchinson, B. B.; Ohlhausen, L.; Neill, P.; Holcomb, J. D. *Inorg. Chem.* **1989**, *28*, 4406-4414.

12. Salmon, L.; Molnár, G.; Cobo, S.; Oulié, P.; Etienne, M.; Mahfoud, T.; Demont, P.; Eguchi, A.; Watanabe, H.; Tanaka, K; Bousseksou, A. *New. J. Chem.* **2009**, *33*, 1283-1289.

13. Reger, D. L.; Little, C. A.; Smith, M. D.; Rheingold, A. L.; Lam, K. C.; Concolino, T. L.; Long G. J.; Hermann, R. P; Grandjean, F. *Eur. J. Inorg. Chem.* **2002**, 1190-1197.

14. Reger, D. L.; Little, C. A.; Rheingold, A. L.; Lam, M.; Concolino, T.; Mohan, A.; Long, G. J. *Inorg. Chem.* **2000**, *39*, 4674-4675.

15. (a) Reger, D. L.; Little, C. A.; Rheingold, A. L.; Lam, M.; Liable-Sands, L. M.; Rhagitan, B.; Concolino, T.; Mohan, A.; Long, G. J.; Briois, V.; Grandjean, F. *Inorg. Chem.* **2001**, *40*, 1508-1520; (b) Reger, D. L.; Little, C. A.; Young Jr., V. G.; Pink, M. *Inorg. Chem.* **2001**, *40*, 2870-2874.

16. Reger, D. L.; Gardinier, J. R.; Elgin, J. D.; Smith, M. D.; Hautot, D.; Long, G. J.; Grandjean, F. *Inorg. Chem*. **2006**, *45*, 8862-8875.

17. Moubaraki, B.; Leita, B. A.; Halder, G. J.; Batten, S. R.; Jensen, P.; Smith, J. P.; Cashion, J. D.; Kepert, C. J.; Létard, J. F.; Murray, K. S. *Dalton Trans.* **2007**, 4413–4426.

18. Goodman, M. A.; Nazarenko, A. Y.; Casavant, B. J.; Li, Z.; Brennessel, W. W.; DeMarco, M. J.; Long, G.; Goodman, M. S. *Inorg. Chem.* **2012**, *51*, 1084−1093.

19. Gardinier, J. R.; Treleven, A. R.; Meise, K. J.; Lindeman, S. V. *Dalton Trans*. **2016**, *45*, 12639-12643.

20. (a) Trofimenko, S. *Scorpionates: The Coordination Chemistry of Polypyrazolylborate Ligands*, Imperial Press, London, 1999. (b) Pettinari, C. *Scorpionates II: Chelating Borate Ligands*, Imperial Press, London, 2008.

21. Spicer, M. D.; Reglinski, J. *Eur. J. Inorg. Chem.* **2009**, *12*, 1553-1574.

22. (a) Akorta, I.; Claramunt, R. M.; Díez-Barra, E.; Elguero, J.; de la Hoz, A.; Lopez, C. *Coord. Chem. Rev.* **2017**, *339*, 153-182. (b) Pettinari, C.; Pettinari, R. *Coord. Chem. Rev*. **2005**, 249, 525-543. (c) Bigmore, H. R.; Lawrence, S. C.; Mountford, P. Tredget, C. S. *Dalton Trans.*, **2005**, 635–651. (d) Reger, D. L. *Comments Inorg. Chem.* **1999**, *21*, 1-28.

23. (a) Kläui, W.; Berghahn, M.; Rheinwald, G.; Lang, H. *Angew. Chem., Int. Ed.* **2000**, *39*, 2464−2466. (b) Kläui, W.; Schramm, D.; Peters, W.; Rheinwald, G.; Lang, H. *Eur. J. Inorg. Chem.* **2001**, 1415−1424. (c) Kläui, W.; Berghahn, M.; Frank, W.; Reiβ, G. J.; Schönherr, T.; Rheinwald, G.; Lang, H. *Eur. J. Inorg. Chem.* **2003**, 2059−2070. (d) Papish E. T.; Taylor, M. T; Jernigan, F. E., 3rd; Rodig, M. J; Shawhan, R. R; Yap, G. P. A.; Jove, F. A. *Inorg. Chem.* **2006**, *45*, 2242-2250.

24. Pettinari, C.; Cingolani, A.; Lobbia, G. G.; Marchetti, F.; Martini, D.; Pellei, M.; Pettinari, R.; Santini, C. *Polyhedron* **2004**, 451-469.

25. (a) Ana Caballero, M. Mar Díaz-Requejo, Manuel R. Fructos, Juan Urbano and Pedro J. Pérez "Modern Applications of Trispyrazolylborate Ligands in Coinage Metal Catalysis" in *Ligand Design in Metal Chemistry: Reactivity and Catalysis*: (eds M. Stradiotto and R. J. Lundgren), John Wiley & Sons, Ltd, Chichester, UK, **2016**, 308-329. Doi: 10.1002/9781118839621.ch11. (b) Caballero, A.; Perez, P. *J. Organomet. Chem.* **2015**, *793*, 108-113. (c) Diaz-Requejo, M. M.; Perez, P. J. *Chem. Rev.* **2008**, *108*, 3379-3394. (e) Diaz-Requejo, M. M.; Perez, P. J. *J. Organomet. Chem.* **2005**, *690*, 5441-5450.

26. Dias, H. V. R.; Browning, R. G.; Polach, S. A.; Diyabalanage, H. V. K.; Lovely, C. J. *J. Am. Chem. Soc.* **2003**, 125, 9270–9271.

27. Lovely, C. J.; Browning, R. G.; Badarinarayana, V.; Dias, H. V. R. *Tetrahedron Lett.* **2005**, 46, 2453-2455.

28. Dias, H. V. R.; Browning, R. G.; Richey, S. A.; Lovely, C. J. *Organometallics* **2004**, *23*, 1200-1202.

29. (a) Alvarez, M.; Gava, R.; Rodriguez, M. R.; Rull, S. G.; Perez, P. J. *ACS Catal.*, **2017**, 7, 3707–3711. (b) Caballero, A.; Despagnet-Ayoub, E.; Mar Diaz-Requejo, M.; Diaz-Rodriguez, A.; Gonzalez-Nunez, M. E.; Mello, R.; Munoz, B. K.; Ojo, W.-S.; Asensio, G.; Etienne, M.; Perez, P. J. *Science* **2011**, *332*, 835-838. (c) Despagnet-Ayoub, E.; Jacob, K.; Vendier, L.; Etienne, M.; Alvarez, E.; Caballero, A.; Diaz-Requejo, M. M.; Perez, P. J. *Organometallics* **2008**, *27*, 4779-4787. (d) Gomez-Emeterio, B. P.; Urbano, J.; Diaz-Requejo, M. M.; Perez, P. J. *Organometallics* **2008**, *27*, 4126-4130. (e) Braga, A. A. C.; Maseras, F.; Urbano, J.; Caballero, A.; Mar Diaz-Requejo, M.; Perez, P. J. *Organometallics* **2006**, *25*, 5292-5300. (f) Urbano, J.; Belderrain, T. R.; Nicasio, M. C.; Trofimenko, S.; Diaz-Requejo, M. M.; Perez, P. J. *Organometallics* **2005**, *24*, 1528-1532.

30. Iglesias, M. J.; Nicasio, M. C.; Caballero, A.; Perez, P. J. *Dalton Trans.* **2013**, *42*, 1191-1195.

31. Urbano, J.; Braga, A. A. C.; Maseras, F.; Alvarez, E.; Diaz-Requejo, M. M.; Perez, P. J. *Organometallics* **2009**, *28*, 5968-5981.

32. Rivilla, I.; Sameera, W. M. C.; Alvarez, E.; Diaz-Requejo, M. M.; Maseras, F.; Perez, P. J. *Dalton Trans.* **2013**, *42*, 4132-4138.

33. Maestre, L.; Sameera, W. M. C.; Díaz-Requejo, M. M.; Maseras, F.; Pérez, P. J. *J. Am. Chem. Soc.* **2013**, *135*, 1338–1348.

34. Llaveria, J.; Beltran, A.; Diaz-Requejo, M. M.; Matheu, M. I.; Castillon, S.; Perez, P. J. *Angew. Chem., Int. Ed.* **2010**, *49*, 7092-7095.

35. Beltrán, A.; Lescot, C.; Díaz-Requejo, M. M.; Pérez, P. J.; Dauban, P. *Tetrahedron* **2013**, 69, 4488-4492.

36. Maestre, L.; Dorel, R.; Pablo, Ó.; Escofet, I.; Sameera, W. M. C.; Álvarez, E.; Maseras, F.; Díaz-Requejo, M. M.; Echavarren, A. M.; Pérez, P. J. *J. Am. Chem. Soc.* **2017**, 139, 2216-2223.

37. Lam, T. L.; Tso, K. C. –H.; Cao, B.; Yang, C.; Chen, D.; Chang, X. –Y.; Huang, J. –S.; Che, C. –M. *Inorg. Chem.* **2017**, *56*, 4253-4257.

38. Arenas, I.; Ángeles Fuentes, M.; Álvarez, E.; Díaz, Y.; Caballero, A.; Castillón, S.; Pérez, P. J. *Inorg. Chem.* **2014**, *53*, 3991-3999.

39. (a) Smolenski, P.; Pettinari, C.; Marchetti, F.; Guedes da Silva, M Fatima C; Lupidi, G.; Badillo Patzmay, G. V.; Petrelli, D.; Vitali, L. A; Pombeiro, A. J. L. *Inorg. Chem.* **2015**, *54*, 434–440. (b) Pettinari, C.; Marchetti, F.; Lupidi, G.; Quassinti, L.; Bramucci, M.; Petrelli, D.; Vitali, L. A.; Guedes da Silva, M. F. C.; Martins, L. M. D. R. S.; Smolenski, P.; Pombiero, A. J. L. *Inorg. Chem.* **2011**, *50*, 11173-11183.

40. Cingolani, A.; Effendy; Martini, D.; Pellei, M.; Pettinari, C.; Skelton, B. W.; White, A. H. *Inorg. Chim. Acta* **2002**, *328*, 87-95.

41. (a) Reger, D. L.; Collins, J. E.; Rheingold, A. L.; Liable-Sands, L. M.; Yap, G. P. A. *Organometallics* **1997**, *16*, 349-353. (b) Reger, D. L.; Semeniuc, R. F.; Smith, M. D. *Eur. J. Inorg. Chem.* **2003**, 3480-3494. (c) Semeniuc, R. F.; Reger, D. L. *Eur. J. Inorg. Chem.* **2016**, 2253-2271.

42. Hückel, W.; Bretschneider, H. *Chem. Ber.* **1937**, *70*, 2024-2026.

43. Julia, S.; del Mazo, J.; Avila, L.; Elguero, J. *Org. Prep. Proc. Int.* **1984**,*16*, 299-307.

44. Reger, D. L.; Grattan, T. C.; Brown, K. J.; Little, C. A.; Lamba, J. J. S.; Rheingold, A. L.; Sommer, R. D. *J. Organomet. Chem.* **2000**, *607*, 120-128.

45. Li, Z; Capretto, D. A.; He, C. *Prog. Inorg. Chem.* **2009**, *56*, 1-48. (b) Li, Z.; Capretto, D. A.; Rahaman, R.; He, C. *Angew. Chem. Int. Ed.* **2007**, *46*, 5184-5186. (c) Li, Z.; He, C. *Eur. J. Org. Chem.* **2006**, 4313-4322. (d) Cui, Y.; He, C. *Angew. Chem. Int. Ed.* **2004**, *43*, 4210-4212. (e) Cui, Y.; He, C. *J. Am. Chem. Soc.* **2003**, *125*, 16202-16203.

46. (a) Yang, M.; Su, B.; Wang, Y.; Chen, K.; Jiang, X.; Zhang, Y. –F.; Zhang, X. –S.; Chen, G.; Cheng, Y.; Cao, Z.; Guo, Q. –Y.; Wang, L.; Shi, Z. –J. *Nat. Commun*. ***2014***, *5:4707*, 1-6. (b) Zhang, X. *J. Organomet. Chem.* **2017**, *832*, 1-8.

47. (a) Corbin, J. R.; Schomaker, J. M. *Chem. Commun.* **2017**, *53*, 4346-4349. (b) Alderson, J. M.; Corbin, J. R.; Schomaker, J. M. *Acc. Chem. Res.* **2017**, *50*, 2147-2158. (c) Weatherly, C. D.; Alderson, J. M.; Berry, J. F.; Hein, J.; Schomaker, J. M. *Organometallics* **2017**, *36*, 1649– 1661. (d) Huang, M.; Corbin, J. R.; Dolan, N. S.; Fry, C. G.; Vinokur, A. A.; Guzei, I. A.; Schomaker, J. M. *Inorg. Chem.* **2017**, *56*, 6725-6733. (e) Shomaker Dolan, N. S.; Scamp, R. J.; Yang, T.; Berry, J. F.; Schomaker, J. M. *J. Am. Chem. Soc.* **2016**, *138*, 14658– 14667. (f) Scamp, R. J.; Jirak, J. G.; Dolan, N. S.; Guzei, I. A.; Schomaker, J. M. *Org. Lett.* **2016**, *18*, 3014-3017. (g) Rigoli, J. W.; Weatherly, C. D.; Alderson, J. M.; Vo, B. T.; Schomaker, J. M. *J. Am. Chem. Soc.* **2013**, *135*, 17238-17241.

48. (a) Martins, L. M. D. R. S. *Catalysts*, **2017**, *7*, 12; doi:10.3390/catal7010012. (b) Wathier, M.; Love, J. A. *Eur. J. Inorg. Chem.* **2016**, 2391-2402.

49. Liang, S.; Jensen, M. P. *Organometallics* **2012**, *31*, 8055-8088.

50. Gardinier, J. R.; Treleven, A. R.; Meise, K. J.; Lindeman, S. V. *Dalton Trans.* **2016**, *45*, 12639-12643.

51. Carrión, M. C.; Jalon, F. A.; Manzano, B. R.; Rodríguez, A. M.; Sepúlveda, F.; Maestro, M. *Eur. J. Inorg. Chem.* **2007**, 3961–3973.

52. (a) Evans, D. F. *J. Chem. Soc.* **1959**, 2003–2005; (b) Evans, D. F.; Fazakerley, G. V.; Phillips, R. F. *J. Chem. Soc. A* **1971**, 1931–1934. (c) Piguet, C. *J. Chem. Ed.* **1997**, *74*, 815-816.

53. Morrison, G.; zur Loye, H.-C. *J. Solid State Chem.* **2015**, 221, 334–337.

54. Bain, G. A.; Berry, J. F. *J. Chem. Ed.* **2008**, *85*, 532-536.

55. Ozawa, T.; Kurahashi, T.; Matsubara, S. *Synlett,* **2013**, 24 2763-2767

56. CrysAlisPro, Agilent Technologies, Version 1.171.34.46 (release 25-11-2010 CrysAlis171.NET), (compiled Nov 25 2010,17:55:46).

57. O. V. Dolomanov, L. J. Bourhis, R. J. Gildea, J. A. K. Howard and H. Puschmann. *J. Appl. Cryst.* **2009**, *42*, 339-341.

58. Sheldrick, G. M. SHELXTL Version 6.12; Bruker Analytical X-ray Systems, Inc., Madison Wisconsin, USA, 2001.

59. (a) The, K.I.; Peterson, L.K. *Can. J. Chem.* **1973**, *51*, 422-426. (b) The, K.I.; Peterson, L.K.; Kiehlmann, E. *Can. J. Chem.* **1973**, *51*, 2448-2451. (c) Peterson, L.K.; Kiehlmann, E.; Sanger, A.R.; The, K.I. *Can J. Chem.* **1974**, *52*, 2367-2374.

60. Gowda, B. T.; Jyothi, K.; D'Souza, J. D. *Z. Naturforsch., Tiel A* **2002**, *57a*, 967-973.

61. Liddle, B. J.; Hall, D.; Lindeman, S. V.; Smith, M. D.; Gardinier, J. R. *Inorg. Chem.* **2009**, *48*, 8404−8414.

62. Reger, D. L.; Semeniuc, R. F.; Little, C. A.; Smith, M. D. *Inorg. Chem.* **2006**, *45*,7758–7769.

63. Carranza, M. P.; Manzano, B. R.; Jalón, F.; Rodriguez, A. M.; Santos, L.; Moreno, M. *New. J. Chem.* **2013**, *37*, 3183-3194.

64. Wen, M.; Munakata, M.; Suenaga, Y.; Kuroda-Sowa, T.; Maekawa, M.; Kodai, I. *Polyhedron* **2004**, *23*, 2117-2123.

65. Reineke, M. H.; Sampson, M. D.; Rheingold, A. L.; Kubiak, C. P. *Inorg. Chem*. **2015**, *54*, 3211-3217.

66. Gardinier, J. R.; Hewage, J. S.; Lindeman, S. V. *Inorg. Chem.* **2014**, *53*, 12108–12121.

67. Davis, T. L.; Watts, J. L.; Brown, K. J.; Hewage, J. S.; Treleven, A. R.; Lindeman S. V.; Gardinier, J. R. *Dalton Trans*. **2015**, 44, 15408-15412.

68. (a) Casarin, M.; Forrer, D.; Carau, F.; Pandolfo, L.; Pettinari, C.; Vittadini, A. *Inorg. Chim. Acta* **2009**, *362*, 4358-4364. (b) Casarin, M.; Forrer, D.; Carau, F.; Pandolfo, L.; Pettinari, C.; Vittadini, A. *J. Phys. Chem. A.* **2008**, 112, 6723-6731.

69. (a) Grochala, W.; Cyranski, M. K.; Derzsi, M.; Michalowski, T.; Malinowski, P. J.; Mazej, Z.; Kurzydlowski, D.; Kozminski, W.; Budziankowski, A.; Leszczynski, P. J. *Dalton Trans.* **2012**, *41,* 2034-2047. (b) Johnston, D. H.; Shriver, D. F. *Inorg. Chem.* **1993**, *32*, 1045-1047. (c) Lawrance, G. A. *Chem Rev.* **1986**, *86*, 17-33.

70. (a) Camp, A. M.; Kita, M. R.; Grajeda, J.; White, P. S.; Dickie, D. A.; Miller, A. J. M. *Inorg. Chem.* **2017**, 56, 11141–11150. (b) Aldrich, K. E.; Billow, B. S.; Holmes, D.; Bemowski, R. D.; Odom, A. L. *Organometallics **2017***, 36, 1227–1237. (c) Ward, W. M.; Farnum, B. H.; Siegler, M.; Meyer, G. J. *J. Phys. Chem. A* **2013**, *117*, 8883-8894. (d) La Mar, G. N. *J. Chem. Phys*. **1964**, *41*, 2992.

71. (a) Miras, H.N.; Wilson, E.F.; Cronin, L. *Chem. Commun*. **2009**, 1297-1311. (b) Baytekin, B.; Baytekin, H. T.; Schalley, C. A. *Org. Biomol. Chem.* **2006**, *4*, 2825.

72. (a) Banerjee, S.; Mazumdar, S. *Int. J. Anal. Chem.* **2012**, *2012*, Article ID 282574. Doi:10.1155/2012/282574. (b) Schalley, C. A. *Mass Spectrum. Rev*. **2005**, *16*, 253-309. (c) Loo, J. A. *Int. J. Mass Spectrum.* **2000**, *200*, 175-186. (d) Smith, R. D.; Light-Wahl, K. J. *Biol. Mass Spectrum*. **1993**, *22*, 493-501.

73. (a) Reger, D. L.; Watson, R. P.; Gardinier, J. R.; Smith, M. D. *Inorg. Chem.* **2004**, *43*, 6609-6619. (b) Reger, D. L.; Gardinier, J. R.; Semeniuc, R. F.; Smith, M. D. *J. Chem. Soc., Dalton Trans.* **2003**, 1712-1718. (c). Reger, D. L.; Gardinier, J. R.; Grattan, T. C.; Smith, M. R.; Smith, M. D. *New J. Chem.* **2003**, 1670-1677. (d) Reger, D. L.; Foley, E. A.; Semeniuc, R. F.; Smith, M. D. *Inorg. Chem.* **2007**, *46*, 11345-11355. (e) Reger, D. L.; Semeniuc, R. F.; Rassolov, V.; Smith, M. D. *Inorg. Chem.* **2004**, *43*, 537-554.

74. (a) Reger, D. L.; Gardinier, J. R.; Smith, M. D. *Inorg. Chem.* **2004**, *43*, 3825-3832. (b) Reger, D. L.; Foley, E. A.; Smith, M. D. *Inorg. Chem*. **2009**, *48*, 936-945. (c) Reger D. L; Watson R. P; Smith M. D. *Inorg. Chem.* **2006**, *45*, 10077-10087.

75. Reger, D. L.; Gardinier, J. R.; Grattan, T. J.; Smith, M. D. *J. Organomet. Chem.* **2005**, *690*, 1901-1912.

76. (a) Niesel, J.; Pinto, A.; N'Dongo, H. W. P.; Merz, K.; Ott, I.; Gust, R.; Schatzschneider, U. *Chem. Commun.* **2008**, *0*, 1798-1800. (b) Pfeiffer, H.; Rojas, A.; Niesel J.; Schatzschneider U. *Dalton Trans.* **2009**, 4292–4298. (c) Pai, S.; Hafftlang, M.; Atongo, G.; Nagel, C.; Niesel, J.; Botov, S.; Schmalz, H.-G.; Yard B.; Schatzschneider, U. *Dalton Trans.* **2014**, 43, 8664–8678.

77. Feng, J. –J.; Zhang, J. *ACS Catalysis*, **2016**, *6*, 6651-6661. (b) Wender, P. A.; Strand, D. *J. Am. Chem. Soc.* **2009**, 131, 7528-7529.

78. Maeda, R.; Ishibashi, R.; Kamaishi, R.; Kirotaki, K.; Furuno, H.; Hanamoto, T. *Org. Lett.* **2011**, *13*, 6240-6243.

79. Kaicharla, T.; Jacob, A.; Gonnade, R. G.; Biju, A. T. *Chem. Commun.* **2017**, *53*, 8219-8222.

80. Gutlich, P.; Goodwin, H. A. *Spin Crossover in Transition Metal Compounds I-III. Topics in Current Chemistry;* Springer-Verlag: Berlin, Germany, 2004; Vol 233-235.

81. Gütlich, P.; Hauser, A.; Spiering, H. *Angew. Chem., Int. Ed. Engl.* **1994**, *33*, 2024–2054.

82. Gütlich, P.; Garcia, Y.; Goodwin, H. A. *Chem. Soc. Rev.* **2000**, *29*, 419-427.

83. Gütlich, P. *Hyperfine Interactions **1987***, *33*, 105-132.

84. Levchenko, G. G.; Khristov, A. V.; Varyukhin, V. N. *Low Temp. Phys.* **2014**, *40*, 571-585.

85. Drickamer, H. G. *Angew. Chem.* **1974**, *13*, 39-47.

86. Lenz, F. *J. Phys.: Conf. Ser.* **2010**, *217*, 012022.

87. Pineiro-Lopez, L.; Valverde-Munoz, F. J.; Seredyuk, M.; Munoz, M. C.; Haukka, M.; Real, J. A. *Inorg. Chem.* **2017**, *56*, 7038-7047.

88. Lennartson, A.; Southon, P.; Sciortino, N.F.; Kepert, C. J.; Frandsen, C.; Morup, S.; Piligkos, S.; McKenzie, C. J. *Chem. –Eur. J.* **2015**, *21*, 16066-16072.

89. Coronado, E.; Gimenez-Marques, M.; Minguez Espallargas, G.; Rey, F.; Vitorica-Yrezabal, I. J. *J. Am. Chem. Soc.* **2013**, *135*, 15986-15989.

90. Bartual-Murgui, C.; Akou, A.; Shepherd, H. J.; Molnar, G.; Real, J. A.; Salmon, L.; Bousseksou, A. *Chem. Eur. J.* **2013**, *19*, 15036-15043.

91. Lefter, C.; Tan, R.; Dugay, J.; Tricard, S.; Molnár, G.; Salmon, L.; Carrey, J.; Nicolazzi, W.; Rotaru, A.; Bousseksou, A. *Chem. Phys. Lett.* **2016**, *644*, 138-141.

92. Nègre, N.; Consejo, C.; Goiran, M.; Bousseksou, A.; Varret, F.; Tuchagues, J. P.; Barbaste, R.; Askénazy, S.; Haasnoot, J. G. *Physica B* **2001,** *91*, 294–295.

93. Unruh, D.; Homenya, P.; Kumar, M.; Sindelar, R.; Garcia, Y.; Renz, F. *Dalton Trans.* **2016**, *45*, 14008-14018.

94. Zhang, Wenkai; Gaffney, Kelly J. *Acc. Chem. Res.* **2015**, *48*, 1140-1148.

95. P. Guionneau and E. Collet, "Piezo- and photo-crystallography applied to spin-crossover materials" in Ref. 1, ch. 20, pp. 507–526.

96. Létard, J.-F. *J. Mater. Chem.* **2006**, *16*, 2550-2559.

97. Legrand, V.; Carbonera, C.; Pillet, S.; Souhassou, M.; Létard, J.-F.; Guionneau, P.; Lecomte, C. *J. Phys.: Conf. Ser.* **2005**, *21*, 73–80.

98. Kumar, K. S.; Ruben, M. *Coord. Chem. Rev.* **2017**, *346*, 176-205.

99. Lefter, C.; Davesne, V.; Salmon, L.; Molnar, G.; Demont, P.; Rotaru, A.; Bousseksou, A. *Magnetochemistry* **2016**, *2*, 1-19.

100. Holovchenko, A.; Dugay, J.; Gimenez-Marques, M.; Torres-Cavanillas, R.; Coronado, E.; van der Zant, H. S. J. *Adv. Mater.* **2016**, *28*, 7228-7233.

101. Manrique-Juarez, M. D.; Mathieu, F.; Shalabaeva, V.; Cacheux, J.; Rat, S.; Nicu, L.; Leichle, T.; Salmon, L.; Molnar, G.; Bousseksou, A. *Angew. Chem., Int. Ed.* **2017**, *56*, 8074-8078.

102. von Ranke, P. J. *Appl. Phys. Lett.* **2017**, *110*, 181909/1-181909/4.

103. Kucheriv, O. I.; Oliynyk, V. V.; Zagorodnii, V. V.; Launets, V. L.; Gural'skiy, I. A. *Scientific Reports* **2016**, *6*, 38334.

104. Thorarinsdottir, A. E.; Gaudette, A. I.; Harris. T. D. *Chem Sci.* **2017**, *8*, 2448–2456.

105. Jeon, I.-R.; Park, J. G.; Haney, C. R.; Harris, T. D. *Chem. Sci.* **2014**, *5*, 2461-2465.

106. Park, J. G.; Jeon, I.-R.; Harris, T. D. *Inorg. Chem.* **2015**, *54*, 359–369.

107. Holzhacker, C.; Calhorda, M. J.; Gil, A.; Carvalho, M. D.; Ferreira, L. P.; Stoeger, B.; Mereiter, K.; Weil, M.; Mueller, D.; Weinberger, P.; Pittenauer, E.; Allmaier, G.; Kirchner, K. *Dalton Trans.* **2014**, *43*, 11152-11164.

108. Aguila, D.; Dechambenoit, P.; Rouzieres, M.; Mathoniere, C.; Clerac, R. *Chem. Commun.* **2017**, *53*, 11588-11591.

109. Yergeshbayeva, S.; Hrudka, J. J.; Lengyel, J.; Erkasov, R.; Stoian, S. A.; Dragulescu-Andrasi, A.; Shatruk, M. *Inorg. Chem.* **2017**, *56*, 11096-11103.

110. Phonsri, W.; Davies, C. G.; Jameson, G. N. L.; Moubaraki, B.; Ward, J. S.; Kruger, P. E.; Chastanet, G.; Murray, K. S. *Chem. Commun.* **2017**, *53*, 1374-1377.

111. Travieso-Puente, R.; Broekman, J. O. P.; Chang, M.-C.; Demeshko, S.; Meyer, F.; Otten, E. *J. Am. Chem. Soc.* **2016**, *138*, 5503-5506.

112. Creutz, S. E.; Peters, J. C. *Inorg. Chem.* **2016**, *55*, 3894-3906.

113. Craig, G. A.; Roubeau, O.; Aromi, G. *Coord. Chem. Rev.* **2014**, *269*, 13-31.

114. Roubeau, O. *Chem. – Eur. J.* **2012**, *18*, 15230-15244.

115. Olguin, J.; Brooker, S. *Coord. Chem. Rev.* **2011**, *255*, 203-240.

116. Munoz, M. C.; Real, J. A. *Coord. Chem. Rev.* **2011**, *255*, 2068-2093.

117. Goodwin, H. A. *Top. Curr. Chem.* **2004**, *233*, 59-90.

118. Phan, H.; Hrudka, J. J.; Igimbayeva, D.; Lawson D., Latevi M.; Shatruk, M. *J. Am. Chem. Soc.* **2017**, *139*, 6437-6447.

119. Trofimenko, S. *J. Am. Chem. Soc.* **1967**, *89*, 3170-3177.

120. Trofimenko, S. *J. Am. Chem. Soc.* **1967**, *89*, 6288–6294.

121. Jesson, J. P.; Trofimenko, S.; Eaton, D. R. *J. Am. Chem. Soc.* **1967**, *89*, 31-48-3158.

122. Jesson, J. P.; Weiher, J. F.; Trofimenko, S. *J. Chem. Phys.* **1968**, *48*, 2058-2066.

123. Long, G. J.; Hutchinson, B. B. *Inorg. Chem.* **1987**, *26*, 608-613.

124. Mahfoud, T.; Molnár, G.; Cobo, S.; Salmon, L.; Thibault, C.; Vieu, C.; Demont, P.; Bousseksou, A. *Appl. Phys. Lett.* **2011**, *99*, 053307.

125. Davesne, V.; Gruber, M.; Studniarek, M.; Doh, W. H.; Zafeiratos, S.; Joly, L.; Sirotti, F.; Silly, M. G.; Gaspar, A. B.; Real, J. A.; Schmerber, G.; Bowen, M.; Weber, W.; Boukari, S.; Da Costa, V.; Arabski, J.; Wulfhekel, W.; Beaurepaire, E. *J.Chem. Phys.* **2015**, *142*, 194702/1-194702/8.

126. Iasco, O.; Boillot, M.-L.; Bellec, A.; Guillot, R.; Rivière, E.; Mazerat, S.; Nowak, S.; Morineau, D.; Brosseau, A.; Miserque, F.; Repain, V.; Mallah, T. *J. Mater. Chem. C* **2017**, Advance Article. DOI: 10.1039/C7TC03276E

127. Real, J. A.; Muñoz, M. C.; Faus, J.; Solans, X. *Inorg. Chem.* **1997**, *36*, 3008–3013.

128. Moliner, N.; Salmon, L.; Capes, L.; Muñoz, M. C.; Létard, J.-F.; Bousseksou, A.; Tuchagues, J.-P.; McGarvey, J. J.; Dennis, A. C.; Castro, M.; Burriel, R.; Real, J. A. *J. Phys. Chem. B* **2002** *106*, 4276-4283.

129. Galet, A.; Gaspar, A. B.; Agusti, G.; Muñoz, M. C.; Levchenko, G.; Real, J. A. *Eur. J. Inorg. Chem.* **2006**, *2006*, 3571-3573.

130. Moertel, M.; Witt, A.; Heinemann, F. W.; Bochmann, S.; Bachmann, J.; Khusniyarov, M. M. *Inorg. Chem.* **2017**, Ahead of Print.

131. Ru, J.; Yu, F.; Shi, P.-P.; Jiao, C.-Q.; Li, C.-H.; Xiong, R.-G.; Liu, T.; Kurmoo, M.; Zuo, Jing-L. *Eur. J. Inorg. Chem.* **2017**, *2017*, 3144-3149.

132. Luo, Y.-H.; Nihei, M.; Wen, G.-J.; Sun, B.-W.; Oshio, H. *Inorg. Chem.* **2016**, *55*, 8147-8152.

133. Milek, M.; Heinemann, F. W.; Khusniyarov, M. M. *Inorg. Chem.* **2013**, *52*, 11585-11592.

134. Rat, S.; Mikolasek, M.; Costa, J. S.; Chumakov, A. I.; Nicolazzi, W.; Molnar, G.; Salmon, L.; Bousseksou, A. *Chem. Phys. Lett.* **2016**, *653*, 131-136.

135. Ossinger, S.; Naggert, H.; Kipgen, L.; Jasper-Toennies, T.; Rai, A.; Rudnik, J.; Nickel, F.; Arruda, L. M.; Bernien, M.; Kuch, W.; Berndt, R.; Tuczek, F. *J. Phys. Chem. C* **2017**, *121*, 1210-1219.

136. Beniwal, S.; Zhang, X.; Mu, S.; Naim, A.; Rosa, P.; Chastanet, G.; Letard, J.-F.; Liu, J.; Sterbinsky, G. E.; Arena, D. A.; Dowben, P. A.; Enders, A. *J. Phys.* **2016**, *28*, 206002/1-206002/8

137. Naggert, H.; Rudnik, J.; Kipgen, L.; Bernien, M.; Nickel, F.; Arruda, L. M.; Kuch, W.; Naether, C.; Tuczek, F. *J. Mater. Chem. C* **2015**, *3*, 7870-7877.

138. Bernien, M.; Naggert, H.; Arruda, L. M.; Kipgen, L.; Nickel, F.; Miguel, J.; Hermanns, C. F.; Krüger, A.; Krüger, D.; Schierle, E.; Weschke, E.; Tuczek, F.; Kuch, W. *ACS Nano*. **2015**, *9*, 8960–8966.

139. Kulmaczewski, R.; Shepherd, H. J.; Cespedes, O.; Halcrow, M. A. *Inorg. Chem.* **2014** *53*, 9809-9817.

140. Piquer, C.; Grandjean, F.; Mathon, O.; Pascarelli, S.; Reger, D. L.; Little, C. A.; Long, G. J. *Inorg. Chem.* **2003**, *42*, 982-985.

141. Reger, D. L.; Little, C. A.; Smith, M. D.; Long, G. J. *Inorg. Chem.* **2002**, *41*, 4453-4460.

142. Shvachko, Y. N.; Starichenko, D. V.; Korolyov, A. V.; Yagubskii, E. B.; Kotov, A. I.; Buravov, L. I.; Lyssenko, K. A.; Zverev, V. N.; Simonov, S. V.; Zorina, L. V.; Shakirova, O. G.; Lavrenova, L. G. *Inorg. Chem.* **2016**, *55*, 9121-9130.

143. Shakirova, O. G.; Lavrenova, L. G.; Korotaev, E. V.; Sheludyakova, L. A.; Varnek, V. A.; Shestopalov, M. A.; Mironov, Yu. V. J. *Struct. Chem.* **2015**, *56*, 1520-1526.

144. Shakirova, O. G.; Lavrenova, L. G.; Bogomyakov, A. S.; Zhizhin, K. Yu.; Kuznetsov, N. T. *Russ. J. Inorg. Chem.* **2015**, *60*, 786-789.

145. Lavrenova, L. G.; Shakirova, O. G. *Eur. J. Inorg. Chem.* **2013**, *2013*, 670-682.

146. Goodman, M. A.; DeMarco, M. J.; Tarasek, S. E.; Nazarenko, A. Y.; Brennessel, W.; Goodman, M. S. *Inorg. Chim. Acta* **2014**, *423*, 358–368.

147. Sohrin, Y.; Kokusen, H.; Matsui, M. *Inorg. Chem.* **1995**, *34*, 3928-3934.

148. Hamon, P.; Thépot, J.-Y.; Le Floch, M.; Boulon, M.-E.; Cador, O.; Golhen, S.; Ouahab, L.; Fadel, L.; Saillard, J.-Y.; Hamon, J.-R. *Angew. Chem. Int. Ed.* **2008**, *47*, 8687 –8691.

149. Gardinier, J. R.; Meise, K. J.; Jahan, F.; Lindeman, S. V. *Inorg. Chem.* **2017**, submitted.

150. Fulmer, G. R.; Miller, A. J. M.; Sherden, N. H.; Gottlieb, H. E.; Nudelman, A.; Stoltz, B. M.; Bercaw, J. E.; Goldberg, K. I. *Organometallics* **2010**, *29*, 2176-2179.

151. Desiraju, G. R.; Steiner, T.; *The Weak Hydrogen Bonding in Structural Chemistry and Biology*; Oxford University Press: New York, 1999.

152. Taylor, R.; Kennard, O. *Acc. Chem. Res*. **1984**, *17*, 320-326.

153. Arunan, E.; Desiraju, G. R.; Klein, R. A.; Sadlej, J.; Scheiner, S.; Alkorta, I.; Clary, D. C.; Crabtree, R. H.; Dannenberg, J. J.; Hobza, P.; Kjaergaard, H. G.; Legon, A. C.; Mennucci, B.; Nesbitt, D. J. *Pure Appl. Chem.* **2011**, *83*, 1637–1641.

154. Grepioni, F.; Cojazzi, G.; Draper, S. M.; Scully, N.; Braga, D. *Organometallics* **1998**, *17*, 296-307.

155. Gardinier, J. R.; Tatlock, H. M.; Hewage, J. S.; Lindeman, S. V. *Cryst. Growth Des.* **2013**, *13*, 3864-3877.